A CORRELATION-BASED APPROACH TO MODELING INTERFEROMETRIC RADAR OBSERVATIONS OF THE GREENLAND ICE SHEET

A DISSERTATION
SUBMITTED TO THE DEPARTMENT OF APPLIED PHYSICS
AND THE COMMITTEE ON GRADUATE STUDIES
OF STANFORD UNIVERSITY
IN PARTIAL FULFILLMENT OF THE REQUIREMENTS
FOR THE DEGREE OF
DOCTOR OF PHILOSOPHY

By
Weber Hoen
March 2001

I certify that I have read this dissertation and that in my opinion it is fully adequate, in scope and quality, as a dissertation for the degree of Doctor of Philosophy.

Howard A. Zebker
(Principal Adviser)

I certify that I have read this dissertation and that in my opinion it is fully adequate, in scope and quality, as a dissertation for the degree of Doctor of Philosophy.

G. Leonard Tyler

I certify that I have read this dissertation and that in my opinion it is fully adequate, in scope and quality, as a dissertation for the degree of Doctor of Philosophy.

Gordon Kino

Approved for the University Committee on Graduate Studies:

Contents

1 Introduction **1**

1.1 History 1

1.2 Motivation 7

1.3 Contributions 7

1.4 Synopsis 8

2 Remote Sensing of Ice Sheets **9**

2.1 Overview 9

2.2 Mass Balance 10

2.3 Structure of the Near-Surface 12

2.4 Remote Sensing 16

2.4.1 Overview 16

2.4.2 ERS SAR Mosaic 18

3 SAR and InSAR **22**

3.1 Overview 22

3.2 Introduction to spaceborne SAR 22

3.2.1 Terminology 22

3.2.2 SAR imaging 25

3.2.3 Geometry of the SAR Impulse Response 28

3.2.4 Pixels 33

3.2.5 SAR scattering characteristics 34

3.2.6 Speckle 39

3.2.7 InSAR Power 40

3.3 InSAR . . . 42
3.3.1 Across-track interferometer . . . 42
3.3.2 Topography measurement . . . 45
3.3.3 Motion measurement . . . 46
3.3.4 Atmospheric signal . . . 52
3.3.5 Total phase . . . 53

4 Correlation **54**
4.1 Introduction . . . 54
4.2 Correlation Measurement . . . 55
4.3 Spatial Decorrelation . . . 59
4.3.1 Overview . . . 59
4.3.2 Formation of Spatial Correlation Model . . . 61
4.3.3 Surface Scatter . . . 65
4.3.4 Volume Scatter . . . 69
4.4 Other Decorrelation Sources . . . 72
4.4.1 Data and Processing Errors . . . 73
4.4.2 Thermal Decorrelation . . . 76
4.4.3 Temporal Decorrelation . . . 77
4.4.4 Doppler Centroid Differences . . . 81
4.5 Conclusion . . . 82

5 Penetration Depths of the Greenland Ice Sheet **84**
5.1 Introduction . . . 84
5.2 Densification . . . 85
5.3 Temporal Decorrelation . . . 88
5.4 Other C-Band Penetration Measurements in Polar Firn . . . 90
5.5 Data . . . 93
5.6 Greenland Ice Sheet Examples . . . 96
5.6.1 Site A: Dry Snow Zone . . . 96
5.6.2 Sites B and C: Ryder Glacier . . . 100
5.6.3 Strip D: Coast to Interior . . . 102

5.6.4 Penetration Depth Discrepancy 105
5.7 Conclusion 109

6 Variations in Dry Snow Zone Structure **111**
6.1 Introduction 111
6.2 Power and Correlation in the Dry Snow Zone 113
6.3 Reasoning for Similarities in Power and Correlation 116
6.4 Snow-grain scattering 120
6.5 Evidence C-band Scattering from Buried Layers 128
6.6 Layering 130
6.7 Conclusion 135

7 Conclusion **138**
7.1 Contributions 138
7.2 Future Work 139

A Correlation Lengths **141**

List of Tables

1.1 Important ERS 1/2 parameters 4

2.1 Mass Balance of the Greenland Ice Sheet 11

3.1 Orbit Information for Ryder Data 48

5.1 Greenland Site Location and Correlation Image Quantity 95

5.2 Dry Snow Zone and Ryder Glacier Results 102

List of Figures

1.1 Shaded Relief and Contour Map of Greenland 2
1.2 Timeline of Spaceborne SAR Missions 5

2.1 Mass Balance Schematic 11
2.2 Profile of Greenland Surface Height 12
2.3 The Glacial Zones of the Accumulation Area of Greenland 13
2.4 Density Profile of the Greenland Firn 14
2.5 Snow Grain Size vs. Depth 15
2.6 Density Profile for a Shallow Pit, Summit, Greenland 16
2.7 Greenland SAR Mosaic and Accumulation Data 19

3.1 SAR Viewing Geometry 23
3.2 Pixel vs Resolution Size 25
3.3 The Synthetic Aperture 27
3.4 Squint Angle 28
3.5 Range Resolution Geometry 30
3.6 Impulse Responses for Square and Kaiser Windows 32
3.7 SAR Scattering Geometry 34
3.8 Power Image of the North Coast of Greenland 42
3.9 InSAR Viewing Geometry 43
3.10 Location and Power Image of Ryder Glacier Channel 49
3.11 Two Interferograms of the Ryder Glacier Channel 50
3.12 Topography and Motion from Interferometric Phase 51
3.13 Atmospheric Artifacts in Interferograms 53

4.1 Bias Due to Spatial Averaging 57

4.2 Standard Deviation vs. Mean Correlation 58
4.3 Correlation Images from the Dry Snow Zone of Greenland 60
4.4 Correlation Distributions 60
4.5 Interferometric Viewing Geometry for Volume Scatter 61
4.6 Surface Decorrelation for Square and Kaiser Window Functions 67
4.7 K-Shift of Ground Reflectivity Spectrum 68
4.8 Spatial Decorrelation from Shifted Spectra 68
4.9 Theoretical and Simulated Volume Decorrelation 72
4.10 Correlation Streaks Caused by Raw Data Errors 74
4.11 Correlation Loss From Misregistration 75
4.12 Decorrelation from Phase Gradients 75
4.13 Thermal Decorrelation from SNR 77
4.14 Crawford Point Location 78
4.15 Crawford Point Power, Correlation, and Temperature 80
4.16 Expected Thermal Correlation Images 81
4.17 Correlation vs Difference in Doppler Centroid 82

5.1 Relative Permittivities vs. Density 85
5.2 Volume Decorrelation including Densification 87
5.3 South Pole Penetration 91
5.4 Geikie Ice Cap Experiment 93
5.5 The Offset Between the True Surface and the Interferometrically-derived Surface vs. Penetration Depth 94
5.6 Sites A, B, C, D, in Northern Greenland 94
5.7 Dry Snow Zone Correlation Maps 96
5.8 Dry Snow Zone Results 97
5.9 Site A Optimization Results 98
5.10 Ryder Glacier Correlation Maps 99
5.11 Ryder Glacier Results 100
5.12 Site B and C Optimization Results 101
5.13 Strip D Correlation Maps 104

5.14 NASA-U and Humboldt Weather Stations 105
5.15 Temperature and Wind Speed Data for NASA-U Weather Station 106
5.16 Temperature and Wind Speed Data for Humboldt Weather Station 107

6.1 Dry Snow Zone Topography, Power, and Correlation 114
6.2 Profile of Dry-Snow Zone Images 115
6.3 Rocky Coast Power and Correlation Variations 116
6.4 Increases in the Scattering Coefficient 118
6.5 Local Average Prevailing Winds 119
6.6 Penetration Depth along the Profile 119
6.7 Topographic Undulations and the Radar Signal 120
6.8 Power and Penetration for Three Grain-Scattering Models 123
6.9 Power and Penetration for Density-Increasing Medium 125
6.10 Correlation vs. Grain Size for Density-Increasing Medium 127
6.11 Correlation vs. Power from Grain Size Variations 127
6.12 Laser Altimeter RMS Variations 129
6.13 σ^0 vs. Incidence Angle 130
6.14 Layered Scattering 131
6.15 Correlation vs. Power for a Layered Medium 134
6.16 Power and Correlation for a Layered Medium 135
6.17 Map of Annual Hoar Layer Spacing 136

Chapter 1

Introduction

1.1 History

test-this test–this

The Earth's cryosphere, comprised largely of the Greenland and Antarctica ice caps, has been largely unknown, or otherwise ignored throughout history. Adventurers began mounting campaigns to the polar regions by the start of the 20th century, primarily for repute, but also to make detailed scientific observations of these vast and remote places. It was not until 1957, during the International Geophysical Year, that scientists from the developed countries of the world included the ice sheets in a global set of geophysical measurements. There have been many *in situ* studies in the interiors of the ice sheets since, in which data describing snowpack accumulation, temperature, chemistry, stratigraphy, rheology, and morphology have been collected.

The difficulties of mounting field campaigns to the Greenland ice sheet are many, mainly due to harsh climate and remoteness. The entire 2000 km x 1000 km extent of Greenland lies above 60° N, as shown in the map of Fig. 1.1. The average temperature in the interior of the the Greenland ice sheet, where the altitude climbs to over 3000 m, is below −20° C [Paterson, 1994]. During the winter months Greenland is shrouded in darkness. Exploration of Antarctica poses similar but even greater hurdles. Moreover, even a successful campaign to these regions will produce a scientific dataset comprised of only a few isolated points on an enormously under-sampled spatial grid, in an environment where a high degree of variation over short distances is possible.

With the advent of remote sensing techniques, in particular satellite-borne sensors, many of the gaps in the various geophysical maps have begun to be filled in. Satellite remote

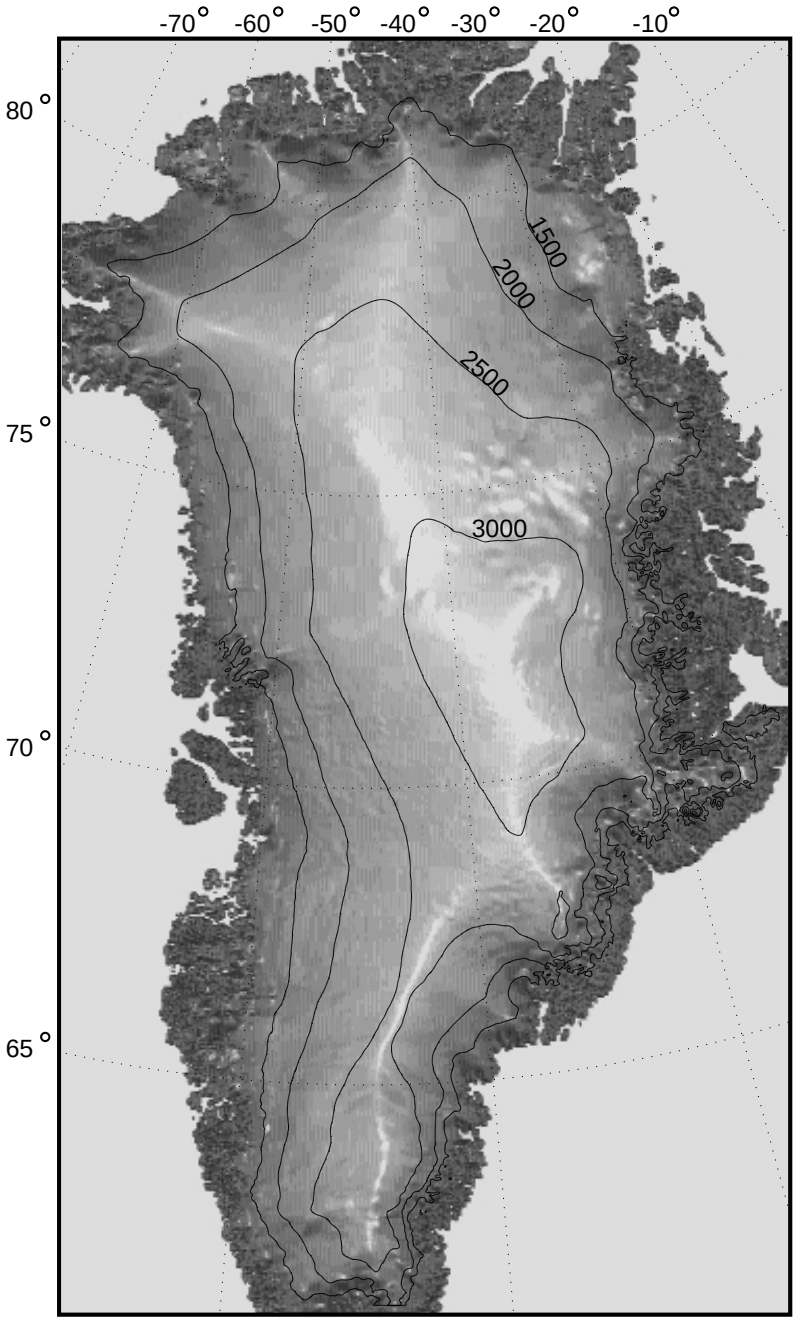

Figure 1.1: Shaded relief and contour map of Greenland, with elevation contours in meters. Most of Greenland lies above 2000 m, but with little topographic variation seen in the interior regions. DEM courtesy of Ian Joughin, NASA-JPL, 2000.

sensing efforts have employed an array of different sensors, both active and passive, most of which were not designed for the explicit purpose of polar observation. In the years since the 1964 launch of the first Nimbus satellite, however, orbiting instruments have revolutionized our understanding of the polar ice sheets. This followed not only from the comprehensive coverage that the satellites afford, but also from the broad range of the electromagnetic spectrum to which they are sensitive, since observations at different wavelengths contain different aspects of the ice sheet. A review of satellite remote sensing of the ice sheets can be found elsewhere [Bindschadler, 1998b]. With an understanding guided by remote sensing techniques, the ice sheets are now seen as an extremely complex and pivotal component in the global climate system.

Radar satellites in particular have proven useful in remote sensing of the ice sheets. While radar, which stands for *ra*dio *d*etection *a*nd *r*anging system, has its experimental beginning in the late 19th century, it was in not until World WAR II that it became of widespread use. In the 1950s engineers first recognized that, instead of rotating a radar antenna to scan an area on the Earth's surface, an antenna mounted on an aircraft could achieve the same goal of areal coverage. It was found that significant image resolution enhancement in the flight direction could be obtained by separating the return echoes according to their Doppler shift. This was the birth of the synthetic aperture radar, or SAR, so named because the along-track resolution could be enhanced by combining a series of echoes, thus "synthesizing" an aperture much larger than the physical dimension of the antenna. It was not until 1978, with the launch of the National Aeronautical and Space Administration (NASA) satellite Seasat, however, that SAR imaging systems mounted aboard orbiting satellites began to play an important role in remote sensing of the Earth. (See Fig. 1.2 for an operational timeline of the Earth-observing SAR satellites.) These early satellite missions showed that synthetic aperture radar can reliably map the planet's surface and acquire information about its physical properties, such as topography, morphology, small-scale roughness and dielectric characteristics.

Spaceborne SAR systems transmit and receive microwave radiation at cm–dm wavelengths, operating in a regime of the electromagnetic spectrum which passes largely unaffected through clouds and dust, though heavy rain may impede transmission to a degree. Also, SAR systems provide their own illumination in the form of a string of coherent pulses.

Table 1.1: Important ERS 1/2 parameters

Parameter	**Value**
Wavelength, m	0.0566
Altitude, km	790
Pulse repetition frequency, Hz	1679
Pulse length, μ sec	37.1
Range bandwidth, MHz	15.55
Receiver noise temperature, K	3700
Range to first pixel, km	831.6
Incidence angle, deg	23
Slant range resolution, m	10.2
Ground range resolution, m	25
Azimuth resolution, m	6
1-look range pixel size, m	20
1-look azimuth pixel size, m	4
Scene size on ground, km^2	$\sim$100 x 100
Observation repeat interval, days	1, 3, 35
Nominal critical baseline, m	1100

Hence, they can acquire information globally and almost independently of meteorological conditions and solar illumination. Furthermore, using pulse compression techniques and the extended synthetic aperture, geometric resolutions of a few to tens of meters can be achieved easily with physical antennas that are modest in size. The trade-off for these advantages, in comparison to optical systems, are the need for transmit power and an increased amount of signal processing.

All of the SAR observations presented here are from the European Space Agency's (ESA) European Research Satellites (ERS). There are two of these, ERS-1 and ERS-2, which were put in orbit in 1991 and 1995, respectively, as shown in Fig. 1.2. Table 1.1 lists the important ERS parameters, which we will explain in greater detail in Chaps. 3 and 4.

As with any interferometric application, combining two SAR observations of the same scene on the ground can teach us more about the terrain than does one SAR image alone.

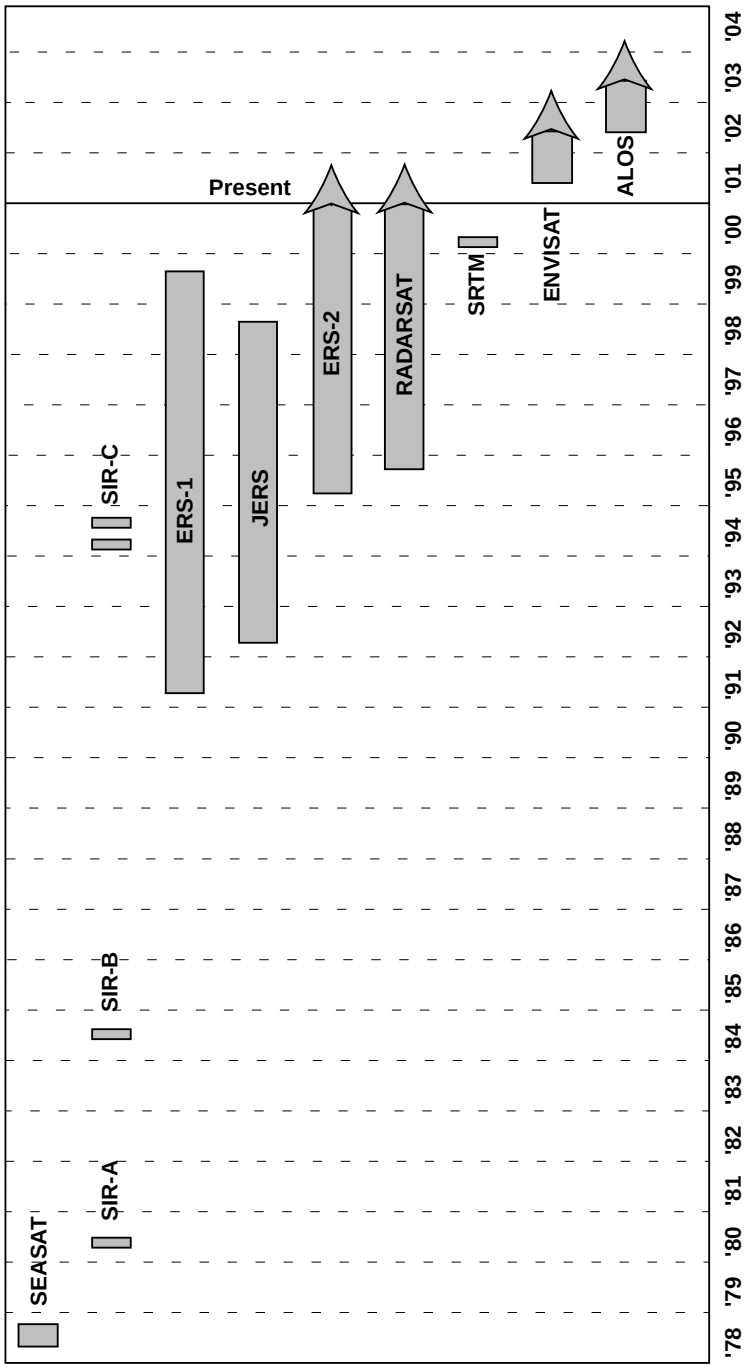

Figure 1.2: A timeline of spaceborne, Earth-observing SAR missions. The missions with arrows at the end are either on-going or planned for the future.

The basic principle for interferometric SAR, or InSAR, dates back to the early 1970s [Graham, 1974]. In regards to Earth-observing satellites, it was only in the late 1980s that the first experimental results were published [Zebker and Goldstein, 1986; Goldstein and Zebker, 1987; Goldstein et al., 1988; Gabriel and Goldstein, 1988; Gabriel et al., 1989; Goldstein et al., 1989; Prati et al., 1989]. At that time only a few datasets from the Seasat, SIR-A, and SIR-B missions were available, as shown in Fig. 1.2. After the launch of ERS-1 in 1991, though, an enormous quantity of data suitable for interferometry became available, and various research groups around the world began to use the technique with success. Other space-borne missions that have provided interferometric possibilities are the Japanese satellite JERS, the Canadian satellite Radarsat, and three different NASA shuttle missions: SIR-B, SIR-C, and SRTM. Adding to this interferometric dataset are a few airborne missions, such as NASA's TOPSAR and AIRSAR. There are several future satellite-borne SAR imaging missions planned as well, including a yet-unnamed American SAR mission slated for a 2005 launch.

The initial theory and first application of InSAR concentrated on mapping the Earth's topography [Graham, 1974; Zebker and Goldstein, 1986]. The topographic information is derived from two spatially separated observations that form an interferometric pair. Today it is generally accepted that InSAR is an extremely powerful tool for mapping the Earth's topography, and there are many sensors, both airborne and space-borne, that employ this technique. Recently, the Shuttle Radar Topographic Mapper (SRTM) was flown aboard NASA's space shuttle in order to create a precise and consistent digital elevation model (DEM) for most of the Earth's landmass.

With the phenomenal lifetime of the ERS satellites, interferometric pairs with long temporal separations became possible. Thus the observations could "sandwich" geophysical events, such as earthquakes, volcano eruptions, or floods, and detect changes occurring in the terrain due to such events. InSAR deformation studies using this technique can detect cm-scale motion of the Earth's surface. For this approach to be successful the velocity field of the surface must be coherent on the scale of a few resolution elements. Gabriel et al. [1989], using Seasat data, were the first to use the technique in measuring subsidence in Imperial Valley, California. It was not until the ERS study of the Landers earthquake in Southern California by Massonet et al. [1993], in which a multi-lobed pattern of crustal

deformation was measured, however, that the use of the technique became widely known. Many other illustrative crustal deformation studies using InSAR have been published since, including studies of other earthquakes, the inflation or deflation of volcanos, subsidence the ground due to water/oil extraction, and landslides. For a more complete review of crustal deformation studies using InSAR, see Massonet and Feigl [1998]. Recently the differential technique has reportedly become precise enough to be able to measure the thermal expansion of buildings [Ferretti et al., 2000]!

1.2 Motivation

In terms of the ice sheets, InSAR techniques have led to more accurate descriptions than has previously been possible with other remote sensing systems of both surface topography [Kwok and Fahnestock, 1996; Joughin et al., 1996b; Dall et al., 2001] and motion [Goldstein et al., 1993; Joughin et al., 1995; Rignot et al., 1995; Joughin et al., 1996a; Rignot et al., 1997; Joughin et al., 1997, 1998, 1999]. These studies have dramatically increased our knowledge of the features and kinetics of the ice sheets. What is lacking currently is a more complete description of the near sub-surface, since the recent climatic history is recorded in these first meters. SAR observations, as we will discuss in Chap. 2, give some information about the sub-surface, but a more complete description is needed. *In situ* studies, of course, can render the sub-surface in far greater detail than any remote-sensing experiment, but, as stated above, these are limited horizontally and temporally. Thus a means to probe the sub-surface by remote sensing methods is needed, in order to read the recent climate history of the ice sheet.

In this dissertation we show that InSAR correlation, by way of a straight-forward scattering model, can fulfill this need.

1.3 Contributions

The contributions of the research presented in this dissertation are:

1. An extended model of expected InSAR correlation observations which includes dielectric volume scattering.

2. Radiowave penetration depth maps of Greenland firn using decorrelation model.

3. Observations and models of the leeward/windward side differences in backscatter and correlation in the dry snow zone.

4. Correlation and power analyses constraining models to estimate accumulation rates.

1.4 Synopsis

This is a multi-disciplinary study, combining elements of glaciology, signal processing, and electromagnetics. We begin with an effort to provide sufficient background for non-experts in each of these areas. Chap. 2 provides an introduction to the ice sheets, concentrating on the first ten or so meters in the snowpack, which is the most relevant section for radar remote sensing. The basics of SAR power observations are given in the first part of Chap. 3, including scattering from a dielectric volume. The second part of Chap. 3 is devoted to In-SAR phase measurements with examples from the Greenland ice sheet. Chap. 4 develops a volume correlation model that allows us to statistically estimate radiowave ice penetration depths. Included in the chapter are several practical aspects of making correlation measurements. Chap. 5 demonstrates application of our volume decorrelation model to ERS data from the Greenland ice sheet, and estimation of penetration depths at several different locations on the ice sheet. In Chap. 6 we examine the relationship between variations in topography, correlation, and backscattered power, and investigate two different scattering models to derive accumulation rates. We discuss our conclusions in Chap. 7.

Chapter 2

Remote Sensing of Ice Sheets

2.1 Overview

The Greenland and Antarctic ice sheets are the largest reservoirs of fresh water in the world, comprising 5% of the Earth's land surface with average ice depths greater than 2000 m. The best estimates put the amount of fresh water in the ice sheets and glaciers between 70–80% of the Earth's total. Of this fraction Antarctica is the largest component, with 89%, followed by Greenland with 10%, and lastly all the other glaciers and small ice caps combined amount to just 1%. If all of the frozen water on Earth were to melt, the sea level would rise by about 70 m. Even a slight thinning of 3 cm/yr in the ice sheets equates to a significant 2 mm/yr rise in the global sea level [Bindschadler, 1998b].

The Greenland ice sheet is not only a large reservoir of fresh water, it plays further roles in controlling and evidencing changes in global climate. Its height, highly reflective surface, and small amount of received sunlight combine to make the Greenland ice sheet one of the coldest places on Earth. Thus the ice sheet acts as 2000 km long, 3000 m high heat sink for the relatively warm winds accompanying the Gulf Stream, significantly influencing the circulation of the atmosphere [Bindschadler, 1998b].

The ice sheets act not only as regulators of the Earth's climate but, also of immediate importance, as key indicators of climatic change. Most global warming models include predictions of the climatic conditions on the ice sheets. To test these models an accurate assessment of how the ice sheets interact with the environment is required. This assessment is normally done at two levels: on a large scale, by measuring the *mass balance*, that is, the difference between the amount of snow that is added to the ice sheet and the amount of snow and ice lost, as discussed mass balance. On a smaller scale, the interaction between

the environment and the snowpack can also be described by the near surface structure of the ice sheet, since melting and accumulation alter the morphology of the first tens of meters of ice depth, discussed in Sec. 2.3. In Sec. 2.4 we show how satellite remote sensing, with an ERS SAR mosaic as example, can lead to greater understanding of these small-scale and large-scale processes.

2.2 Mass Balance

The mass balance of a glacier or ice sheet refers to the net gain or loss of matter, usually in the form of solid water, over time. The calculation is straightforward, in that the amount of matter lost through ablation is subtracted from the amount of matter gained through accumulation, resulting in a positive or negative figure that indicates the "health" of the glacier or ice sheet. A glacier or ice sheet in equilibrium, or "in balance," will have a mass balance of zero. While the calculation is simple enough, determining the actual amounts of accumulation or ablation is in fact quite difficult, due to incomplete spatial and temporal knowledge of the gain and loss of water.

In specifying the mass balance, the ice sheet is divided into areas of gain and loss, which typically correspond to changes in altitude, as depicted in Fig. 2.1. The accumulation area is defined as the region where matter, in the form of fallen snow, is added to the glacier throughout the year. The ablation area is defined as the region where the ice sheet has a net loss of snow and ice by run-off, calving, sublimation, or other processes. The line that divides the two areas is called the *equilibrium line*, at which point the amount lost equals the amount gained. Because of its low mean temperature, almost the entire Greenland ice sheet is accumulation area. Today the equilibrium line runs along a contour at about 1000 m elevation, which, for most of the ice sheet, is less than 100 km from the coast.

What keeps the accumulation area from growing each year and the ablation area from withering away? The ice and snow mixture that makes up the ice sheet, while composed of solid ice crystals, acts as a viscous fluid transporting mass from the interior highlands to the coast. Thus the ice sheet is in constant motion toward lower elevations due to the force of gravity, and its approximate kinetic behavior can be described by fluid dynamics equations [Paterson, 1994]. The snow and ice in the upper layers that is lost in the ablation zone,

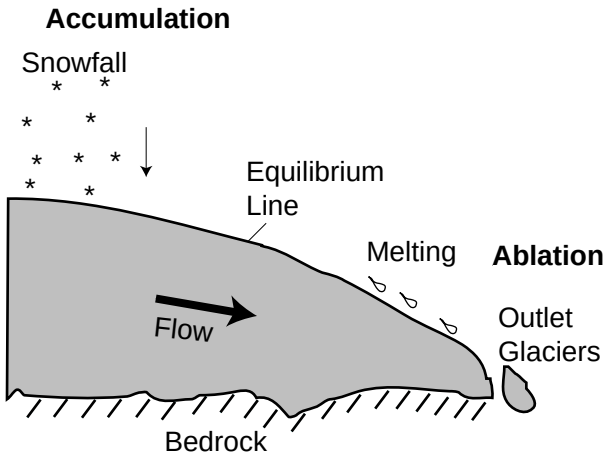

Figure 2.1: Mass balance schematic for a typical glacier. Areas of accumulation show an increase in mass due to snowfall, whereas ablation areas show a net loss due to melting or calving, among other processes. The overall shape of the glacier is maintained by the flow of ice due to gravity.

Table 2.1: Annual Mass Balance of the Greenland Ice Sheet [Weidick, 1984]

Process	**Gt**
Accumulation	500±100
Calving	205±60
Melting and run-off	295±100

then, is perpetually replenished by the ice flowing down into the area from the accumulation zone. In Fig. 2.2 we plot an elevation profile of the Greenland ice sheet at 71° N. Because of the fluid-like nature of the ice sheet, abrupt topographic variations can not be supported, and thus the interior of the ice sheet is relatively smooth. The sharp variations on the sides of the profile correspond to rocky coastal areas.

Table 2.1 shows the mass balance values for the Greenland ice sheet as calculated by Weidick [1984]. While the gains and losses sum to zero, there are large uncertainties in the measurements. Most of this error has been attributed to use of spatially sparse *in situ* data [Ohmura and Reeh, 1991; Paterson, 1994].

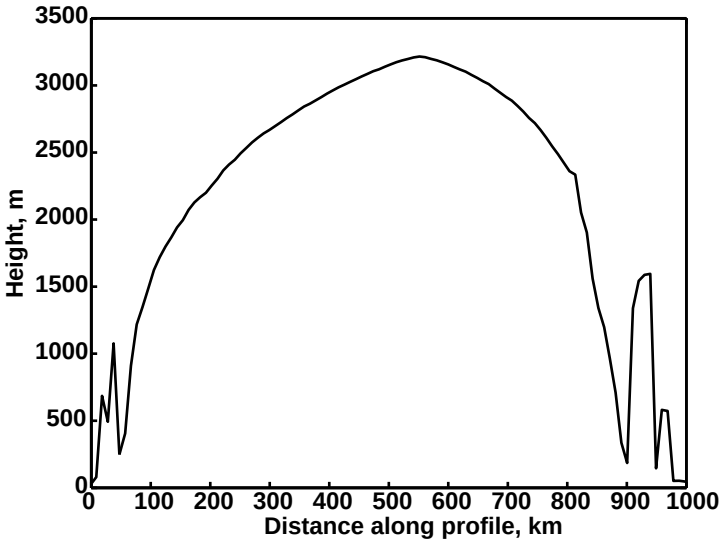

Figure 2.2: A profile of the Greenland ice sheet along latitude 71°N. Notice the lack of topographic complexity in the interior. The shape of the ice sheet profile is determined by climate conditions and the fluid characteristics of the snow pack [Paterson, 1994].

2.3 Structure of the Near-Surface

There are four different zones within the accumulation area, depicted in Fig. 2.3, as labeled by Benson [1962]. The *dry snow zone* is the coldest interior region where no melting occurs, even during the height of summer. The near surface of the dry snow zone is marked by a lack of density contrast, save for boundaries between snow layers and the snow grains themselves. Next and lower in elevation is the *percolation zone*, which is not quite as cold as the dry snow zone and in which melting on the surface occurs in the summer. The meltwater collects into puddles and then "percolates" down through the upper layers where it refreezes. Meltwater refrozen in a vertical column is called an *ice pipe*; meltwater that encounters a layer and spreads out horizontally before refreezing is called an *ice lens*. Within the percolation zone the areal number density of ice pipes and lenses varies; a range of 1–3 m^{-2} has been reported by Rignot [1995].

Closer to the coast and in the next lower altitude range lies the *wet snow zone*, where by the end of summer melting will have occurred thoughout the entire volume of snow deposited since the end of the previous summer, leaving a relatively uniform volume devoid

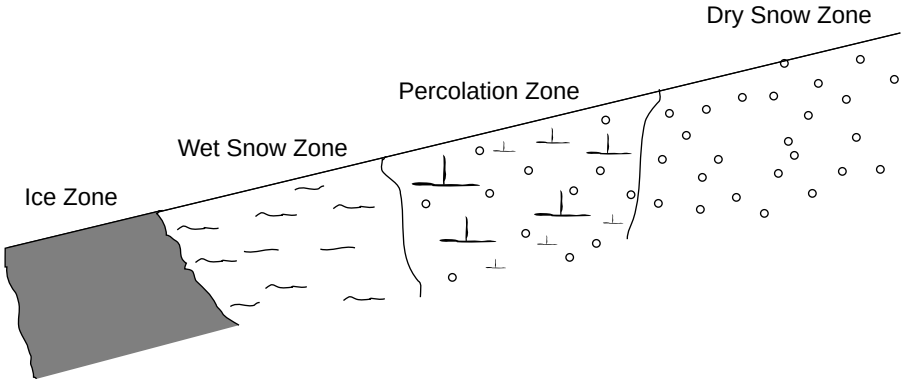

Figure 2.3: Glacial zones of the accumulation area of Greenland. The accumulation area can be divided morphologically into at least four zones. The degree and extent of summer melt within the snowpack causes the differences in internal structure depicted in the figure.

of a high degree of density contrast. Finally, at the lower limit of the accumulation zone is the *ice zone*, where so much meltwater is produced that the layers merge to form a continuous mass. In this region differentiating between annual layers is difficult at best. At the lower boundary of the ice zone lies the equilibrium line, which marks the limit of the accumulation area. Below this line there may also be solid ice, but this ice will suffer a net loss of mass from the surface each year [Benson, 1962].

In the accumulation area each year's layer is buried by successive years of snowfall. As this occurs, the snow beneath the surface slowly transforms into ice due to the increase in overlying weight, and, in the lower altitudes, also as a result of melting and refreezing. The intermediate stage of this transformation is known as *firn*. The increase in density of the firn with depth has been modeled semi-empirically by Herron and Langway [1980],

$$\ln\left(\frac{\rho_f}{\rho_i - \rho_f}\right) = a \cdot z + b, \tag{2.1}$$

where ρ_f is the density of the firn (not to be confused with the correlation coefficient, ρ, which we will discuss later), ρ_i is the density of pure ice, z is the depth, and a and b are constants.

Densification of the firn in the dry snow zone occurs in at least two stages. The first stage

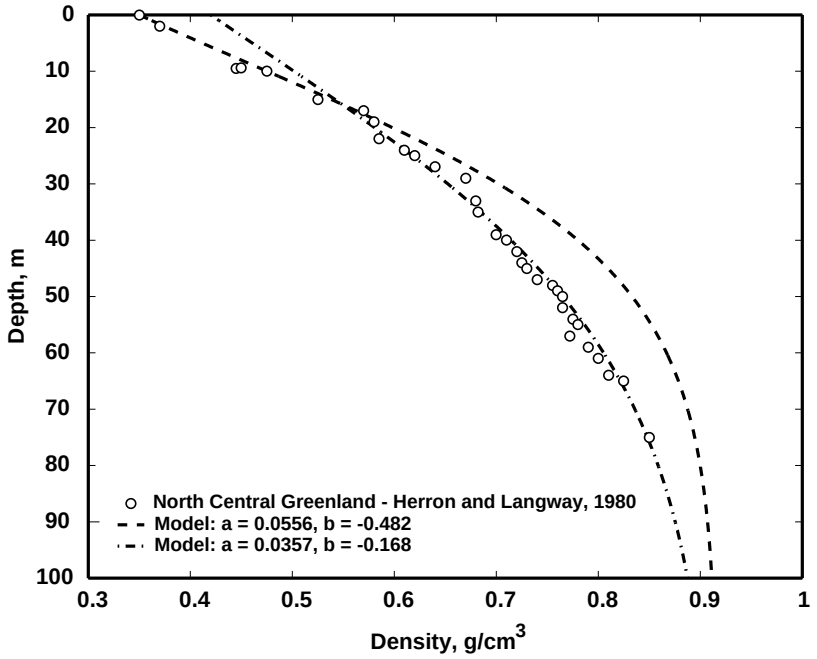

Figure 2.4: Density profile of the upper Greenland firn, from Herron and Langway [1980], with two fits of Eqn. 2.1 to the first two stages of densification. Similar density profiles can be found throughout Greenland and Antarctica [Herron and Langway, 1980].

consists of grain settling and packing, up to a critical density of about 0.55 g cm^{-3}. Densities increase more slowly in the second stage until the interconnected air passages become closed off, leaving individual air bubbles. Finally, at about 0.83 g cm^{-3}, the trapped air is slowly compressed as the density approaches that of pure ice [Herron and Langway, 1980]. Fig. 2.4 shows density vs. depth data for the first 80 meters of Greenland firn from the dry snow zone of North Central Greenland [Herron and Langway, 1980]. Following Benson [1962], we have plotted two curves from Eqn. 2.1 to match the first two stages.

Because of the contact of grains in the upper layers, there is a diffusion of molecules from each ice grain to its neighbors. In general, larger grains receive molecules from smaller grains. This process, which has importantance in the modeling of accumulation rates from SAR data [Forster, 1999], is called *grain-boundary migration* [Alley, 1990]. It results in a larger mean grain size with increasing depth, since the smaller grains eventually disappear. A plot of measured grain size vs. depth at the GISP2 site in the summit region of the

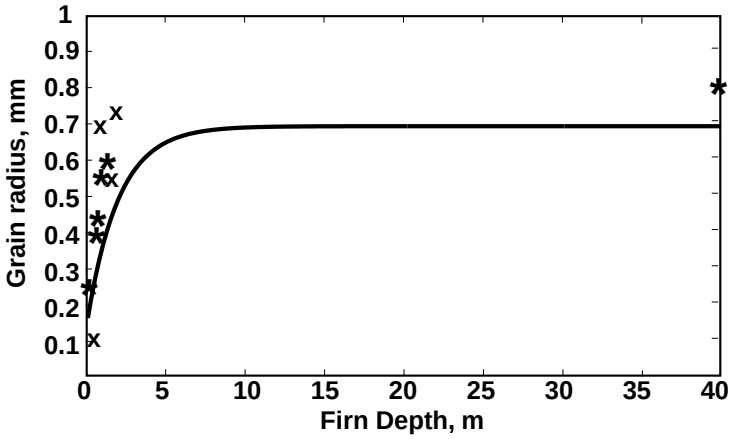

Figure 2.5: *In situ* snow grain radii vs. depth, from Woods [1994] (*) and Lytle and Jezek [1994] (x), as collected by Forster [1999]. Snow grain size is seen to increase rapidly in the first two meters, then grow at a slower rate. Solid line is from a grain-growth model developed by Forster [1999].

Greenland ice sheet is shown in Fig. 2.5, where we see that grain-boundary migration leads to a rapid increase in size in the first few meters, while the grain radius stays relatively constant over the next few tens of meters. This behavior has been modeled by Forster [1999], and the results of his model for the conditions at GISP2 (25 cm yr^{-1} water equivalent (w.e.) accumulation rate and a mean annual temperature of $-30°$ C) are plotted in Fig. 2.5 (solid line), where the grain-growth model appears to be consistent with the general trend of grain-size vs. depth.

Grain growth over time implies that in areas of low accumulation, where the grains are buried more slowly, the mean grain size will be larger at a given depth, as compared to areas of high accumulation [Jezek, 1993; Forster, 1999]. This implication can affect how radar images of the dry snow zone are interpreted, as we discuss in Sec. 2.4.

In certain circumstances, snow is transformed in a different way than detailed above. Through sublimation, coarse grains may be created within the snowpack, at a depth of a few meters, producing a porous layer of grains 2–5 mm in size. This layer is known as *depth hoar*. A strong vertical temperature gradient is needed for its formation and thus depth hoar is produced mainly during the summer months [Alley, 1990]. In Fig. 2.6 we plot a density profile of the first two meters at Summit Base Camp, Greenland, in the dry snow

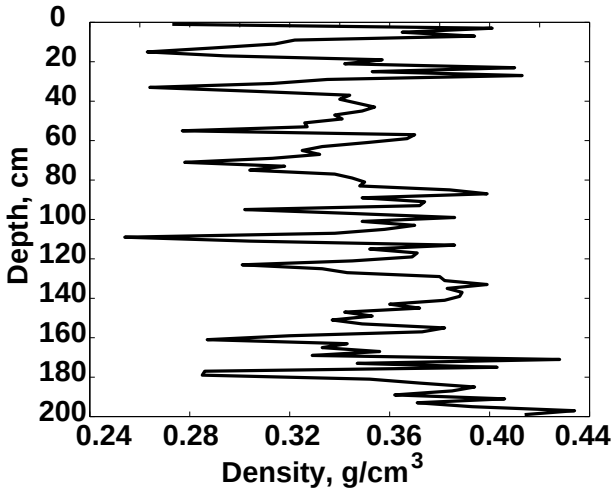

Figure 2.6: Density profile for the first two meters at Summit Camp, Greenland. The thin layers of low density correspond to depth hoar layers. Snow pit data courtesy of Chris Schuman, GSFC-NASA, 2000.

zone (Data courtesy of Chris Schuman, Goddard Space Flight Center, NASA, 2000). The thin layers of low density correspond to depth hoar layers, which mark the summer period of each annual cycle and indicate, by their separation, the amount of accumulation from year to year.

Thus there are two important structural features in the dry snow zone that are indicative of the accumulation rate: (1) the size of the snow grains and (2) the thickness of the annual layers. We discuss the relative importance of each in the interpretation of InSAR data in Chap. 6.

2.4 Remote Sensing

2.4.1 Overview

Hundreds of years of climate history, including accumulation, melting and freezing events, and wind patterns are recorded in the first ten meters of snow. *In situ* studies are able to unravel this history, but are limited in both space and time. For this reason satellite remote sensing is an essential tool for monitoring the ice sheets. Whereas *in situ* measurements

are limited spatially and temporally, interpretation of remote sensing data is hindered by the complexity of the interaction between the electromagnetic wave and the firn as well as the paucity of information retrieved for a single resolution element. In order to derive meaningful mass balance estimates then, scientists investigating the firn with space- or air-mounted sensors must be able to properly interpret the remote sensing data, which, due to the number of unknown parameters values, is not always an easy task.

Many of the remote sensing efforts for monitoring the ice sheets employ images from passive optical sensors. These visual or near-visual images are produced from sunlight reflected from the surface of the ice sheet, and thus are sensitive to the topography and the surface characteristics (e.g., new-fallen snow vs. wind crusts.) Resolutions range from 1100 m in the case the Advanced Very High Resolution Radiometer (AVHRR), to 80 m for the early Landsat satellites, to 15 m for the latest Landsat satellite (Landsat7), to 10 m for the French Pour l'Observation de la Terre (SPOT) satellite. Optical images have resulted in the first comprehensive and accurate maps of the ice sheets, as well as the capability to monitor the changes in ice sheet boundaries on a continental scale [Weidick, 1995]. Surface topography obtained from AVHRR image data using photoclinometry provides needed inputs to models of ice flow in remote areas, and has led to the discrimination and analysis of ice streams [Scambos et al., 1999]. Higher resolution images, including declassified military data, have been used to study flow bands or crevasses that have changed over time, and to thus characterize further the ice in motion [Weidick, 1995; McDonald, 1995; Bindschadler, 1998b].

The only active optical sensors employed thus far to monitor the ice sheets have been airborne laser altimeters. While laser altimeters are limited in ground coverage, they have recently been used in a repeat-pass mode over a wide grid of flight tracks to measure thickening/thinning rates of the Greenland ice sheet. [Krabill et al., 2000]. These laser measurements have been shown to be consistent with mass balance estimates achieved through GPS measurements [Thomas et al., 2000].

Passive optical data suffer limitations due to atmospheric visibility, as do laser altimeters, and also lack adequate sunlight for much of the year. Both limitations are largely overcome by the use of radio wavelength sensors. Passive microwave emissions from ice sheets have been monitored since the early 1970s, with typical resolutions of about 25 km, and have

also been successful in demarking the different accumulation and ablation zones of the ice sheet. More importantly, since microwaves can propagate many meters in dry firn, as we discuss in detail in Chaps. 5 and 6, emissivity studies at these frequencies are sensitive to the firn structure including the thickness of the annual snow layer and the sizes of grains, both of which are indicators of accumulation rate. Emissivity-derived accumulation maps have had some success in matching *in situ* data [Zwally and Giovinetto, 1995; Shuman, 1995; Abdalati and Steffen, 1998; Arthern and Winebrenner, 1998].

Active microwave sensors, or radars, including both air- and space-mounted platforms, have been employed with great success in monitoring the ice sheets. Low-frequency sounding data from airborne systems have been used to map out the geometry of the bedrock kilometers below the surface [Gogineni et al., 1998; Moussessian et al., 2000]. Radar altimetry studies have successfully provided 2 km resolution DEMs for both Greenland [Ekholm, 1996] and the region of Antarctica north of 82° [Bamler, 1994]. Incoherent scatterometery data have characterized the backscattering efficiency of the polar firn for all polarizations and for a wide range of incidence and azimuthal angles [Rott et al., 1993; Long and Drinkwater, 1994; Rott and Rack, 1995; Wismann et al., 1997; Long and Drinkwater, 2000]. But it has been spaceborne SAR systems, especially InSAR systems, that have proven to be advantageous on the largest number of geophysical fronts. SAR/InSAR systems combine the all-condition viewing of other microwave sensors with resolutions that are comparable to those of satellite optical instruments. Thus, they are not affected by clouds or darkness and can provide information on horizontal variations of the ice sheets on the scale of ~20 m. Furthermore, like other microwave sensors, InSAR/SAR instruments are sensitive to the sub-surface structure.

2.4.2 ERS SAR Mosaic

The remainder of the dissertation is devoted to SAR and InSAR imaging capabilities in regards to the ice sheets; however, for illustrative purposes, below we provide an example of SAR remote sensing of the Greenland ice sheet, which has direct bearing on this dissertation.

An ERS SAR mosaic of the ice sheet is shown in Fig. 2.7(a), courtesy of the National Snow and Ice Data Center (NSIDC) and M. Fahnestock, GSFC-NASA, 1999. The brightness of the image indicates the relative amount of 5.6 cm wavelength energy scattered back to

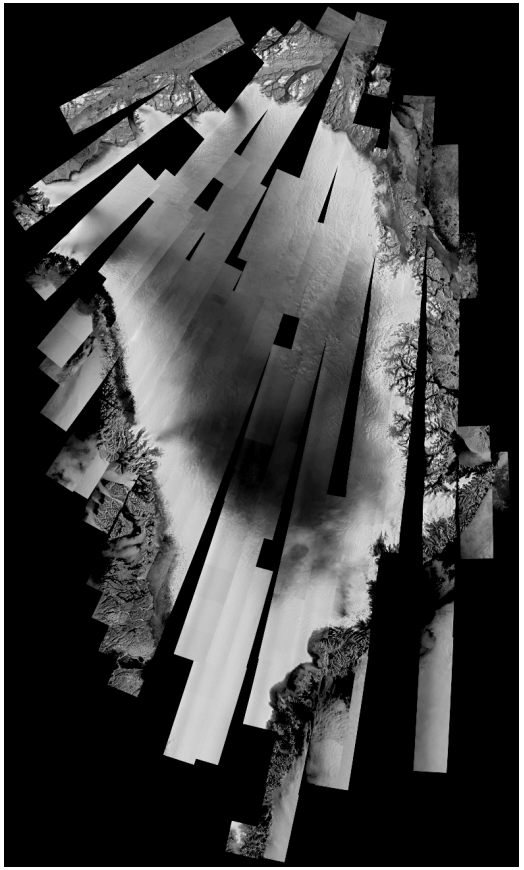

(a) ERS SAR Mosaic of Greenland

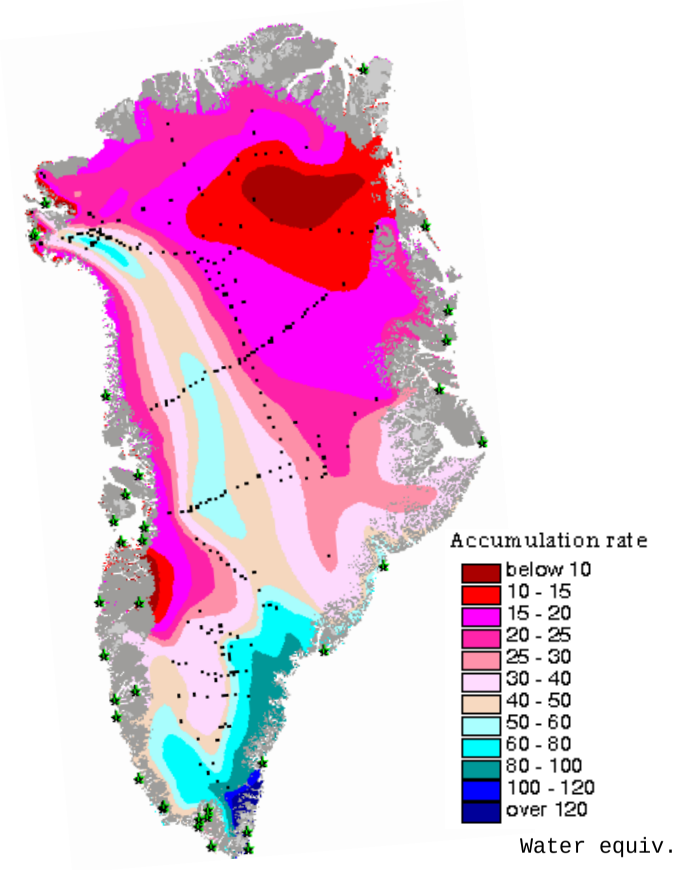

(b) Greenland Accumulation Map

Figure 2.7: An ERS SAR mosaic of the ice sheet, courtesy of the National Snow and Ice Data Center (NSIDC) and M. Fahnestock, GSFC-NASA, 1999, is shown in (a). . The mosaic was created from August 1992 observations. The dry snow zone and percolation zones are clearly distinguishable as the dark interior and surrounding bright region, respectively. Wet-snow and ice zones can be seen as the dark region closest to the rocky coast. A Greenland accumulation map is shown in (b), where the units are in centimeters per year of water equivalent [Ohmura and Reeh, 1991]. Over the northern half of the Greenland ice sheet most of the precipitation occurs west of the summit, due to the predominant direction of motion of moisture-bearing storms. Within the dry snow zone an inverse relationship between backscatter and accumulation can be seen, possibly owing to differences in snow grain size [Jezek, 1993; Forster, 1999; Munk et al., 2001].

the radar. The ice sheet, which to the eye would appear almost uniformly bright, shows dramatic contrast in this image. The dark interior of the image corresponds to the dry snow zone, where the dominant scatterers are limited to the snow grains and the annual snow layers. The bright region that surrounds it corresponds to the percolation zone, where the presence of ice pipes and ice lenses provides relatively large scatterers having a large degree of density contrast with the surrounding medium. At the very edge of the ice sheet are the wet snow, ice, and ablation zones, which also appear darker in the image. The observations that comprise this mosaic were taken in August 1992, when the presence of liquid water would be possible in these outer areas. Liquid water acts as a conductor to the cm-scale wavelength radiation, thus absorbing or forward scattering most of the signal from the SAR satellite. Since minimal amounts of energy are scattered back to the radar, regions where meltwater is present appear dark in the SAR image.

Thus, using SAR, we are able to discriminate between the zones, especially between the dry snow and percolation zone, due to the order of magnitude difference in the amount of sub-surface energy that is scattered back to the radar. The extent of these zones, quantified by the radar, has important implications for climate monitoring, as changes in climate result in changes in the position of the zonal boundaries [Bindschadler, 1998b].

Within the dry snow zone, we can see a subtler variation in the amount of backscatter. The darkest region is in the south-west, while the north-east is brighter by about a factor of two. This difference has been attributed to differences in accumulation rates [Jezek, 1993; Forster, 1999], the contours of which, as seen in Fig. 2.7(b), roughly match the gradations in backscatter. The south-west region of the dry-snow zone has a higher accumulation rate because the snow-bearing storms arrive from the south-west, impact the high plateau of the summit region, and deliver their precipitation to this region. The north-east section of the dry snow zone is in a snow "shadow," and receives little snowfall. Jezek [1993], Forster [1999], and Munk et al. [2001] have posited that the regions of low accumulation rate have high backscatter due to the larger snow grains at depth in these regions, as explained in Sec. 2.3. Larger snow grains have a larger radar cross-section and thus scatter more energy back to the radar than smaller grains, as we discuss in Chap. 6.

Since the ERS signal penetrates into the firn, scientists are not only able to classify the different regions of the ice sheet, but also can infer a very important geophysical parameter,

accumulation rate. Our understanding of the ice sheet and our means to characterize it thus is dependent on the penetration depth of the radio signals, which we we discuss in detail in the following chapters.

Chapter 3

SAR and InSAR

3.1 Overview

In this chapter we introduce synthetic aperture radar (SAR) and interferometric SAR (InSAR) and define interferometric phase, which results from the difference in distances from the radar to the ground in the two images comprising the interferogram. In Chap. 4 chapter we focus on correlation, a property of interferometric radar images that we relate explicitly to the geophysical structure of the ice. Many of the sources of decorrelation in interferometric images are dependent on details of the SAR or InSAR imaging systems, and thus a general understanding of the various parameters used in SAR/InSAR image formation are necessary before discussing interferometric correlation.

3.2 Introduction to spaceborne SAR

3.2.1 Terminology

A spaceborne or airborne SAR illuminates the Earth's surface in a side-looking fashion as depicted in Fig. 3.1. Due to the shape of the antenna beam pattern at a single point in time the illumination of the terrain is confined to an area called the *antenna footprint*. As the SAR moves at velocity V along its (assumed) straight path at an altitude H above the ground, it illuminates a *swath* of the terrain by transmitting a series of microwave pulses at a rate called the pulse repetition frequency, or PRF. The SAR receiver detects coherently the stream of echoes reflected back from the Earth and separates it into individual echoes, each corresponding to a single transmitted pulse.

Echoes are produced because the terrain consists of *scatterers*, which are objects, such

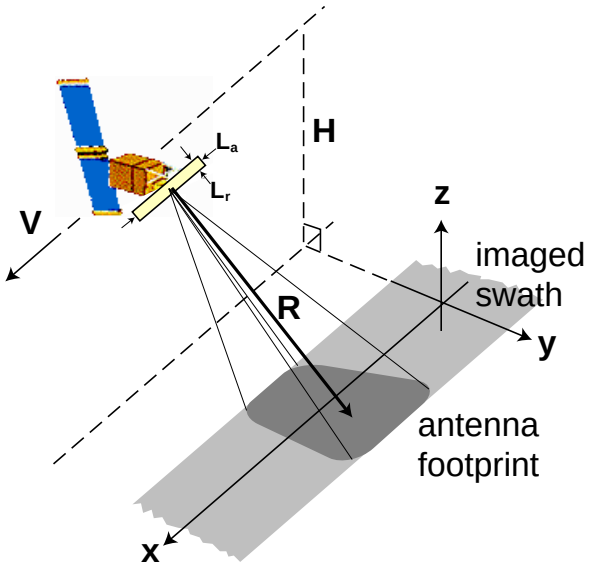

Figure 3.1: The SAR viewing geometry, for a left-looking radar. The parameters above are described in the text. The antenna footprint is the size the antenna beam on the ground. The swath width is the size of the antenna footprint in the ground range direction.

as trees, the ground, or glacial ice, for example, that interact with the incident radiowave. Since SARs transmit and receive signals at (nearly) the same location in space, the interactions that are of importance in the SAR geometry are reflections of the incident wave *back* towards the radar. This type of interaction is called *backscattering*, and the scatterers involved are called *backscatterers*. In this dissertation, unless otherwise stated, we assume "backscatterer" when we write "scatterer". A good or efficient scatterer reflects more energy than a poor or inefficient one. Moreover, the transmit signale, and the echo that is received from a particular scatterer will be *complex*, that is, having both amplitude and phase. The echo amplitude is determined by the efficiency of the scatterer, as well as system and geometric factors. For simple scattering interactions the echo phase is determined by the phase of the transmit signal, the dielectric properties of the interveaning medium, and the position of the scatterer relative to the SAR.

Two different scanning mechanisms are employed to image the terrain. First, as each transmitted pulse sweeps across the swath, i.e., in the direction perpendicular to the flightpath or *across-track*, the terrain reflects energy back to the radar. Since typical terrain

has a continous placement of scatterers, the reflected energy is in the form of a continuous echo. This echo is digitized in time at a sampling frequency f_s. Simultaneously the scene is scanned in the flight direction, i.e., *along-track*, at the speed of the platform motion.and digitized at the PRF. The time scales of the across-track and along-track mechanisms differ from each other by several orders of magnitude, which allows us to consider them independently [Bamler and Hartl, 1998]. The raw SAR data — and later the focused SAR image — is in the form of a 2-D matrix, with the coordinates being *range* R for the distance from the SAR and *azimuth* x for the position of the scatterer along the sensor path, as depicted in Fig. 3.1. To specify the component of range in the y direction, the term *ground range* is used, and the range R is often called in contrast *slant range* to distinguish the two.

A bin in the 2-D matrix constitutes a *pixel*. In the case of raw SAR data, each pixel will have a complex value, that is, having both amplitude and phase, or real and imaginary components, depending on the convention used. Due to the sampling procedures decribed above, each pixel also has an associated size in range and azimuth. In azimuth the pixel size is $V \cdot PRF$ and in slant range it is $\frac{c}{2f_s}$. The total size in azimuth and range of the 2-D matrix is called the *scene* size. Averaging pixels together to create a smaller 2-D matrix increases pixel size, as we discuss in Sec. 3.2.4, but the scene size remains constant.

The pixel size should not be confused with the *resolution* size. The resolution of the image indicates the spatial extent of the scatterers whose echoes contribute to the measured pixel value. More simply, resolution is described by the "sharpness" of the image. A larger resolution size implies a coarser resolution and a blurry image; conversely, a smaller resolution size implies a finer resolution and a sharper image. While we normally attribute a single value to the resolution size, the resolution is actually defined by the 2-D *impulse response* function, $W(x, R)$. The impulse response is centered on the center of the pixel and in principle extends to infinity in both the range and azimuth directions. Each pixel has an associated impulse response, though typically the impulse responses are indentical or nearly indentical across the SAR image. A representative 1-D impulse response and pixel width are shown in Fig. 3.2. The resolution size is typically defined by the width of the impulse resonse at the half-maximum point, and is in general larger than the pixel size.

In theory echoes from all scatterers will contribute to the value, or return *signal*, of each pixel. The impulse response governs the weighting applied to each of these echoes, based

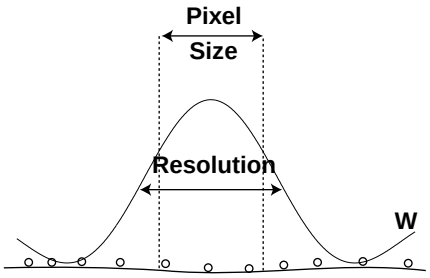

Figure 3.2: Pixel size vs. resolution size, for an impulse response function W. The circles represent surface scatterers that contribute to the return echo.

on their time of arrival. It is perhaps easier to describe the impulse response weighting by the *position* of the scatterer rather than the echo delay time. Scatterers that are close to the resolution center will have the most weighting, while those a long distance away will have minimal weighting. Also, neighboring impulse responses overlap each other. Thus a single scatterer will contribute to many different pixels. This is the reason why a very bright scatterer can appear in several neighboring pixels.

The goal of SAR processing is to decrease the resolution size so that the image is as sharp as possible. We describe the steps below.

3.2.2 SAR imaging

The resolutions in range and azimuth for a raw radar image will be poor, and in general the unprocessed data for orbiting SARs appear similar to noise. The unprocessed range resolution, R_{r}, will be governed by the duration of the transmitted pulse, τ_{p}, and the speed of light c,

$$R_{\mathrm{r,unprocessed}} = \frac{c\,\tau_{\mathrm{p}}}{2}. \tag{3.1}$$

The unprocessed range resolution for the ERS system and will be on the order of 5 kilometers.

The unprocessed azimuth resolution, on the other hand, will be determined by the

antenna footprint size, or,

$$R_{\mathrm{a,unprocessed}} = \frac{R\,\lambda}{L_{\mathrm{a}}}, \tag{3.2}$$

where L_{a} is the length of the antenna parallel to the flight track as shown in Fig. 3.1, and λ is the wavelength. A typical value for L_{a} for a space-borne radar is 10 meters, thus resulting in unprocessed azimuth resolutions also of about 5 kilometers.

With signal processing techniques, however, "focused" image resolutions of only a few meters can be achieved. In range this is often done by first slewing the signal through a range of frequencies before transmission, creating a *chirped* pulse. The spread of frequencies in each pulse creates for a greater bandwidth BW than would a monochromatic pulse with the same pulse duration. Secondly, the return echo is *matched-filtered*, meaning that it is convolved with the time-reversed pattern of the transmitted pulse. Matched-filtering allows for the range resolution to decrease to

$$R_{\mathrm{r,focused}} = \frac{c}{2\,BW}. \tag{3.3}$$

For ERS, the resulting *compressed* range resolution is less than 10 m.

A similar filtering process is used in the azimuth direction, but in this instance the spread in frequencies results from the interaction of the radiowaves with the ground – the well-known Doppler shift phenomenon – rather than from the transmitter. Echoes reflected from terrain in front of the moving sensor are shifted to higher frequencies than those reflected from behind. This Doppler spread is in essence a motion-induced chirp, and the same matched-filtering techniques that were used for range can now be employed to decrease the azimuth resolution size to a few meters.

We can consider this refinement in azimuth resolution as equivalent to an increase in the size of the aperture. Since the antenna footprint as shown in Fig. 3.1 is larger than the distance the radar travels between pulses, a single scatterer, say a rock or tree, is illuminated by the radar in a succession of locations along the radar flight path, as depicted in Fig. 3.3. With correct bookkeeping of the phase history of each scatterer, we can *synthesize* a larger

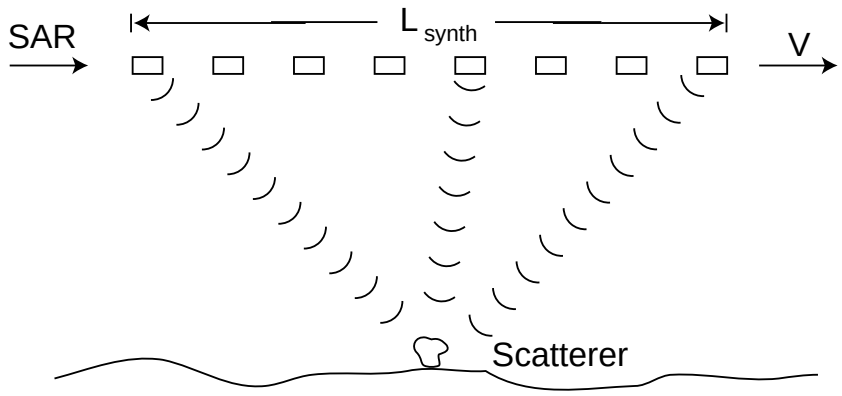

Figure 3.3: The synthetic aperture. By coherently combining echoes from different positions along-track, a virtual aperture much larger than the physical size of the antenna is created.

virtual aperture by combining coherently the echoes from many pulses. This is analogous to a phased-array antenna system, where in this case each element of the array is the SAR system at one point in time. As it turns out, the focused azimuth resolution is governed by the size of the antenna as was the unprocessed resolution discussed above, but in this case it is

$$R_{\mathrm{a,focused}} = \frac{L_{\mathrm{a}}}{2}. \tag{3.4}$$

Shorter antennas yield finer resolutions because a single point on the ground will be illuminated for a longer time. Of course, signal-to-noise considerations become important if the antenna is too small. What is perhaps surprising is that no other parameter, such as range, platform velocity, or wavelength, enters into the equation for theoretical azimuth resolution. This result is the fundamental aspect of synthetic aperture radar and is why SAR has such powerful imaging capabilities, especially for spaceborne systems orbiting hundreds or thousands of kilometers above the Earth or other planets.

To this point we have assumed that the radar pointing is fixed and oriented perpendicular to the flight path. This imaging geometry is called *strip-map* mode. Within the strip-map mode, nonetheless, there will be slight variations of the antenna pointing, such that there

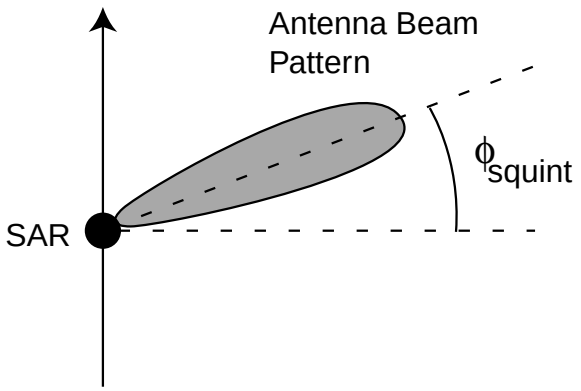

Figure 3.4: Squint angle definition. "Squint" is the amount of angular offset between the antenna boresight and the line perpendicular to the flight path. Here the view is from above.

will be some *squint* angle ϕ_{squint} that will cause the SAR to look either slightly forward or backward, as depicted in Fig. 3.4. This will cause the raw data to have a non-zero *Doppler centroid*, meaning that the middle of the antenna beam will now not be centered directly perpendicular to the flight path, or towards the locus of zero Doppler shift. In terms of SAR processing, there are few consequences of antenna squinting, as the positive or negative carrier frequency associated with the Doppler centroid can be eliminated by filtering techniques. However, for interferometry, there is at least one deleterious effect of having different Doppler centroids in the two observations, as will be discussed in Chap. 4.

A much more comprehensive description of SAR image formation can be found in Curlander and McDonough [1991], among many other texts.

3.2.3 Geometry of the SAR Impulse Response

It was stated above that the impulse response assigns its weights based on the echo delay time, but delay time is often mapped into azimuth and range values. Thus, instead of $W(t)$, we consider $W(x, R)$. Since range and azimuth are separable, $W(x, R)$ can be broken up into its multiplicative parts,

$$W = W_{\text{a}}(x - x_0)W_{\text{r}}(R - R_0), \tag{3.5}$$

where $W_{\rm a}$ and $W_{\rm r}$ are the impulse responses in the azimuth and range directions, respectively, and x_0 and R_0 are the corresponding distances to the center of the resolution element. Due to the common practice of using a square spectral window in the data processing, the typical impulse response of a SAR system is a sinc-like function [Zebker and Villasenor, 1992], for example,

$$W_{\rm a}(x) = \mathrm{sinc}\left(\frac{x - x_0}{R_{\rm a}}\right) \tag{3.6}$$

and

$$W_{\rm r}(R) = \mathrm{sinc}\left(\frac{R - R_0}{R_{\rm r}}\right), \tag{3.7}$$

where $R_{\rm a}$ and $R_{\rm r}$ are the azimuth and range resolution sizes, respectively. As stated earlier, for a processed SAR image, $R_{\rm a}$ is determined by the along-track antenna size $L_{\rm a}$, while $R_{\rm r}$ is determined by the bandwidth BW. The above sinc-function is defined as

$$\mathrm{sinc(q)} = \frac{\sin(\pi\, q)}{\pi\, q}. \tag{3.8}$$

Because we wish to relate the radar response to the three-dimensional geometry of the terrain, we need to express results in terms of a rectilinear rather than azimuth-range coordinate system. Since the x coordinate does not change between the systems, we consider the 2-D (y, z) problem only. We assume, for the moment, a non-refractive scattering medium, as shown in Fig. 3.5, where y_0 and z_0 are the distances to the center of the resolution element and θ_0 is the angle the range vector makes with the vertical. We have assumed a planar geometry and therefore θ_0 is equivalent to the *look angle*, which is defined as the angle the antenna pointing makes with the vertical.

Assuming that the radar is far away from the terrain, the (y, z) position of a scatterer can be mapped into range R by

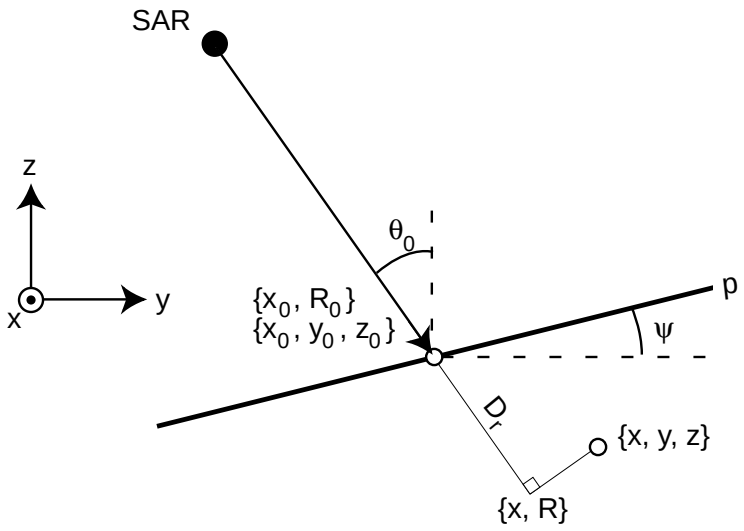

Figure 3.5: The geometry of range resolution in the (x, y, z) coordinate system. The parameters shown above are explained in the text. The amount of weighting that the impulse response applies to an echo from an individual scatterer is determined by its position x, y, z projected on the range direction, D_r

$$R(y,z) = y \sin\theta_0 - z \cos\theta_0. \tag{3.9}$$

Then,

$$R(y,z) - R_0 = (y - y_0) \sin\theta_0 - (z - z_0) \cos\theta_0, \tag{3.10}$$

which can be substituted into Eqn. 3.7 to find $W_{\rm r}(y,z)$.

The difference $R(y,z) - R_0$, which we label as $D_{\rm r}(y,z)$, is a fundamental variable of SAR and InSAR, for it determines both the phase of the echo from the scatterer relative to resolution center and the amount of weighting that is applied by the impulse response.

Hence

$$W_r(y,z) = sinc\left(\frac{(y-y_0)\,\sin\theta_0 - (z-z_0)\,\cos\theta_0}{R_r}\right). \tag{3.11}$$

For most applications we are mainly concerned with the range resolution as projected on the ground. If the surface is horizontal, then

$$W_r(y) = sinc\left(\frac{y\,\sin\theta_0}{R_r}\right). \tag{3.12}$$

If there is a tilt to the terrain, a simple rotation yields

$$W_r(p) = sinc\left(\frac{p\,\sin\theta}{R_r}\right). \tag{3.13}$$

where p is the component of R along the (tilted) ground. Here $\theta = \theta_0 - \psi$, where ψ is the tilt of the terrain from the horizontal towards the radar, as shown in Fig. 3.5. As ψ approaches θ_0, the range resolution on the ground increases. There will be a similar increase in the size of the pixel on the ground. This increase is one reason why the sides of hills towards the radar are brighter and *foreshortened* [Curlander and McDonough, 1991].

For the rest of this dissertation we will assume that the surface is horizontal, that is, defined by $z = 0$, and therefore θ is both the angle of incidence and the angle the incoming radiation makes with the vertical. For the ice sheets this is valid assumption, as deviations $> 1^\circ$ from the horizontal are not found in the interior of the Greenland ice sheet. In any event, solutions for tilted geometries can be found by the simple substitutions above.

Impulse responses other than a sinc-functions are possible, of course, depending on the spectral filtering techniques used for side-lobe reduction or for increasing correlation. In general spectral filtering will tend to increase the resolution size. Most of the interferometric data presented in this dissertation were processed at JPL using a Kaiser window, as defined by Oppenheim and Schafer [1989], with Kaiser parameter $\beta = 2.12$ [Werner, 1999]. In Fig. 3.6 we plot W for the square and Kaiser spectral windows. The ramifications of spectral filtering on the interferometric correlation will be discussed in Chap. 4.

In the case where the scattering medium is a dielectric volume which alters the velocity

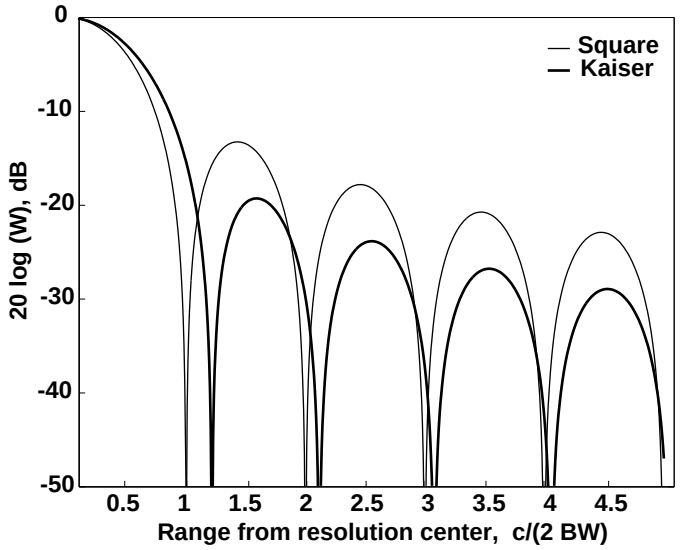

Figure 3.6: Impulse responses for square and Kaiser windows, assuming Kaiser parameter β of 2.12. The abscissa is the distance from the center of the resolution element in the range direction. Note that the Kaiser window produces lower primary sidelobes but a wider main lobe.

of light, such as the ice and snow mixture in the upper firn of the Greenland ice sheet, then the shape of the impulse response within the medium will be affected. It is straightforward to show that

$$D_r(y,z)_{firn} = (y - y_0)\ \sin\theta - \sqrt{\epsilon}(z - z_0)\ \cos\theta_r, \tag{3.14}$$

where ϵ is the relative permittivity of the medium, which is assumed constant throughout. In the firn there will of course be fluctuations in the permittivity, but we view these fluctuations as embedded scatterers. θ_r is the refracted angle in the medium, defined by Snell's law:

$$\sin\theta = \sqrt{\epsilon}\sin\theta_r. \tag{3.15}$$

The impulse response within the medium is then

$$W_r(y,z)_{firn} = W_r\left(\frac{(y-y_0)\,\sin\theta - \sqrt{\epsilon}(z-z_0)\,\cos\theta_r}{R_r}\right), \tag{3.16}$$

where W_r is the range impulse response as determined by the window filter. The y component of W_r remains unchanged in the medium, and if we consider surface scattering only, then this expression collapses to Eqn. 3.12.

3.2.4 Pixels

The sizes of pixels in SAR images are determined by the azimuth and range sampling frequencies. In azimuth the pixel size is $V \cdot PRF$ and in (slant) range it is $\frac{c}{2f_s}$. On the ground this corresponds to 4 and 20 m respectively for the ERS system, as listed in Tab. 1.1. To create pixels that have the favorable property of being "square", i. e. with equal range and azimuth dimensions, 5 adjacent pixels are averaged together in azimuth for every 1 pixel averaged in range, resulting in a final pixel that is roughly 20 m x 20 m. Further averaging is often done to reduce the size of the files and to decrease noise. Therefore each pixel in a SAR image may be the average of 80 or more pixels. The trade-off with this method of spatial averaging is that, while the file sizes and noise fluctuations are smaller, the pixel sizes and resolutions are larger. Averaging adjacent pixels is also called "taking looks" or "multi-looking". There are other methods of taking looks, such as averaging repeat observations of the same scene, which is how the phrase "taking looks" is derived.

The size of a pixel is not the same as the resolution size. As stated above, the pixel size is determined by the azimuth and range sampling frequencies, while the SAR resolutions will be determined by the length of the antenna (azimuth) and the bandwidth (range.) Usually the pixel size will be smaller than the resolution size, as shown in Fig. 3.2, hence scatterers outside the pixel will contribute to the amplitude and phase of a given pixel. Thus adjacent pixels can not be considered to be (completely) independent, in a statistical sense. This has favorable and unfavorable consequences. In InSAR, we co-register two images and are forced to interpolate between pixels, and thus the non-independence of adjacent pixels is necessary [Bracewell, 1986]. However, to calculate the theoretical expected values of the InSAR or SAR observables in multi-looked images is complicated because neighboring pixels

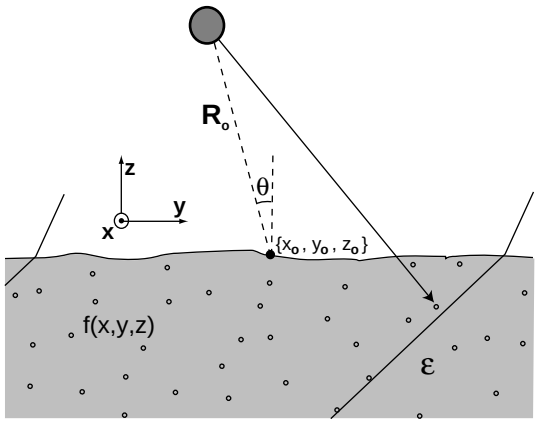

Figure 3.7: The SAR scattering geometry for a volume of point scatterers embedded within a dielectric medium. Here the surface is assumed horizontal and smooth, and the relative permittivity of ϵ.

cannot be considered independent. We will discuss this last point in Chap. 4.

3.2.5 SAR scattering characteristics

Let us model the expected return from a single representative pixel of a focused SAR image. Though radiowave scattering from most terrain is restricted to surface scatter, this is not necessarily the case for ice and snow terrain, and so we will consider scattering from a volume, defined by a reflectivity function $f(x, y, z)$, as depicted in Fig. 3.7.

We can assume that the phase due to the Doppler shift has been eliminated in our processing. Thus the position of the scatterer in the azimuth x direction (out of the page) does not affect the resultant, post-processed phase. The phase of each individual sub-echo then is determined by the projection of the position of the scatterer onto the range direction, and the amplitude by the value of $f(\cdot)$ modulated by W. The echo for a scatterer in at a position (x, y, z) is then

$$s_{scatterer}(x, y, z) = f(x, y, z)e^{-j\frac{4\pi}{\lambda}(R_0 + y\,\sin\theta - \sqrt{\epsilon}z\,\cos\theta_r)} \cdot W_a(x)W_r(y, z), \tag{3.17}$$

where $W_r(y, z)$ is $W_r(y, z)_{firn}$. The total complex echo for this pixel is the summation of

all of the echoes from scatterers:

$$s = \iiint f(x,y,z)e^{-j\frac{4\pi}{\lambda}(R_0+y\sin\theta-\sqrt{\epsilon}z\cos\theta_r)} \cdot W_a(x)W_r(y,z)dxdydz. \tag{3.18}$$

Since the cm-scale wavelength of the radiation is small compared to the size of the resolution, in order to determine *a priori* the resultant phase and magnitude of s, the position and strength of each scatterer must be known precisely, a requirement which can never be met for natural *distributed* scenes. There are many realizations leading to the same resultant amplitude and phase for each pixel, and hence the reflectivity function f and the return echo s are best treated as random processes.

Gaussian scatterers are those that include a sufficiently high number of randomly-placed scatterers within a resolution cell, such that the central limit theorem may be used to estimate the scene scattering statistics reasonably well. It is necessary that no single scatterer dominates the others. If these conditions are met s will be a complex circular Gaussian random variable. The Gaussian assumption is true for most natural terrain such as forests, fields, rough water, soil or rock surfaces, and ice and snow. It is violated if only a few dominant scatterers are present in a resolution cell such as man-made corner reflectors or if the SAR system is sufficiently high-resolution.

Due to the large number of scatterers with random phase contributing to the return echo, the phase of a SAR pixel is random, though deterministic. By this we mean that the phase is a random variable from 0 to 2π, and without other information gives no insight into the terrain; however, if we were to repeat the experiment with the same radar in the same geometry we would expect the same resultant phase.

The fact that the phase carries no information in a SAR image is the reason that SAR images are displayed in terms of amplitude or power. Consider next the power of a resolution element in a SAR image, which can be represented by

$$ss^* = \iiint \iiint f(x,y,z)f^*(x',y',z') \cdot e^{-j\beta(y,z,y',z')}$$
$$\cdot W_a(x)W_a^*(x')W_r(y,z)W_r^*(y',z')dxdydzdx'dy'dz',$$

where

$$\beta(y, z, y', z') = \frac{4\pi}{\lambda}(\sin\theta(y - y') - \sqrt{\epsilon}\cos\theta_r(z - z')). \tag{3.19}$$

We assume that the reflectivity function is a white random process with autocorrelation function

$$\langle f(x, y, z) f^*(x,' y', z')\rangle = \sigma_v(x, y, z)\delta(x - x', y - y', z - z'), \tag{3.20}$$

where $\sigma_v(x, y, z)$ is the *volumetric radar cross-section* [Hagberg, 1994; Askne et al., 1997]. It represents the radar cross section per unit volume and is measured in m^2m^{-3}. The expression above is derived in Appendix A.

In practice, even with rough surfaces, there will be some *correlation length* associated with the terrain. For example, a correlation length of 6 cm was found for the layered interfaces of the Greenland firn by Long and Drinkwater [1994]. If we consider the individual snow grains, the correlation length is approximately 1 mm, or the size of one grain. Since the size of the resolution cell is a few to tens of meters, then the δ function in Eqn. 3.20 assumption is a good one.

The expected power for the representative pixel then reduces to

$$\langle ss*\rangle = \iiint \sigma_v(x, y, z)|W_a(x)|^2|W_r(y, z)|^2 dxdydz. \tag{3.21}$$

In Fig. 3.7 we show the representative first nulls of the range impulse response by the black lines, given by Eqn. 3.16. It is obvious from the figure and from Eqn. 3.21 that if scattering from the medium extends without loss to an infinite depth, then the power return for a given pixel will be infinite. However, the ice/snow medium will have some loss associated with it, due to both scattering and absorption, and the depth to which the radiowave penetrates will be restricted. We examine two special cases below.

Surface scatter

When all of the scattering is concentrated at the surface (e.g. at $z = 0$), then the volumetric backscatter coefficient will be

$$\sigma_v(x, y, z) = \sigma^0(x, y)\delta(z), \tag{3.22}$$

where $\sigma^0(x, y)$ is the dimensionless normalized radar cross section. There have been many studies into the measured and theoretical values of σ^0 for various natural surfaces (see, for instance, Ulaby et al. [1981].)

We assume over the width of the resolution element that $\sigma^0(x, y)$ is constant. Then

$$\langle ss* \rangle = \iiint \sigma^0 |W_a(x)|^2 |W_r(y, z = 0)|^2 dxdy, \tag{3.23}$$

and thus

$$\langle ss* \rangle \approx \frac{\sigma^0 R_a R_r}{|sin\theta|}. \tag{3.24}$$

At this point we must explain our units in this derivation, as $\langle ss* \rangle$ is in units of area, not power. In fact this is reasonable, as the expression in Eqn. 3.24 is simply the radar cross section σ of the terrain as found in the radar equation [Curlander and McDonough, 1991]:

$$P_r = \frac{P_t G}{4\pi R_0^2} \cdot \sigma \cdot \frac{A_r}{4\pi R_0^2}, \tag{3.25}$$

where P_r and P_t are the received and transmitted powers, respectively, G is the antenna gain (including system losses), A_r is the effective area of the antenna, and σ is the radar cross section of the target. For distributed targets, σ is usually expressed in terms of the normalized radar cross section:

$$\sigma = \sigma^0 A_i, \tag{3.26}$$

where A_i is the illuminated surface area. In our case A_i is simply the size of the resolution cell on the ground,

$$A_i = \frac{R_a R_r}{|sin\theta|}. \tag{3.27}$$

Therefore in our modeling of the power return for one resolution element we have omitted the system parameters and geometrical power loss in Eqn. 3.25. Instead we have concentrated on σ, since all of the scattering information is contained within it. However, to convert from the pixel value in the SAR power image to σ^0 we need the values of the parameters in Eqn. 3.25.

Exponential loss within medium

If instead of surface scatter the medium exhibits volume scatter, then the depth-dependency of the volumetric scattering coefficient must be taken into account. Several possibilities exist; for instance the scattering could be confined to a layer of a given thickness. This would be characteristic of floating ice, for example. For the ice sheets what is perhaps more appropriate is that the medium is an isotropic, infinite half-plane, with a constant extinction coefficient κ_e. The extinction coefficient embodies both scattering and absorption losses [Ulaby et al., 1981]:

$$\kappa_e = \kappa_s + \kappa_a, \tag{3.28}$$

where κ_s and κ_a are the the scattering coefficient and the absorption coefficient, respectively. The degree of loss in the medium is also commonly expressed by the penetration depth d, which is equivalent to $1/\kappa_e$. The penetration depth and how it relates to correlation will be discussed in greater detail in Chap. 4.

Now the volumetric backscatter coefficient, for a negative z within the medium, becomes

$$\sigma_v(x,y,z) = \sigma_v^0 \exp\left(\frac{2z\kappa_e}{\cos\theta_r}\right), \tag{3.29}$$

where we have assumed that throughout the medium the volume backscatter coefficient σ_v is constant ($= \sigma_v^0$) , except for the decrease caused by travel within the lossy medium. Then the return power for the pixel is

$$\langle ss* \rangle = \iiint \sigma_v^0 e^{\frac{2z\kappa_e}{\cos\theta_r}} |W_a(x)|^2 |W_r(y,z)|^2 dxdydz \tag{3.30}$$

$$\langle ss* \rangle \approx \frac{\sigma_v^0 R_a R_r \cos\theta_r}{2\kappa_e |\sin\theta|}. \tag{3.31}$$

Often a SAR image will be represented by equivalent σ^0 values regardless of whether surface scattering or volume scattering dominates. For the ice sheets σ^0 ranges from almost unity to -15 dB. For the cases modeled above, we can equate the two results to find a relation between σ^0 and the volume scattering parameters:

$$\sigma^0 = \frac{\sigma_v^0 \cos\theta_r}{2\kappa_e}. \tag{3.32}$$

From Eqn. 3.32 it would appear that an arbitrarily high value of σ^0 is possible, based on a high value of σ_v^0 or alternatively a low value of κ_e. But σ_v^0 and κ_e are not independent, as we will discuss in Chap. 6.

3.2.6 Speckle

As stated above, the *pdf* for the phase of a SAR pixel is uniform due to the summation over many scatterers of random phase. The *pdf* of pixel power is not, however. Let us call the power in a given pixel P, and the expected or mean power $\langle P \rangle$. Then the *pdf* of P is

[Levanon, 1988]:

$$pdf(P) = \frac{1}{\langle P \rangle} exp\left[\frac{-P}{\langle P \rangle}\right]. \tag{3.33}$$

The fluctuations of pixel power described by the above *pdf* are known as speckle. The word "speckle" is derived from the grainy images produced from coherent illumination of rough surfaces, originally in laser studies, but also found in SAR images [Dainty, 1975; Goodman, 1985; Madsen, 1986]. Speckle is often misleadingly labeled as noise, and there has been much effort to reduce speckle without a subsequent loss of image information. However, for the purposes of interferometry the speckle pattern is tremendously important. First, when co-registering two images in order to interfere them, speckle provides the needed contrast to align the SAR images precisely, especially in homogeneous regions without dominant scatterers such as the interior of the ice sheets. Secondly, the speckle pattern is a result of the coherent addition of many different scatterers over the size of the resolution cell, and is therefore at these wavelengths very sensitive to the angle of incidence. We will see in Chap. 4 that the correlation between (complex) speckle patterns at different θ can give important information about the sub-resolution structure of the scattering medium. Of course, for the purposes of estimating σ^0 from a single SAR image, speckle is a nuisance.

3.2.7 InSAR Power

Most of the power images that will be presented in this dissertation will be from InSAR observations. InSAR power images comprise two different SAR observations. For the images that we analyze here there is little if any perceptible difference between the two SAR power images. We calculate the power images associated with InSAR to be an average of the two, i.e.

$$P_{insar} = \sqrt{\langle s_1 s*_1 \rangle \cdot \langle s_2 s*_2 \rangle}. \tag{3.34}$$

Hereafter, when we refer to "power", it should be assumed that we imply P_{insar}, unless

stated otherwise.

Furthermore, as mentioned above, radar power images are often calibrated in terms of σ^0, for which geometric and radiometric distortions included in the radar equation (Eqn. 3.25) are accounted [Curlander and McDonough, 1991], as well as additive noise effects. We calibrate our power images using standards processed by C. Werner at Gamma Remote Sensing. A comparison between our calibrated power images of Greenland and those of the National Snow and Ice Data center show minimal differences.

As an example, Fig. 3.8 is a power image near Petermann glacier on the north coast of Greenland. The brightness scale corresponds to σ^0 values, in units of dB. If we consider the top of the image, and move left to right, we see that different forms of water have strikingly different backscattering efficiencies. The bright region to the left is the start of the percolation zone, where ice pipes and lenses dominate the scattering, as explained in Chap. 2. While not as bright as the brightest part of the Greenland percolation zone, which has σ^0 twice as high, this part of the image still shows a large amount of backscatter compared to the rest of the image. To the right of the percolation zone is the gray region that corresponds to the wet-snow zone, where there is an absence of large structures in the firn. The other zones, such as the ice or ablation zone, are not present, due to the relatively cold climate of this region of Greenland. The edge of the ice sheet is bright probably due to crevassing and fracturing from calving stresses. The very dark region in the right-center of the top is the Arctic ocean, which, due to the smooth surface and electrically lossy nature of sea water, scatters little energy back to the radar. Newly-calved icebergs can be seen in the ocean. The gray region to the far right is reformulated sea ice, which is electrically lossy to the radiowave due to the presence of salt, and thus scatters less energy back to the radar. Note that the ice regions, with the exception possibly of the sea ice, appear less focussed than the rocky region in the lower right. This is because scattering from the ice sheet is from a diffuse volume, whereas in the rocky region the scattering is confined to a surface [Jezek et al., 1993].

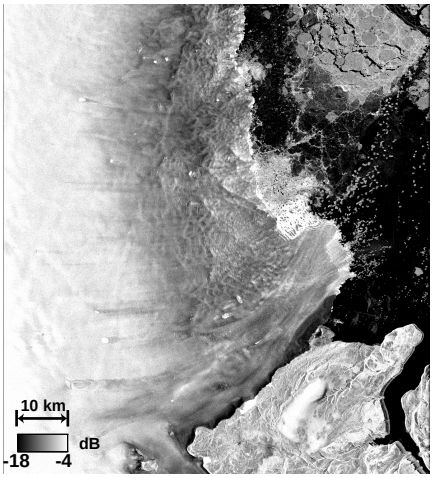

Figure 3.8: A power image from the north coast of Greenland, near Petermann Glacier. The scale corresponds to σ^0 values, in dB. Besides the rocky coast in the lower right, the image contains water only, in various forms. These various forms have strikingly different scattering properties, as explained in the text.

3.3 InSAR

3.3.1 Across-track interferometer

As stated in Sec. 3.2.2, the end-product of the SAR processor is a complex, focused image, with range/azimuth resolutions of a few to a few tens of meters. SAR *interferometry* consists of cross-correlating two such complex SAR images of the same terrain to derive more information about the terrain than is present in a single SAR image. For a second SAR image to provide additional information at least one imaging parameter must be different, such as flight path, time of observation, or wavelength. The most well-known use of interferometry in radar is the across-track interferometer, in which the across-track positions of the two observations are slightly different. This type of interferometer, which is described below, has its most important role in constructing DEM's of the Earth's topography, but it has other uses as well as we shall see in later chapters.

Two antennas, A_1 and A_2, are used in across-track interferometry, as seen in Fig. 3.9, where the flight direction is out of the page. In the *single-pass* mode, the antennas are joined physically and operated simultaneously, as in the TOPSAR and SRTM instruments.

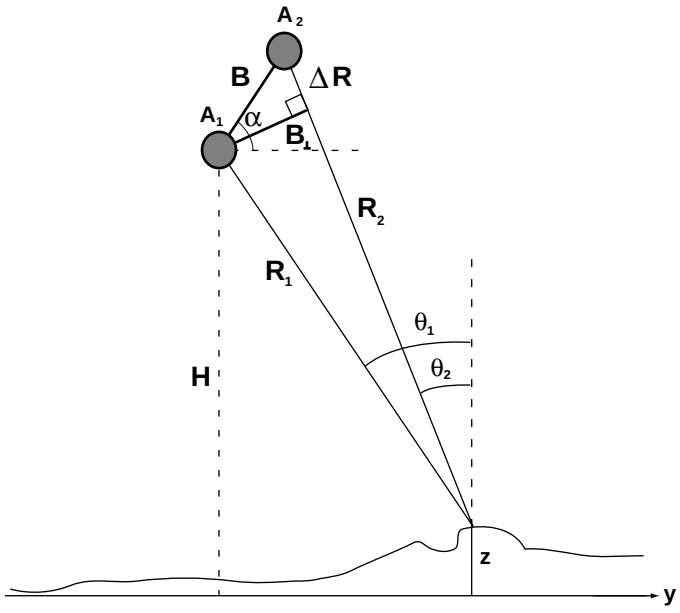

Figure 3.9: InSAR viewing geometry. Here the two antennas comprising the interferometer are A_1 and A_2. The variable z is the height of the surface above a local reference plane. The length of the perpendicular baseline $B_\perp$ indicates the sensitivity of the interferometer to the measurement of z.

Alternatively, the terrain can be imaged by a single SAR antenna at two different times such as with the ERS system. This is known as *repeat-pass* interferometry. Since ERS 1 and 2 were operated simultaneously for several years, they were used in conjunction in what is called *tandem* mode, where the interval between ERS 1 and ERS 2 passes was exactly one day. The effect of time on the interferometric measurement will be discussed in section 3.3.3.

The altitude of the first sensor above the ground is H and its radar look angle is θ_1, as shown in Fig. 3.9. The separation of the flight paths is called the baseline B, and its component perpendicular to the radar line-of-site is called the effective or perpendicular baseline $B_\perp$. The angle the baseline makes with the horizontal is α. For the time being let us constrain the scattering to the surface, but let the height of the surface z vary with the Earth's topography.

A complex SAR pixel whose center lies at range R and azimuth x will have the value

$$s(R,x) = |s(R,x)|\, e^{j\phi(R,x)}, \tag{3.35}$$

where ϕ is the resultant phase of the pixel. As stated before, the phase is random due to the number of sub-resolution scatterers. The phase due to travel between the radar and the ground, however, will depend only on the distance and the refractivity of the atmosphere at radar wavelengths, which we will assume for the time being is unity. Thus

$$\phi(R,x) = \frac{-4\pi}{\lambda} R + \phi_{scat}(R,x) \tag{3.36}$$

where the first term on the right side of Eqn. 3.36 is the phase due to round-trip travel between the sensor and the center of the resolution element, and ϕ_{scat} is the scattering phase.

The two SAR images are co-registered so that the same pixel in each image corresponds to the same spot on the ground. The interferogram is formed by cross-multiplying the two complex SAR images of the same terrain:.

$$i = s_1(R_1,x_1)s_2(R_2,x_2)^* = |s_1(R_1,x_1)|\,|s_2(R_2,x_2)| \exp(j\phi_{int}(R_1,R_2,x_1,x_2)), \tag{3.37}$$

where the interferometric phase is

$$\phi_{int}(R_1,R_2,x_1,x_2) = \frac{-4\pi}{\lambda}\Delta R + \phi_{scat,1}(R_1,x) - \phi_{scat,2}(R_2,x). \tag{3.38}$$

and the difference between the range values is ΔR, as shown in Fig. 3.9.

As stated above, ϕ_{scat} is deterministic, and therefore it is reasonable to suspect that $\phi_{scat,1}$ will be equal to $\phi_{scat,2}$. This is not quite true, as the difference in incidence angle between the two observations will result in a residual phase noise:

$$\phi_{int} = \frac{-4\pi}{\lambda}\Delta R + \phi_{noise}. \tag{3.39}$$

Of course there are several other possible sources of phase noise, and in fact there is much information in the relative magnitude of ϕ_{noise}. This is the main point of this thesis and it will be discussed in more detail in the following chapters. For the sake of conventional interferometry though, phase noise is a nuisance which results in a diminished accuracy in measurements of ΔR.

3.3.2 Topography measurement

Given the altitude H and the range R_1 the height z of every point on the Earth's surface can be reconstructed if the look angle θ_1 is known accurately, as depicted in Fig. 3.9. While θ_1 is known *a priori* to less than a degree, this is by no means precise enough to determine topography. It is only by combining the information contained in the second SAR image that we can determine the exact value of θ_1 and therefore z.

The InSAR imaging geometry resembles that used in stereo imaging, in that there are two parallel flight lines which view the terrain at two different viewing angles. Unlike conventional stereo techniques, where image contrast is required and where the parallax of chosen scatterers is used to determine height, InSAR uses the interferometric phase information of every pixel to measure the topography, as we see below.

From Fig. 3.9 and the law of cosines

$$\sin(\alpha - \theta) = \frac{(R_1 + \Delta R)^2 - R_1^2 - B^2}{2R_1 B}. \tag{3.40}$$

Also

$$z = H - R_1 \cos\theta. \tag{3.41}$$

The altitude H, the baseline B, and the tilt angle α can be derived from satellite the ephemeris. R_1 is known through time-of-flight analysis, and ΔR is derived from the

interferometric phase according to Eqn. 3.39. Therefore, using Eqns. 3.39-3.41 we can solve for the topographic height z:

$$z \approx -\frac{\phi_{topo}\,\lambda\,R_1}{4\pi\,B}\left[\frac{\cos\alpha}{\tan\theta_1}+\sin\alpha\right]^{-1}, \tag{3.42}$$

where we have renamed ϕ_{int} as ϕ_{topo}, the phase due to a varying topography.

Of course, ϕ_{topo} is still ambiguous to within integer multiples of 2π. In order to resolve this ambiguity, many different phase unwrapping algorithms have been developed, for example, see Goldstein et al. [1988]; Zebker and Lu [1998]; Chen and Zebker [2000]. The theory and implementation of phase unwrapping techniques is beyond the scope of this thesis, but stated simply, where ϕ_{noise} is comparatively small and the rate of change of ϕ_{int} from one pixel to the next is also small, then the phase can be unwrapped into a continuous function.

With a few manipulations, Eqn. 3.42 can be rearranged in terms of $B_\perp$ and z:

$$\phi_{topo} \approx -\frac{4\pi B_\perp z}{\lambda R \sin\theta}, \tag{3.43}$$

where we have substituted a generic R for R_1.

Because the interferometric phase can be measured to within a few tenths of a radian, topographic errors of only few meters in height are possible, though inaccurate knowledge of the baseline geometry as well as ϕ_{noise} limits the precision of the measurement [Zebker et al., 1994b; Hanssen, 2000]. Nevertheless, detailed topographic information can be obtained about the Earth, and in particular the vast and remote ice sheets, from an InSAR satellite system orbiting several hundred kilometers above the surface.

3.3.3 Motion measurement

In repeat-pass mode, the temporal as well as the spatial separation of the two observations becomes important. Similar to the spatial baseline B, the time between observations is called the *temporal baseline*, T. A non-zero T may mean that the terrain has been altered between observations. For the present we will only discuss coherent motion, in which the

scatterers in a pixel move by the same amount. Of course on the scale of one scene ($\approx$100 km in the ERS case) there may be differences in the magnitude and direction of the motion, but within a resolution element the velocity vectors must be equal for the motion to be considered coherent. This requirement implies a large-scale ($<$ 1 km) crustal deformation such as from earthquakes, subsidence or glacial flow.

If the motion is coherent, then a phase term associated with the change in range adds directly into the interferometric phase (Eqn. 3.38):

$$\phi_{int} = \phi_{topo} + \phi_{motion} + \phi_{noise}. \tag{3.44}$$

Here

$$\phi_{motion} = \frac{-4\pi}{\lambda}\delta R, \tag{3.45}$$

where δR is the amount of line-of-sight motion towards the radar that occurs between observations. ϕ_{motion} is baseline-independent. Moreover, since ϕ_{motion} can be mapped directly into displacement without the R scaling that is present in ϕ_{topo}, the InSAR system is therefore highly sensitive to deformations, with measurements in the sub-cm scale routine in the ERS case.

Because of its synoptic and regular observations afforded by the SAR satellites, InSAR has become an invaluable tool for mapping the motion of glaciers and ice sheets. However, since ϕ_{int} will contain both topography and motion information, we must constrain one in order to solve for the other. This is often done by *double differencing* two interferograms, in which the phase of a second interferogram is subtracted from the first. The double differencing method uses the assumption that the ice moves at a constant rate, i.e. ϕ_{motion} is the same in interferograms having the same temporal baseline. Normally the two interferograms will have the same temporal baselines but different spatial baselines, such that after differencing only a residual $\phi_{topo,diff}$ term will remain, where

Table 3.1: Orbit information for Ryder data

Interferogram	ERS Orbit/Frame No.	Acquisition Dates	$B_\perp$,m	T, days
a	3520/1935-3477/1935	18-15 MAR 1992	52	-3
b	3520/1935-3463/1935	18-21 MAR 1992	164	3

$$\phi_{topo,diff} = \phi_{topo,1} - \phi_{topo,2} B_{\perp,1}. \tag{3.46}$$

The differenced topography term has an associated baseline of

$$B_{\perp,diff} = B_{\perp,1} - B_{\perp,2}. \tag{3.47}$$

Using $B_{\perp,diff}$ with $\phi_{topo,diff}$ we can solve for the topography as described in Sec. 3.3.2. The topography information is then used to synthesize ϕ_{topo} for one of the interferograms, which is then subtracted from Eqn. 3.44, leaving only the motion term.

As an example of this technique, we consider ERS data acquired over one of the channels of the Ryder glacier in Northern Greenland. The data were acquired in March 1992. In Fig. 3.10 (a) we show the location of the scene. In the power image of this scene (b) we see that, in the upper left, the exposed rock has formed a comparatively narrow channel between which ice is situated. The direction to the coast is towards the upper left. We also can see a high contrast in the backscatter between the ice that is in the upper left and that which is closer to the interior of the ice sheet in the lower right. This contrast is due to the various structural differences within the firn associated with altitude, as discussed in Chap. 2.

In Fig. 3.11 (a) and (b) we show the phases of two different interferograms, resulting from both the gradual slope of the terrain towards the coast and the motion of the ice stream in the same direction. The orbital information is listed in Table 3.1.

In (a) $B_\perp = 45$ m and in (b) $B_\perp = 164$ m, therefore by Eqn. 3.43 there are over three times more topographic fringes in (b) than in (a). This is apparent in the number of fringes

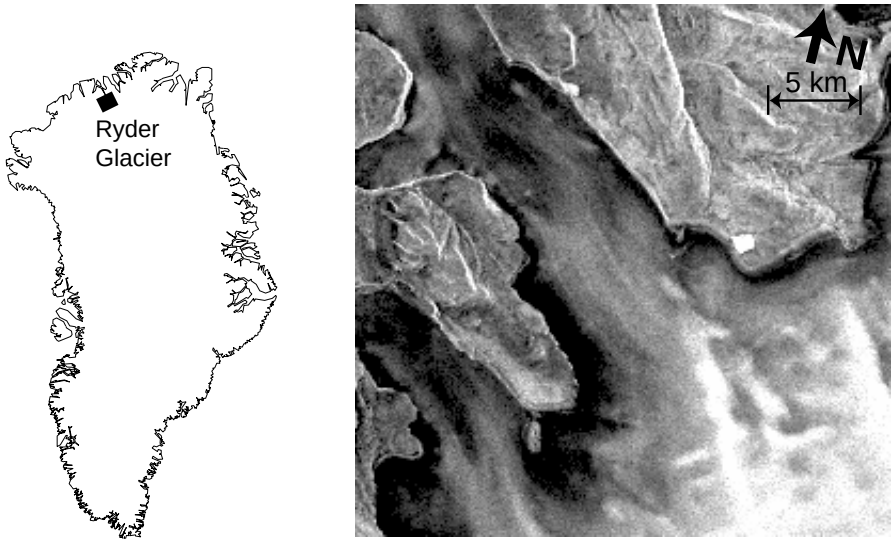

(a) Ryder Glacier location (b) Power image of Ryder Glacier channel.

Figure 3.10: Location (a) and power image (b) of a channel of the Ryder glacier. The divisions between rock and ice/snow is easily seen. The ice zone is the very dark regions near the rock. The wet snow zone is the intermediate bright region. The bright region to the lower left is the start of the percolation zone.

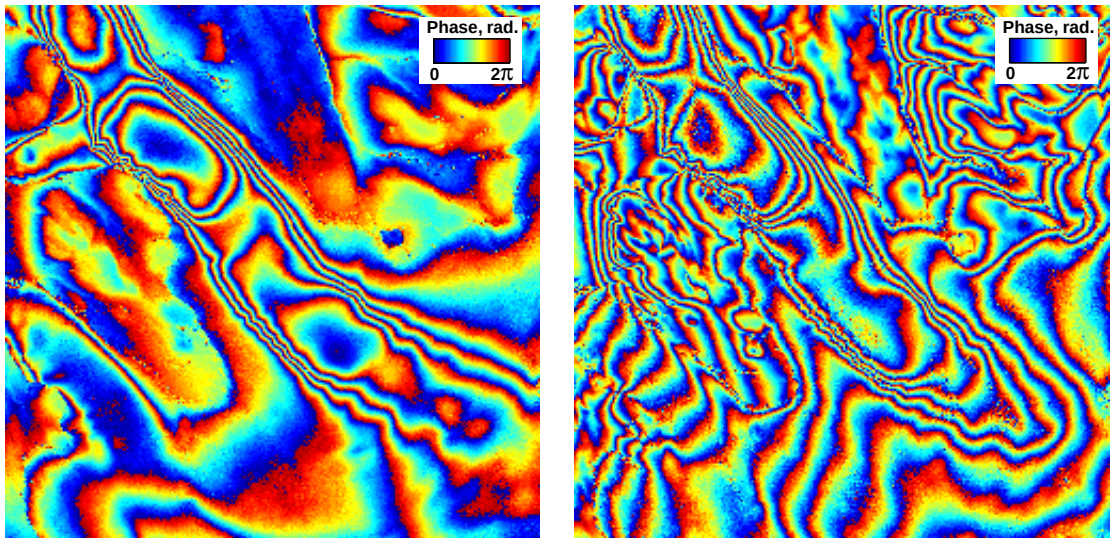

(a) (b)

Figure 3.11: Ryder Glacier Interferograms. The interferogram in (a) has a $B_\perp$ of 45 m, while the $B_\perp$ of interferogram (b) is 162 m; therefore there are nearly 4 times the number of topographic fringes in (b) than in (a). However, since both interferograms have a three-day temporal baseline, they have the same number of motion-induced fringes.

in the rocky area in the upper right of the image. The time between observations was 3 days for both interferograms, thus each interferogram has the same number of motion-induced fringes. However, for (a) $T = -3$ days while in (b) $T = 3$ days, therefore the sequence of the colors in the motion fringes is reversed. This is evident in the dense fringes near the *shear margin* of the ice stream. Here, because the narrow channel, the magnitude of the velocity vector changes rapidly over short spatial scales.

Using the double differencing technique described above we solve for both the topography and the motion towards or away from the radar, shown in Fig. 3.12 (a) and (b), respectively. The slope of the ice sheet towards the coast is evident in (a), which is steep in comparison to the rest of Greenland. (See Fig. 1.1.) In the motion image (b) we see the draining of the ice sheet through the channel towards the coast. Several "bullseyes" are also seen. These are due to the sliding of the ice stream over the undulations in the bedrock, producing a vertical component in the motion of the surface [Kwok and Fahnestock, 1996]. Because of the steep look angle of ERS (23 degrees) the radar is more sensitive to vertical

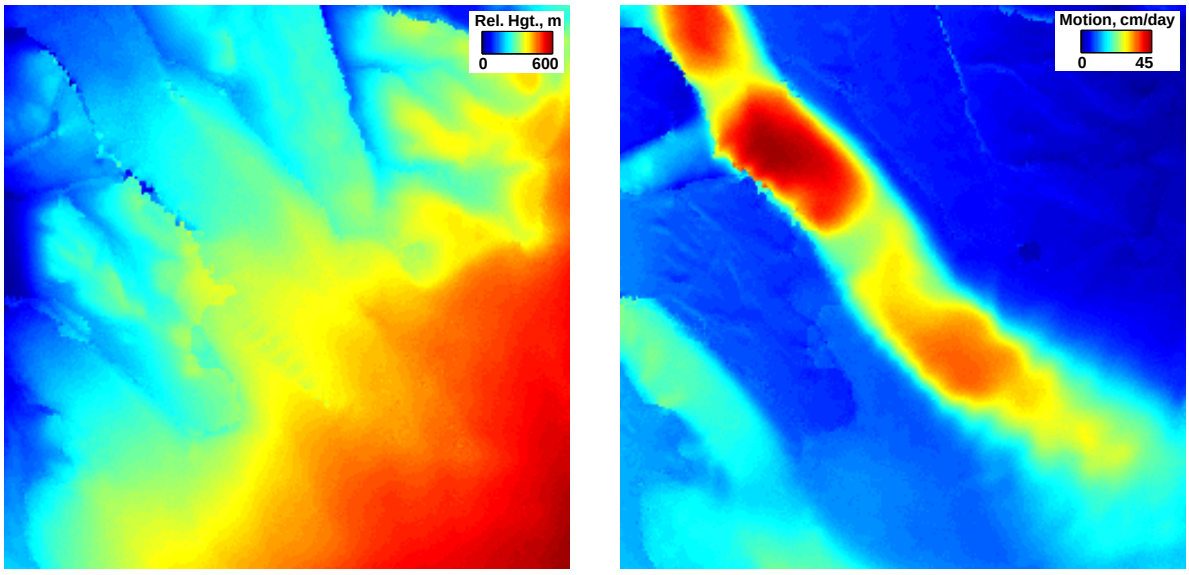

(a) (b)

Figure 3.12: Fringes corresponding to topography (a) and motion (b) for the Ryder interferograms shown in Fig. 3.11, as derived from the double-differencing technique explained in the text.

than horizontal motions, by a factor of 2.4.

Since the radar measures motion only in the line-of-site direction, motion perpendicular to $\vec{R}$ will go undetected. Further information about the ice velocity vector can be gained by combining velocity maps derived from ascending and descending orbits [Joughin et al., 1998]. For the ERS case in central Greenland, there is a $\sim 45°$ angle between the northward- and southward-going orbit tracks. To derive a 3-D representation of the ice motion from ascending and descending orbits a further assumption must be made: that the velocity vector is parallel to the surface. This usually is a valid assumption for ice sheets, though some amount of motion perpendicular to the surface does occur within glaciers [Paterson, 1994].

If the scatterers within a resolution element do not move *en masse* but instead move in a random manner, then this will comprise incoherent motion. Incoherent motion, part of a larger set of temporal decorrelation effects, will tend to increase ϕ_{noise}. This will be discussed in greater detail in Chap. 4.

3.3.4 Atmospheric signal

It was assumed earlier that the refractivity of the atmosphere was the same in both observations. In repeat-pass mode this is not necessarily the case, as changes in water vapor content and ionospheric electron fluctuations can cause a difference in the speed of propagation from one day to the next. This difference would amount to an additional interferometric phase term ϕ_{atmos}, and would appear in the interferogram as fringes. In conventional InSAR atmospheric fringes are considered a nuisance, as ϕ_{atmos} might be interpreted as topography or deformation, and the uncertainty about the atmospheric contribution can severely limit the accuracy of topography/deformation maps [Goldstein, 1995; Zebker et al., 1997]. The simplest recourse taken to reduce the effect of the atmosphere on InSAR measurements is to average several to many interferograms together; since the atmospheric water content changes from day-to-day, then ϕ_{atmos} should be reduced.

On the other hand, there has been at least one study, Hanssen et al. [1999], which has focused not on eliminating the atmospheric signal in interferograms but matching it to the meteorological data at the time of observation. The area studied was Northern Holland, which consists of flat, stable terrain. Thus in the interferograms both ϕ_{topo} and ϕ_{motion} would be negligible, leaving only the ϕ_{atmos} term. Hanssen et al. [1999] found that the InSAR phase measurement in some cases provides a more spatially detailed means to map atmospheric water content then other remote sensing techniques. Fig. 3.13 is a figure from this study. On the left is the residual atmospheric phase, in units of delay, where the bodies of water have been masked out, and on the right is a weather radar image taken at the same time as the first SAR image. It is clear that InSAR and the weather radar see the same storm, but that the InSAR technique has a finer resolution. This figure shows that InSAR may be a useful tool in making more precise weather forecasts.

In the case of the ice sheets, because of the frigid temperatures and high elevations, the atmosphere can hold only a small amount of water vapor. There has been no instance known to the authors of an atmospheric signal in ice sheet interferograms.

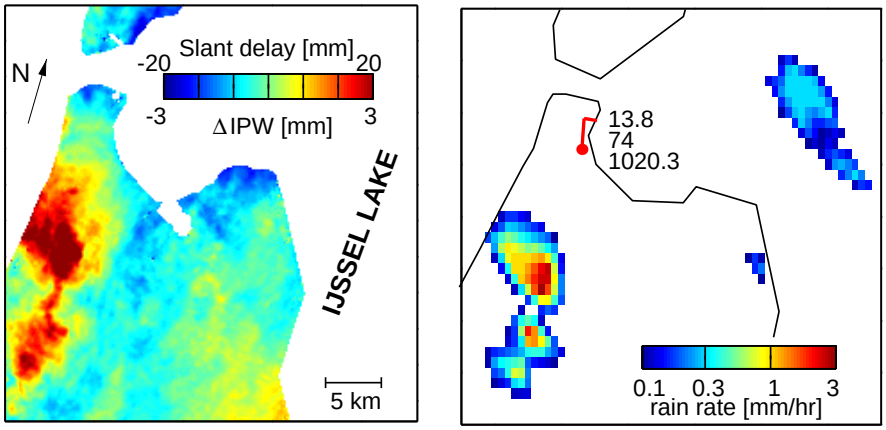

(a) (b)

Figure 3.13: The SAR interferogram (a)(29 and 30 August, 1995, 21:41 UTC) shows slant delay variation, mapped to zenith integrated precipitable water differences. The average of the undisturbed area is set to zero, yielding relative precipitable water estimates. In (b) the weather radar rain rate (29 August, 1995, 21:45 UTC) is shown. The surface wind velocity is 4.1 m/s, from 350 degrees, indicated by the wind barb. Temperature (°C), the percentage of relative humidity, and pressure (hPa) are plotted beside the station. From Hanssen et al. [1999].

3.3.5 Total phase

Therefore, the total interferometric phase, including effects due to topography, coherent motion of the terrain, a varying atmosphere between the observations, and noise, is:

$$\phi_{int} = \phi_{topo} + \phi_{motion} + \phi_{atmos} + \phi_{noise}. \tag{3.48}$$

To make an accurate geophysical measurement from one of the first three terms in the right hand side of Eqn. 3.48, the term must first be isolated by combining other interferograms or by using *a priori* information. While the chance of a strong ϕ_{atmos} signal is low for the Greenland ice sheet, the other two terms, ϕ_{topo} and ϕ_{motion} will always be present. As stated earlier, ϕ_{noise} is a hindrance to these measurements. We will show in the next chapters, however, that there is useful information contained within this noise term, as quantified by the interferometric correlation.

Chapter 4

Correlation

4.1 Introduction

In the previous chapters we showed how power and interferometric phase observations from satellite-borne radar sensors lead to a greater understanding of the facies, topography, and dynamics of the Greenland ice sheet. In particular, InSAR data provide useful information for constraining both melt extent and the amount of ice discharge, which comprise basic and needed information for mass balance estimates. What is lacking, though, is a means to probe the sub-surface of the ice sheet from space. While the power images from C-band radars are sensitive to structures beneath the surface, there is no means to calculate to what depth this sensitivity extends. This is important, because, as we will discuss in Chap. 6, knowledge of the vertical extent of scattering allows us to better estimate the local accumulation rate, which is the most sought-after mass balance term. The InSAR power and phase observables are limited in this regard, as they give no information about the depth of the locus of the return echo.

There is another InSAR observable besides power and phase, however – the interferometric correlation. The correlation, or coherence, of an interferogram is a statistical comparison between pixels at the same location in the two SAR images. As we mentioned in Sec. 3.3.1, there will be a stochastic component to the phase, ϕ_{noise}, along with the coherent terms, ϕ_{topo}, ϕ_{motion}, and ϕ_{atmos}. The correlation value is a measure of the relative contribution of ϕ_{noise} to the total interferometric phase. In this sense, the correlation has been used historically to assess the accuracy of the coherent phase estimates.

In this chapter we demonstrate that correlation, through a simple model, gives important information about the Greenland ice sheet, namely the radiowave penetration depth of the

upper firn. The penetration depth is indicative of the power loss due to scattering as well as the absorptive losses of the icy medium. In Chap. 5 we use the results from the model to extract penetration depths of the ice sheet, from the coastal areas into the interior, and in Chap. 6 we extend the modeling to relate the correlation, coupled with the power observations, to accumulation rates.

Before investigating the geophysical aspects of correlation, we begin with a discussion of the practical issues in measuring correlation. Then we develop a model that relates spatial correlation, i.e. the correlation that is dependent on the physical separation of the two interferometric observations, to penetration depth. The final section is devoted to other possible factors that may influence correlation.

4.2 Correlation Measurement

Mathematically, the correlation, ρ, is defined as the ratio of the magnitude of the interferogram to the mean power of the two signals, s_1 and s_2, which are assumed to be (wide-sense) stationary processes [Born and Wolf, 1985]:

$$\rho = \frac{|\langle s_1 s_2^* \rangle|}{\sqrt{\langle s_1 s_1^* \rangle \langle s_2 s_2^* \rangle}} \tag{4.1}$$

where ρ is the correlation. Elsewhere [Born and Wolf, 1985; Goodman, 1985] the correlation is defined as the complex equivalent of Eqn. 4.1, i.e. without the $|\cdot|$ in the numerator. We instead define the correlation as magnitude only and leave phase information to the interferogram. Therefore ρ ranges from 0 to 1, with 0 indicating complete decorrelation, and 1 complete correlation.

By the $\langle\cdot\rangle$ in Eqn. 4.1 we denote expectation values. In practice, the correlation is evaluated by approximating the expectation as a spatial averaging of neighboring pixels (or taking looks, discussed in Sec. 3.2.4):

$$\tilde{\rho} = \frac{|\sum_{i=1}^{N} s_1(i) s_2^*(i)|}{\sqrt{\sum_{i=1}^{N} s_1(i) s_1^*(i) \ \sum_{i=1}^{N} s_2(i) s_2^*(i)}}, \tag{4.2}$$

where $\tilde{\rho}$ is the measured correlation and $N = n_{az} \times n_{ra}$ is the total number of pixels averaged in azimuth and range. The processes involved in Eqns. 4.1-4.2 are assumed to be ergodic in mean, and therefore the sample means in Eqn. 4.2 will provide asymptotically unbiased estimates to the statistical means in Eqn. 4.1 [Touzi et al., 1999].

The estimator in Eqn. 4.2 will give biased results, however, due to the $|\cdot|$ operation. If we are to derive the most accurate quantitative information from the correlation we must correct for this inherent bias. The expected value of the biased correlation, $\langle\tilde{\rho}\rangle$, as a function of the true correlation ρ and the number of *independent* or *effective* looks L has often been evaluated using Monte Carlo simulations [Goldstein et al., 1993; Zebker et al., 1994b; Guarnieri and Prati, 1997; Hoen and Zebker, 2000, 2001]. Touzi et al. [1996] found a closed-form expression:

$$\langle\tilde{\rho}\rangle = \frac{\Gamma(L)\Gamma(1+1/2)}{\Gamma(L+1/2)} \cdot F_{2,3}(3/2, L, L; L+1/2, 1; \rho^2) \cdot (1-\rho^2)^L \tag{4.3}$$

where $F_{q,p}$ is the generalized hypergeometric function as defined by Abramowitz and Stegun [1972]. In Fig. 4.1 we plot Eqn. 4.3 for several values of L. For $L = 1$ the correlation will be unity, as would be expected from Eqn. 4.2. For an increasing number of looks or for an increasing correlation the bias is asymptotically reduced towards the true value.

L is not known *a priori*. What is known is the number of actual looks, N. Because the resolution cell size is greater than the pixel size (see Sec. 3.2.3), adjacent pixels are not completely independent of each other and the actual number of looks N will be greater than the number of independent looks L. A tapered windowing function, which increases resolution cell size, will only make the disparity between L and N grow. Joughin and Winebrenner [1994] showed, that if the number of independent looks, L, can be estimated, it can be used in place of the actual number of looks in the expression for the multilook phase *pdf*. Hence if L is known, then together with the expected measured correlation, $\langle\tilde{\rho}\rangle$, and Eqn. 4.3, we can find the true correlation. Since Eqn. 4.3 is difficult in practice to invert analytically, we use the curves in Fig. 4.1 to calculate the inversion numerically.

There are several methods to estimate the effective number of looks of an InSAR image. The method that we use involves the standard deviation of the measured correlation, $std(\tilde{\rho})$,

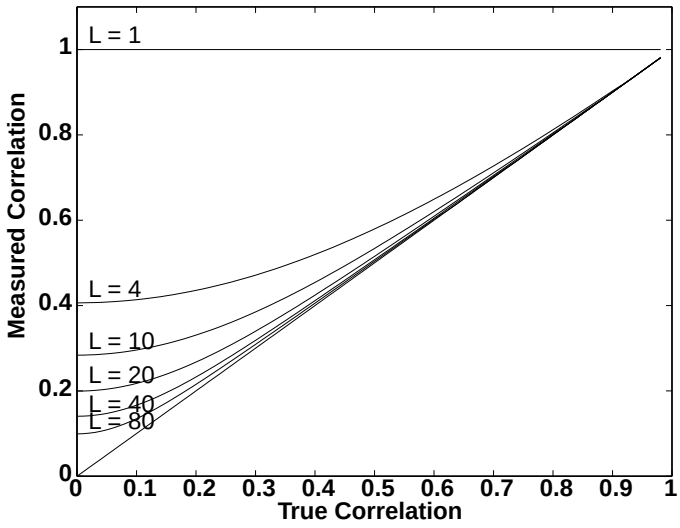

Figure 4.1: Bias in the correlation estimate due to spatial averaging, for different number of looks. The bias inherent in Eqn. 4.2 decreases for an increasing number of averages and/or increasing correlation value. The curves were computed using Eqn. 4.3.

and the mean measured correlation, $\langle\tilde{\rho}\rangle$. Touzi et al. [1999] found that, for high correlation values, the standard deviation of the correlation is approximated by the Cramer-Rao bound:

$$std(\tilde{\rho}) = \frac{1 - \langle\tilde{\rho}\rangle^2}{\sqrt{2\,L}}. \tag{4.4}$$

Thus the standard deviation and mean of the measured correlation, for high correlation values, can be used with Eqn. 4.4 to determine L. L is assumed not to vary with correlation; it is the same for low correlation values.

In Fig. 4.2 we plot a family of curves from Eqn. 4.4, with ERS correlation data from the dry snow zone of Greenland. The ERS data were processed using a Kaiser spectral weighting function to reduce sidelobes. The curve for L=43 optimizes the match with the data. The actual number of looks was in this case 80, therefore the effective number of looks was about half of the total. Joughin and Winebrenner [1994] found a similar $N : L$ ratio for ERS data processed with a cosine-on-a-pedestal spectral weighting function. Using this value of L with the curves generated by Eqn. 4.3 we can remove the small bias associated

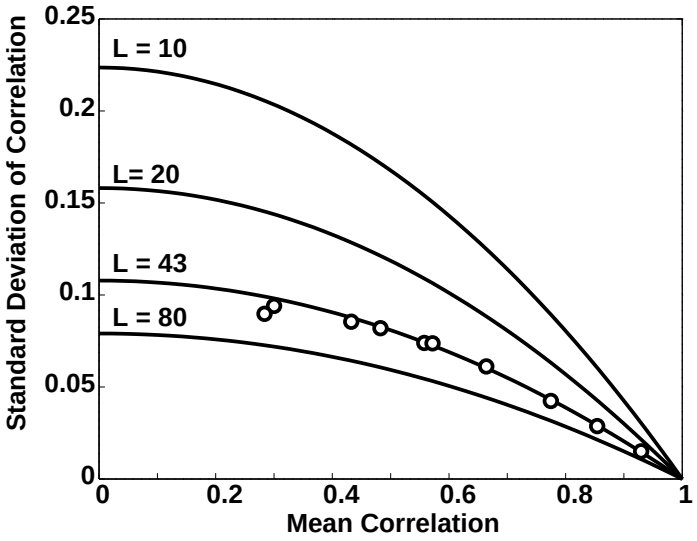

Figure 4.2: Standard deviation of the correlation vs. mean correlation, for different number of independent looks. Plotted also are ERS data from the dry snow zone of Greenland, as circles. The ERS data, with 80 actual number of looks, is found to have approximately 43 effective number of looks.

with all of the data used in this thesis, since they were processed identically. No bias found was greater than 0.03.

Another way to estimate L is to compare the resolution size to the pixel size for the averaging window used in Eqn. 4.2. For example, the ERS nominal azimuth resolution is 6 meters and the ground range resolution is 25 meters whereas the pixel sizes are 4 meters and 20 meters, respectively [Zebker et al., 1994a]. Therefore an image that was averaged $20\times4=80$ times will have approximately

$$L = 20 \times 4 \times 80/(25 \times 6) \approx 43 \tag{4.5}$$

independent looks, or the same as was found by the method discussed previously.

Even though the bias for these data is negligible compared to the other unknowns that will be discussed in Chap. 5, for reference we list the step-by-step method we use for calculating the true correlation from the processed ERS interferometric data:

(1) Compute the correlation image from the processed interferometric data as per Eqn. 4.2 with $N = n_{az} \times n_{ra} = 20 \times 4 = 80$.

(2) Select a 30×30 pixel region of interest within the image. With the number of looks in (1) this region corresponds to a 2.4 x 2.4 km square. The size of the region is chosen to allow for an accurate calculation of sample mean, while remaining small enough to avoid texture in the images, in order that the assumption in Eqn. 4.1 be valid.

(3) Compute the sample mean of the region. I.e.,

$$\langle \tilde{\rho} \rangle = \frac{1}{K} \sum_{i=1}^{K} \tilde{\rho}, \tag{4.6}$$

where K(=900) is the number of samples in the region of interest.

(4) Convert $\langle \tilde{\rho} \rangle$ to ρ using the curve for $L = 43$ (or other L values if different processing steps than above are taken) from Eqn. 4.3.

As an example, two correlation images of the same scene in the dry snow zone of Greenland are shown in Fig. 4.3, with a region of interest denoted by the black box. The distributions from this region are shown in Fig. 4.4, with sampled means of 0.56 (a) and 0.45 (b). The unbiased values are 0.55 and 0.43, respectively . The reason why the correlation images in Fig. 4.3 seem to have the exact same structure but with a slightly different overall correlation will be discussed in Chap. 5.

In Fig. 4.3 we have used a color scale to denote the correlation value in order to show the differences between (a) and (b). For the rest of the correlation images in this dissertation we will either use this color scale or, in cases where a simple contrast between high/low correlation is desired, a gray scale.

4.3 Spatial Decorrelation

4.3.1 Overview

Because of the physical separation of the two antennas forming the interferometer, the incidence angle for one image will be slightly different than that of the other, as shown in Fig. 4.5. The decorrelation that results from this separation we call spatial decorrelation;

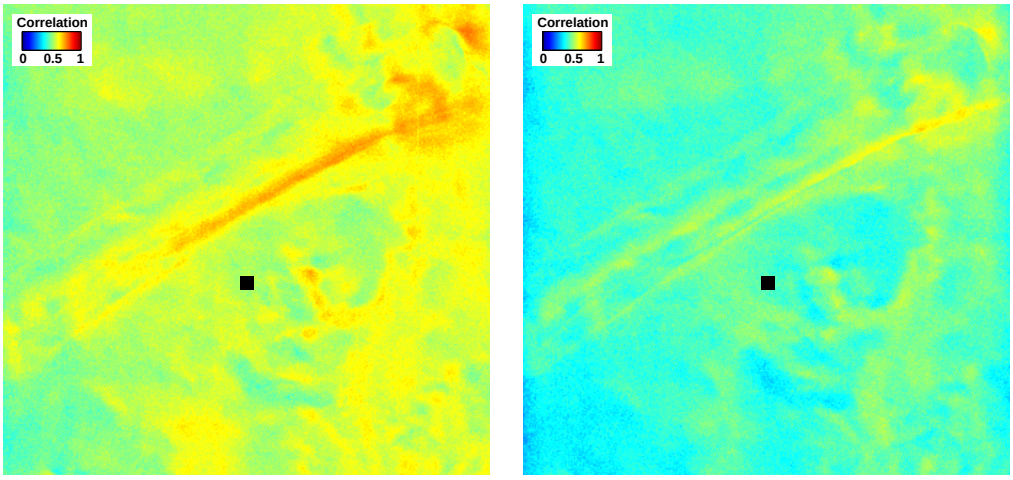

(a) (b)

Figure 4.3: Correlation images from the dry snow zone of Greenland. Both correlation images exhibit the same features, but with a difference in overall correlation. The reason for this difference will be discussed in detail in Sec. 4.3. The black square in the center of the images demarks the area whose correlation values are shown in the histograms of Fig. 4.4 (a) and (b).

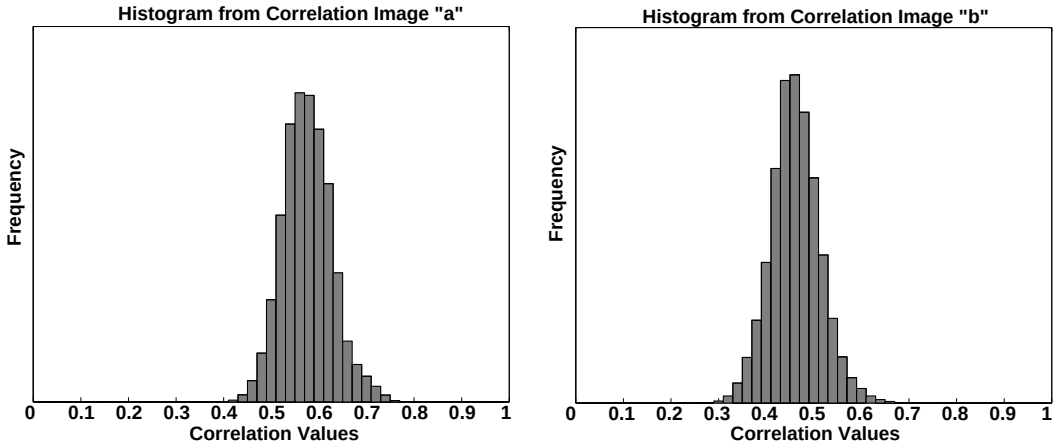

(a) (b)

Figure 4.4: Correlation distributions from the area of study (the black square) in Fig. 4.3 (a) and (b), respectively. The mean (unbiased) correlation is 0.56 in (a) and 0.45 in (b).

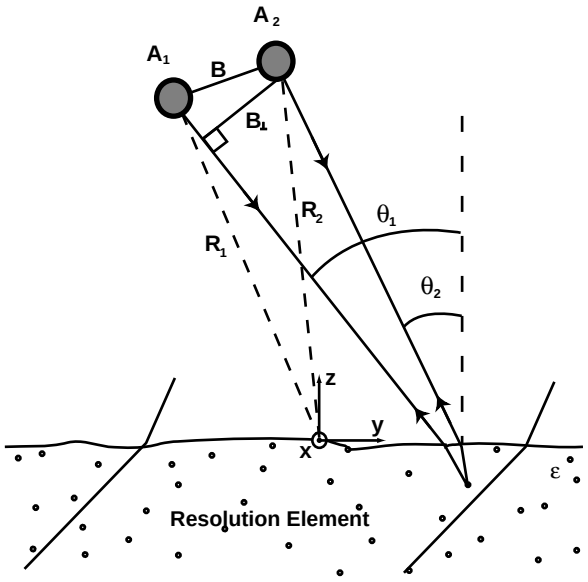

Figure 4.5: Interferometric viewing geometry for volume scatter, where A_1 and A_2 are the two radar antennas and ϵ is the effective dielectric constant of the firn. Representative borders of the resolution element are refracted by the ice/snow medium.

it is also known as baseline decorrelation or geometric decorrelation.

We present now a derivation of the spatial correlation coefficient, where for generality we permit the scatterers to be spread vertically as well as horizontally within a refractive half-space. As was the case with the derivation of expected return power, we will examine two cases: surface scatter and volume scatter from a lossy medium.

4.3.2 Formation of Spatial Correlation Model

Consider the viewing geometry shown in Fig. 4.5, where A_1 and A_2 are the two antennas of the interferometer, and the angle of incidence for each is θ_1 and θ_2, respectively. As was the case in the derivation of SAR power in Chap. 3, we assume a scattering medium with reflectivity function $f(x, y, z)$ and effective permittivity ϵ. The distance from the center of the resolution element to the radars is R_1 and R_2. For simplicity we will assume that the origin of the (x, y, z) coordinate system is at the center of the resolution element on the surface, as shown in Fig. 4.5.

As was mentioned in Chap. 3, the sub-resolution propagation term D_r determines both the phase due to travel of the echo from an individual scatterer, and the weighting that the impulse response applies to the amplitude of the echo. In the geometry here,

$$D_{r1} = y \sin\theta_1 - z\sqrt{\epsilon}\cos\theta_{r1}, \tag{4.7}$$

with a change of index from 1 to 2 for D_{r2}.

Then the value, or "signal" measured by antenna A_1 for the representative resolution element can be expressed by the sum of complex echoes from point scatterers in the far-field of the antenna:

$$s_1 = \iiint f(x,y,z) e^{-j\frac{4\pi}{\lambda}(R_1 + D_{r1})} \cdot W_x(x) W_r(x,y) dx dy dz, \tag{4.8}$$

where θ_r denotes the refracted angle within the medium and $W_r(y,z)$ is $W_r(y,z)_{firn}$ defined by Eqn. 3.16.

Likewise the corresponding signal measured by antenna A_2 is

$$s_2 = \iiint f(x,y,z) e^{-j\frac{4\pi}{\lambda}(R_2 + D_{r2})} \cdot W_x(x) W_r(y,z) dx dy dz. \tag{4.9}$$

The interference, or cross-correlation, of the two signals is

$$s_1 s_2^* = e^{-j\frac{4\pi}{\lambda}\Delta R} \iiint \iiint f(x,y,z) f^*(x',y',z') \cdot e^{-j\beta(y,z,y',z')} \cdot W_x(x) W_x^*(x') W_r(y,z) W_r^*(y',z') dx dy dz dx' dy' dz',$$

where

$$\beta(y,z,y',z') = \frac{4\pi}{\lambda}(y\sin\theta_1 - y'\sin\theta_2 - \sqrt{\epsilon}\,(z\cos\theta_{r1} - z'\cos\theta_{r2})). \tag{4.10}$$

Here the phase factor in front of the integrals is the interferometric phase as was discussed in Chap. 3, which will drop out when we consider the magnitude of the correlation.

We assume the volume consists of uniformly distributed and uncorrelated scattering centers as was assumed in the derivation of SAR power in Chap. 3:

$$\langle f(x,y,z) f^*(x',y',z') \rangle = \sigma_v(x,y,z)\, \delta(x-x', y-y', z-z'). \tag{4.11}$$

Then

$$\langle s_1 s_2^* \rangle = e^{-j\frac{4\pi}{\lambda}\Delta R} \iiint \sigma_v(x,y,z)\, e^{-j\,\gamma(y,z)} \cdot |W_x(x)|^2 |W_r(y,z)|^2 dx dy dz$$

where

$$\gamma(y,z) = \frac{4\pi}{\lambda}(y\, \cos\theta\, \delta\theta + \sqrt{\epsilon}\, z\, \sin\theta_r\, \delta\theta_r). \tag{4.12}$$

Here θ is the average of θ_1 and θ_2, and θ_r is the average of θ_{r1} and θ_{r2}. Also, $\delta\theta = \theta_1 - \theta_2$, and $\delta\theta_r = \theta_{r1} - \theta_{r2}$, which are both small angles, such that

$$\sin\theta_1 - \sin\theta_2 \approx \cos\theta\, \delta\theta, \tag{4.13}$$

and

$$\cos\theta_{r1} - \cos\theta_{r2} \approx -\sin\theta_r\, \delta\theta_r\,. \tag{4.14}$$

Furthermore, we assume here that the volumetric radar cross section of the scatterers within each resolution element varies only as a function of depth, i.e.

$$\sigma_v(x,y,z) = \sigma_v(z), \tag{4.15}$$

which is reasonable for the highly stratified geometry of the Greenland firn. Then the cross-correlation becomes

$$\langle s_1 s_2^* \rangle = e^{-j\frac{4\pi}{\lambda}\Delta R} \int |W_x(x)|^2 dx \cdot \int \sigma_v(z) e^{-j2\pi k_z z} \cdot \int |W_r(y,z)|^2 e^{-j2\pi k_y y} dy dz. \tag{4.16}$$

where

$$k_y = \frac{2}{\lambda} \cos\theta \, \delta\theta, \tag{4.17}$$

and

$$k_z = \frac{2}{\lambda} \sqrt{\epsilon} \, \sin\theta_r \, \delta\theta_r. \tag{4.18}$$

The x variable in Eqn. 4.16 can be integrated directly. Since

$$W_r(y,z) = W_r(\frac{y \, \sin\theta - \sqrt{\epsilon}\, z \, \cos\theta_r}{R_r}), \tag{4.19}$$

then we can make use of the shift property of Fourier transforms to separate the remaining two integrals:

$$\langle s_1 s_2^* \rangle = e^{-j\frac{4\pi}{\lambda}\Delta R} \cdot R_x \cdot \int |W_r(y)|^2 e^{-j2\pi k_y y} dy \int \sigma_v(z) e^{-j2\pi k_z z} e^{\frac{-2\pi j \sqrt{\epsilon} \cos\theta_r k_y z}{sin\theta}} dz \tag{4.20}$$

From the derivative of Snell's law,

$$\cos\theta\,\delta\theta = \sqrt{\epsilon}\,\cos\theta_r\,\delta\theta_r. \tag{4.21}$$

We can then combine the terms in the exponent of the z integral to yield

$$\langle s_1 s_2^* \rangle = e^{j\frac{-4\pi}{\lambda}\Delta R} \cdot R_x \cdot \int |W_r(y)|^2 e^{-j2\pi k_y y} dy \int \sigma_v(z) e^{-j2\pi k_{zz} z} dz, \tag{4.22}$$

where

$$k_{zz} = \frac{2\sqrt{\epsilon}\,\delta\theta_r}{\lambda\,\sin\theta_r}. \tag{4.23}$$

To calculate the correlation coefficient, $\rho_{spatial}$, we divide the cross-correlation product in Eqn. 4.22 by the average power in the two channels, as expressed in Eqn. 4.1, and take the absolute value, thereby canceling the interferometric phase factor and the azimuthal resolution:

$$\rho_{spatial} = \left| \frac{\int |W_r(y)|^2 e^{-j2\pi k_y y} dy}{\int |W_r(y)|^2 dy} \right| \cdot \left| \frac{\int \sigma_v(z) e^{-j2\pi k_{zz} z} dz}{\int \sigma_v(z) dz} \right|. \tag{4.24}$$

We examine below two scenarios for radar scattering. First, the scattering is constrained to the surface only, and, second, the entire volume contributes to the return, but with an associated loss due to radiowave travel within the medium.

4.3.3 Surface Scatter

If the scattering is localized to the surface, such as for microwave scattering from rock, wet soil, or sea water for example, then

$$\sigma_v(x, y, z) = \sigma^0(x, y)\delta(z). \tag{4.25}$$

The second factor in Eqn. 4.24 then is 1, leaving

$$\rho_{spatial} = \rho_{surface} = \left| \frac{\int |W_r(y)|^2 e^{-j2\pi k_y y} dy}{\int |W_r(y)|^2 dy} \right|. \tag{4.26}$$

Assuming a square spectral window, which has a sinc-like impulse response (as described in Sec. 3.2.3), and substituting $\frac{B_\perp}{R_0}$ for $\delta\theta$, the Fourier transform relationship in Eqn. 4.26 results in a scaled triangle function:

$$\rho_{surface} = \begin{cases} 1 - \frac{2|\delta\theta|B_\perp|R_r}{R_0 \lambda |\tan\theta|} & |B_\perp| < B_{\perp,crit}\,, \\ 0 & |B_\perp| \geq B_{\perp,crit}\,, \end{cases} \tag{4.27}$$

where the critical baseline, the point where correlation drops to zero, is

$$B_{\perp,crit} = \frac{R_0 \lambda |\tan\theta|}{2R_r}. \tag{4.28}$$

For ERS, $B_{\perp,crit}$ is about 1100 m for flat terrain.

In Fig. 4.6 we plot the surface correlation as a function of baseline for both the square and Kaiser window filters for ERS geometries. Notice that windowing has the effect of raising the correlation for smaller $B_\perp$ at the expense of the larger baseline correlation. This makes sense if we consider the generalized interferometric geometry, where a smaller baselines are sensitive to larger spectral wavelengths. By applying a tapered window to the return echo we are giving more weight to the larger wavelengths, and therefore the smaller baseline correlation should be increased.

Another way to visualize surface decorrelation is to consider the difference in incidence angle as a shift in the received ground reflectivity spectrum for each observation [Gatelli et al., 1994]. A schematic of this effect is shown in Fig. 4.7, where a single spatial frequency is mapped back into the radar direction at different frequencies in the two observations. Thus there is an apparent "shift" between the two received ground spectra. This shift causes the amount of spectral overlap to decrease, as depicted in Fig. 4.8. The amount

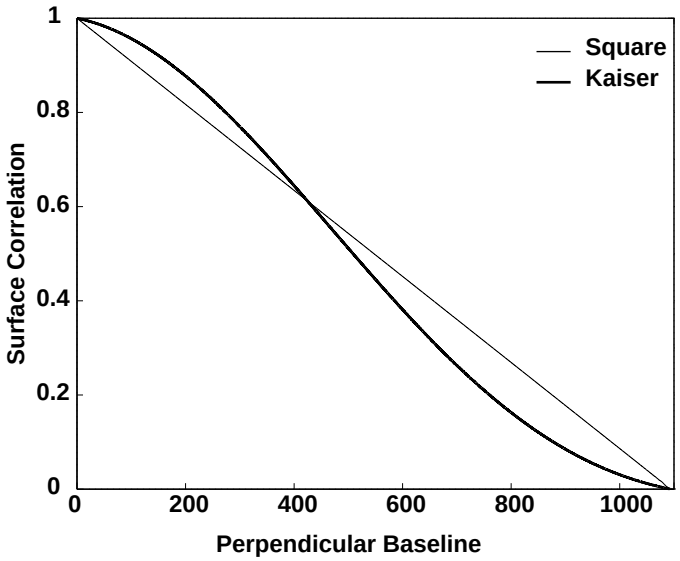

Figure 4.6: Square and Kaiser window functions effect on surface correlation, assuming ERS parameters for rough, flat terrain. Due to the tapered shape of the Kaiser spectral window, smaller baseline correlation is increased.

of spectral overlap, compared to the total, indicates the degree of correlation. Note that the actual set of frequencies used by the SAR is identical in each case; it is set by the specifications of the instrument and of the spectral windowing in the processor. It is the *projected* ground frequencies that are, however, shifted from each other. Because this shift is often visualized as a shift in spatial frequencies, it has been called the "k-shift" [Gatelli et al., 1994].

Gatelli et al. [1994] first proposed a filtering method to increase correlation, in which the $\rho_{surface}$ term is maximized by truncating the parts of the spectra that do not overlap. If the only source of decorrelation is from $\rho_{surface}$, then these overlapping parts will be perfectly correlated. As $\rho_{surface}$ is a function of slope angle (due to the θ in Eqn. 4.27), the filter should ideally take the topography information, either from a DEM or ϕ_{topo}, as input. This method is called "slope filtering". Since the power in the signal has been decreased by the truncation there will be a drop in SNR. Beyond the critical baseline no correlation can be achieved by any method.

Decorrelation from surface scatter is defined by the system parameters in Eqn. 4.26, and,

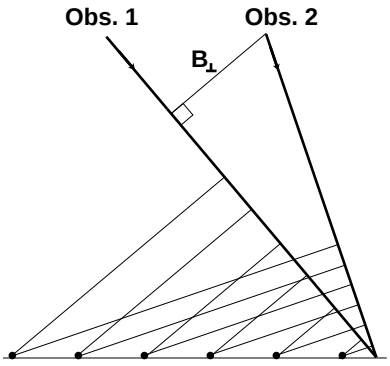

Figure 4.7: K-shift of ground reflectivity spectrum. A single ground spatial frequency maps back into the range direction differently for the two observations, due to the difference in incidence angle.

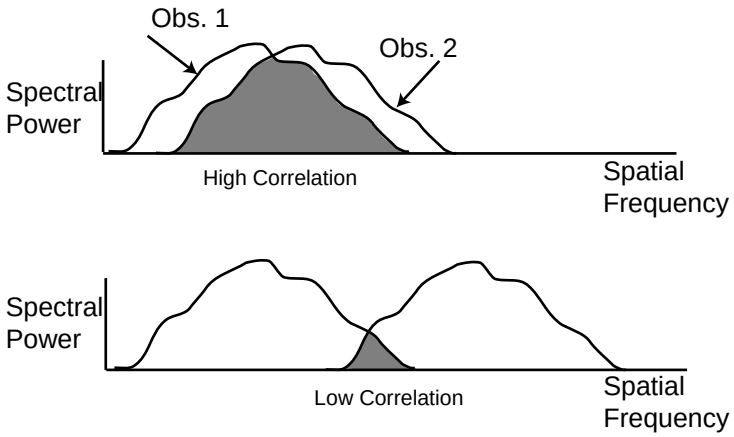

Figure 4.8: Spatial decorrelation from shifted spectra. Due to the difference in incidence angle, the ground reflectivity spectra will be shifted from one another. The extent of overlap indicates the degree of correlation. The critical baseline is reached when the spectra do not overlap, resulting in a correlation of zero.

in general, determines the interferometrically useful baselines for studies of terrain lacking in vertical structure. Other than the local slope, however, there is no information contained in $\rho_{surface}$ about the terrain. This is similar to the coherent optical imaging case, where the decorrelation of the complex laser speckle patterns with viewing angle is dependent on only the size of the laser "spot" and is not dependent on the details of the scattering surface [Goodman, 1999].

4.3.4 Volume Scatter

For the spatial decorrelation coefficient for the volume scatter case we retain the entire right side of Eqn. 4.24. Therefore the expression for spatial correlation for scattering over a half-space volume includes the surface scattering coefficient, but has a volume scatter coefficient as well:

$$\rho_{spatial} = \rho_{surface} \cdot \rho_{volume}. \tag{4.29}$$

where $\rho_{surface}$ is defined in Eqn. 4.26 and

$$\rho_{volume} = \left| \frac{\int \sigma_v(z) e^{-j2\pi k_{zz} z} dz}{\int \sigma_v(z) dz} \right|. \tag{4.30}$$

The subscript "surface" is somewhat misleading, for even if there is no actual surface scattering this factor will still exist, but we have chosen this nomenclature because it is of identical form to the surface scatter-only case described above, as well as published surface scatter solutions [Zebker and Villasenor, 1992; Gatelli et al., 1994]. It is perhaps more accurate to consider $\rho_{surface}$ as the decorrelating factor associated with the y variable, and ρ_{volume} as associated with z.

The integrals that comprise each of the factors in Eqn. 4.24 are similar in form, as they both express Fourier transform relationships, and each depends on the spatial localization of the scattering that contributes to the return echo. The extent of the scatterers contributing to the return echo in the y direction is contained in $\rho_{surface}$; the greater the width of $W_r(y)$,

the faster the correlation will drop-off with increasing $B_\perp$. Similarly, ρ_{volume} is a measure of the extent of the scatterers contributing to the return echo in the z direction; the greater the vertical extent of the scattering, the faster the correlation will fall with increasing $B_\perp$. The relationship between the size of the terrain "aperture" and the rate of spatial decorrelation is identical with the results of the classical two-slit experiment, where the shape of the interference envelope is determined by the Fourier transform of the aperture function.

What is *not* similar about $\rho_{surface}$ and ρ_{volume} is that now, with ρ_{volume}, we gain information about the scattering medium, namely, the vertical dispersion of scatterers comprising the return echo.

As was the case in Sec. 3.2.5, we assume here that the scattering medium is homogeneously lossy, and extends in depth as far as the radar can "see":

$$\sigma_v(z) = \sigma_v^0 \, e^{\frac{2z\kappa_e}{\cos\theta_r}}. \tag{4.31}$$

Here σ_v^0 is the average cross section per unit volume, which we assume to be constant. Propagation losses are contained within the exponential, where the extinction coefficient κ_e is equivalent to $1/d$, where d is the penetration depth at which the one-way power falls to $1/e$. In reality d is a penetration *length*, since by the factor $\cos\theta_r$ in the exponent we are accounting for the off-vertical travel of the radiowave within the medium. For ERS observations of the Greenland ice sheet, $\theta \approx 23°$, $\epsilon \approx 1.9$ (discussed in Chap. 5), resulting in θ_r of 16° and $\cos\theta_r$ of 0.96. Therefore the penetration "depth" that is measured can be considered nearly vertical.

We note here that there are other ways of defining the penetration depth, in particular the one-way $1/e$ point for the field amplitude ($= 2\,d$), or the two-way $1/e$ point for power ($= d\,/2$). The present definition of d was chosen for consistency with the existing literature of *in situ* radar measurements of glacial firn [Matzler, 1987; Rott et al., 1993].

Substituting Eqn. 4.31 into the ρ_{volume} factor in Eqn. 4.30, and using the scaling property of Fourier transforms, we have

$$\rho_{volume} = \left| \frac{1}{1 + jU} \right|. \tag{4.32}$$

where

$$U = -\frac{2\pi \sqrt{\epsilon}\, d\, \delta\theta_r}{\lambda \tan\theta_r}, \tag{4.33}$$

or

$$U = -\frac{2\pi \sqrt{\epsilon}\, d\, B_\perp}{R_0\, \lambda \tan\theta}. \tag{4.34}$$

Notice in Eqn. 4.33 that the refractive medium alters both the wavelength and the angle, but that the angular effects cancel out, as evidenced in Eqn. 4.34. Eqn. 4.32 can be rearranged to be

$$\rho_{volume} = \left| e^{j\phi_z} \frac{1}{\sqrt{1 + U^2}} \right|, \tag{4.35}$$

where

$$\phi_z = \tan^{-1} U. \tag{4.36}$$

In Chap. 5 we will show how the phase factor ϕ_z can also give information about the wave penetration, but for the correlation-based argument here it is eliminated by the $|\cdot|$ procedure. Computing the magnitude of Eqn. 4.32,

$$\rho_{volume} = \frac{1}{\sqrt{1 + (\frac{2\pi \sqrt{\epsilon}\, d\, B_\perp}{R_0\, \lambda\, tan\theta})^2}}. \tag{4.37}$$

In Fig. 4.9 we plot two different curves from Eqn. 4.37 along with the results from a Monte-Carlo simulation, in which Eqn. 4.1 was calculated from realizations over a uniform

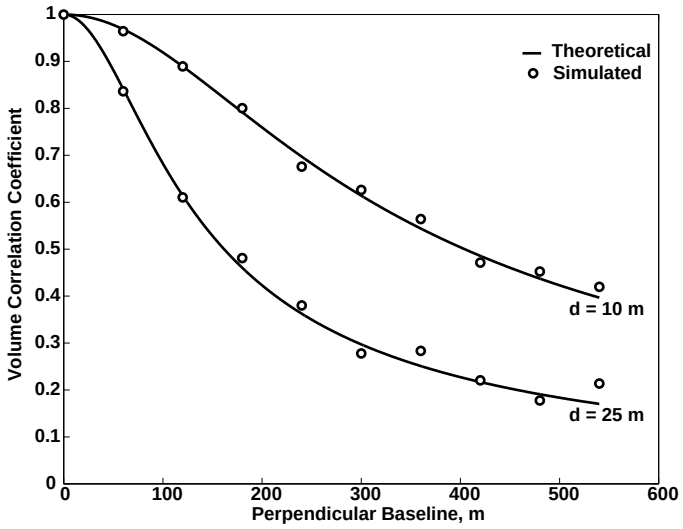

Figure 4.9: Theoretical and simulated volume decorrelation for penetration depths of 10 and 25 meters.

volume distribution of point scatterers for 10 different baselines.

Thus by inverting Eqn. 4.37 the unbiased correlation ρ can be related to the depth of penetration d of the radiowave into the medium. In terms of the Greenland ice sheet, knowledge of the penetration depth will determine whether the radar echo is dominated by return from the surface or near-surface, or whether a significant contribution comes from buried scatterers in the firn. Moreover, climatic differences could alter the penetration depth from one region to the next, a variation to which the correlation would be sensitive.

4.4 Other Decorrelation Sources

Unfortunately, since the radar, the ground, the intervening medium, and the processing steps used to create the interferogram comprise a compound observing system, there are several potential sources of decorrelation other than spatial decorrelation. The total correlation is reducible, i.e. it consists of a series product of the individual decorrelation factors [Zebker and Villasenor, 1992]:

$$\rho = \rho_1 \cdot \rho_2 \cdot \rho_3 \cdot ... \tag{4.38}$$

In this section we detail the sources of decorrelation that correspond to the factors above, other than the $\rho_{surfcace}$ and ρ_{volume} factors derived in the previous section.

4.4.1 Data and Processing Errors

There are several different errors which can occur between the reception of the radar signal and the production of an interferometric correlation image, such as errors introduced into the raw data at the downlink station, or misregistration of the two SAR images when forming the interferogram, for example. We group these effects into one coefficient, $\rho_{process}$.

The raw data error mentioned above is particularly troubling for InSAR studies of Greenland, because all of the ERS data over Greenland are downlinked to the same station in Kiruna, Sweden. Unfortunately a systematic and replicating error is occasionally observed in the raw SAR data from this station, resulting in nearly horizontal (i.e. in the range direction) "streaks" of low correlation. At first these streaks were thought to be caused by katabatic winds [Jezek et al., 1994]. Later it was found that in fact the streaks were due to missing data, which were surprisingly not aligned exactly with the rows of the raw data [Joughin, 1994]. Moreover, no such streaks have been found in any ERS or RADARSAT data over Antarctica, where strong katabatic winds are also present. To date no cause for this data error has been found. In Fig. 4.10 we show a correlation image containing many such streaks. The darkened lines correspond to the abovementioned streaks. In some Greenland InSAR data the number of streaks is so large as to render the data unusable.

Co-registration of the two SAR images is another important source of decorrelation. If the registration is done improperly the phases of the resolution elements will not align and a loss of coherence will ensue, as is the case with the raw data error mentioned above. In Fig. 4.11 we plot ρ_{misreg}, a sub-factor of $\rho_{process}$, as a function of pixel offset in azimuth (a) and range (b). The shape of the curve in the two images is a function of the impulse response of the system, as images of coarser resolutions will suffer smaller decorrelating effects from misalignment. Therefore the curves for the Kaiser window fall off slower than

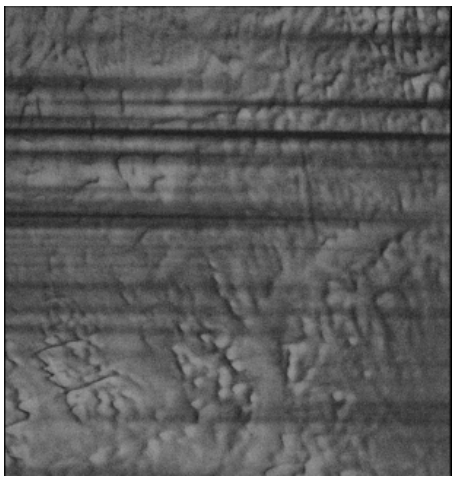

Figure 4.10: Correlation streaks in ERS data of Northern Greenland. The streaks are believed to be caused by raw data errors introduced at the downlink station in Kiruna, Sweden [Joughin, 1994].

those for the square window. ρ_{misreg} is also a function of the perpendicular baseline, with large baselines falling off slower than small baselines [Joughin, 1995].

Local misregistration also can occur in images where one area of the terrain has moved a significant amount between observations. The fast moving tongues of glaciers and ice streams can move several meters per day, for example. Thus inter-observational times of a few weeks will cause pixels in these fast moving areas to be misaligned. If phase information is required for these regions, then adaptive co-registering techniques may be required [Joughin, 2000].

Another effect that decreases $\rho_{process}$ is the spatial averaging over high phase gradients, such as those caused by steep slopes or shearing motion of the terrain. Atmospheric or ionospheric variations, such as clouds, exist on spatial scales that are greater than a few tens of pixels and in general have diffuse edges, and therefore can not cause the steep gradients in phase that can lead to this apparent decorrelation. The decorrelation that results from averaging over fringes is due, in essence, to the fact that the magnitude of the sum of vectors is smaller than the sum of their magnitudes, as depicted in Fig. 4.12. While the previous statement is, of course, always true, in most cases the variation in phase over the averaging window is due to ϕ_{noise}, not a coherent signal. For a large phase gradient,

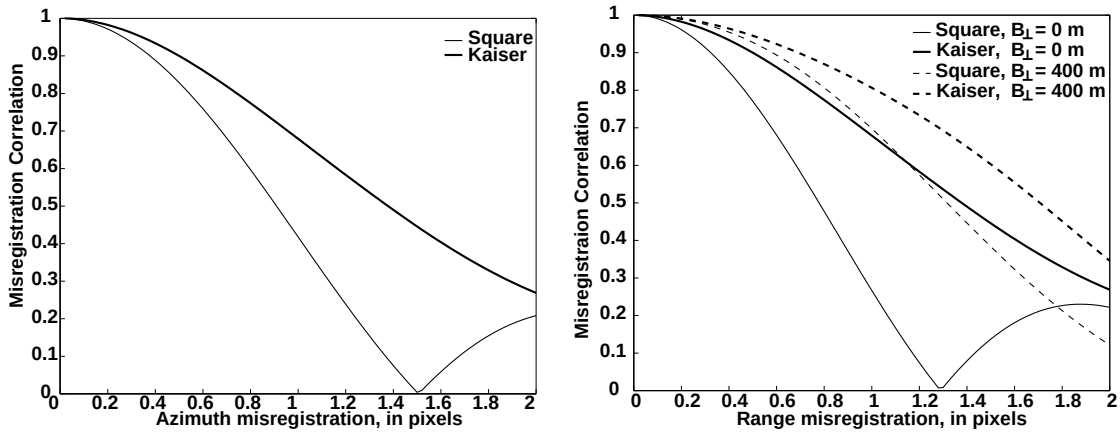

Figure 4.11: Correlation loss from misregistration, in azimuth (a) and range (b), for square and Kaiser spectral windows. In range, an increasing perpendicular baseline tends to lessen the amount of misregistration decorrelation.

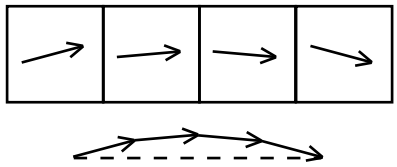

Figure 4.12: Decorrelation from phase gradients. The resultant is smaller than the sum of magnitudes, implying decorrelation from Eqn 4.2.

the true value of correlation, ρ, could still be a high value, but because of the spatial extent of the averaging window $\tilde{\rho}$ will decrease.

For instance, if f_r is the assumed constant number of cycles of phase per 1-look pixel and n_{ra} is the number of pixels averaged in one direction, which in this case is range, then the measured correlation is

$$\tilde{\rho} = \frac{\left|\sum_{i=1}^{n_{ra}} e^{j2\pi f_r i}\right|}{n_{ra}}, \tag{4.39}$$

where we have assumed that (1) the power in each channel is constant over the averaging

window, (2) there is no phase gradient in azimuth, and (3) the true correlation is unity. Using properties of geometric series,

$$\tilde{\rho} = \left| \frac{sinc(f_r n_{ra})}{sinc(f_r)} \right|. \tag{4.40}$$

Thus in this scenario the disparity between $\tilde{\rho}$ and ρ *increases* for an increasing number of looks. For this reason, if desired geophysical information is contained within areas of high phase gradients, the number of looks is often reduced.

A typical value of n_{ra} is 4. Complete decorrelation will therefore occur at an f_r of 0.25 cycles/pixel. For ERS deformation studies, this implies that over one pixel, or 20 m, the change in displacement towards the radar must be less than 0.7 cm, in order to avoid complete decorrelation. For topography, assuming $B_\perp \cong 100$ m, a slope of 10% towards the radar results in $\tilde{\rho} = 0$. For the ice sheets the scenario involving topography is unlikely, as the slopes in the interior are always less than 1°. The possibility of averaging over a high fringe rate due to motion-effects is possible, however, near the *shear margins* of glaciers or ice streams. For example, see Fig. 3.11, where the fringes near the margins of the ice stream are broken, due to spatial averaging over the rapidly changing phase.

In sum, the decorrelation sources due to processing or data errors can lead to complete decorrelation, but are not typical. For correlation studies such as this dissertation, high fringe rate or high velocity areas can be avoided, as can the areas in the image with correlation streaks. We found no systematic loss of correlation due to misalignment of the images or other processing errors. Therefore, we assume that $\rho_{process} \cong 1$.

4.4.2 Thermal Decorrelation

When the received signal approaches the thermal noise level, then there will be decorrelation, due to fact that the noises in the two signals will not correlate. If we assume white circular Gaussian (thermal) noise in the receiver, then its associated correlation factor, $\rho_{thermal}$, is related to the SNR according to [Zebker and Villasenor, 1992]:

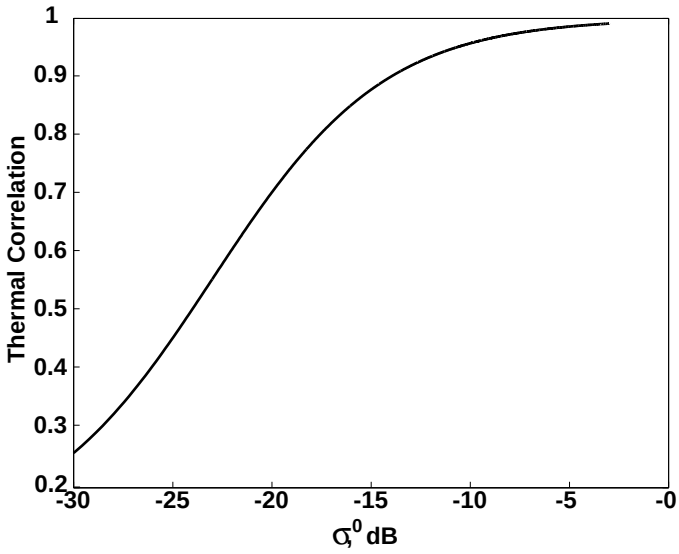

Figure 4.13: Thermal decorrelation, plotted as a function (Eqn. 4.41) of the normalized radar cross section of the terrain, σ^0. The noise floor is determined by the temperature in the receiver [Levanon, 1988]. For ERS σ^0_{noise} = -25 dB.

$$\rho_{thermal} = \frac{1}{1 + \frac{1}{SNR}}. \tag{4.41}$$

For the ERS system the thermal noise equivalent, σ^0_{noise}, which represents the apparent σ^0 when there is no signal other than the additive noise in the receiving system, is -25 dB. In Fig. 4.13 we plot $\rho_{thermal}$ as a function of σ^0, assuming that a region in the middle of the antenna beam is illuminated. Unless σ^0 is below -15 dB there is negligible thermal decorrelation, and for most of the correlation images analyzed here the SNR is sufficiently high that $\rho_{thermal} \cong 1$. An example that does exhibit thermal decorrelation will be given in Sec. 4.4.3.

4.4.3 Temporal Decorrelation

The correlation coefficient associated with incoherent variations in the scattering medium between observations, such as through random changes in the position and sizes of the

Crawford Point Location

Figure 4.14: Location of Crawford Point Station, in East Greenland. The station lies within the percolation zone.

scatterers or temporal fluctuations in the electrical properties of the scattering medium, is called $\rho_{temporal}$. For example, areas of dense vegetation often suffer increased amounts of temporal decorrelation due to the movement of the leaves and branches in the wind, or their growth over time. Zebker and Villasenor [1992] reported that the fall-off of temporal decorrelation with time was linear for various types of forest in Oregon. Another result from this study was that, for the case of ERS, an RMS motion of 2-3 cm of the scatterers in the resolution cell results in complete decorrelation.

Examples of mechanisms that may decrease $\rho_{temporal}$ for the Greenland ice sheet are the movement of snow/ice particles on the surface due to wind, the settling of the upper firn into year layers, or fracturing due to shearing motions of ice streams. Liquid water plays an important role as well, as a terrain with a variable liquid water content will have different radiowave scattering properties from one observation to the next [Zebker et al., 1994a].

As an example that combines both thermal and temporal decorrelation effects, we consider ERS tandem data of a summer melt event at Crawford Point, the location of which is shown in Fig. 4.14. In Fig. 4.15 we show data from two InSAR observations in the summer of 1995. Figs. 4.15 (a), (c) and (e) refer to June 21-22 observations, and (b), (d), (f) refer to July 26-27 observations. Power images are shown in (a) and (b), correlation images in (c) and (d), and temperature readings at the Crawford Point weather station (location marked with a black cross in the images) in (e) and (f). The times of ERS observation, which were locally at 11:43 a.m, correspond to the dashed lines. The temperature data is courtesy of

J. Box, University of Colorado.

In Fig. 4.15 we can see the onset of summer melt in the percolation zone, and its effect on power and correlation. In (a), the firn, due to the scattering efficiency of ice pipes and lenses (as discussed in Chap. 2), appears bright, with the exception of a dark region at the bottom right corner of the image. This dark area is closer to the coast, at low elevation, and thus more susceptible to melting. Liquid water is much absorptive to microwave radiation than is the dry firn. Thus, where there is melting on the surface or within the snowpack, little energy is scattered back to the radar. The correlation image (c) matches the power image, where we see high correlation in most of the interior, but low correlation near the coast. The temperature readings in (e) show that, at the location of the weather station, the temperature was below freezing during the two observations. On the other hand, in (f) we can see that the temperature at the weather station was above freezing for the two observations. This is corroborated by the power image (b), which is almost completely dark, due to the suspected presence of liquid water on the surface. The correlation image (d) matches that of the power image, with the bottom right half of the image completely decorrelated.

How much of the decorrelation that we see in Fig. 4.15 is due to thermal noise effects and how much is due to temporal decorrelation? By comparing (a) with (c) and (b) with (d)there seems to be a correspondence between power and correlation, which suggests that $\rho_{thermal}$ is a significant source of decorrelation. The coefficient $\rho_{thermal}$ is easily calculated from the power and the noise floor of the system by Eqn. 4.41. In Fig. 4.16 we show the calculated thermal correlation image. As is evident, some but not all of the loss of correlation in Fig. 4.15 (d) can be attributed to thermal decorrelation. It is reasonable to expect that the rest of the decorrelation is due to temporal effects, since the scattering surface was changed in between observations by melting. Spatial decorrelation, which is a not decorrelating factor in this case, since the perpendicular baseline was 3 meters.

Monitoring the correlation for dramatic SNR and temporal effects is thus a means to map the extent of summer melt on the ice sheet. However, for the rest of this dissertation we use data either from the dry snow zone or, if at lower elevations, from the winter months, to avoid melt possibilities. For ice sheet terrain not experiencing melt, the temporal effects are much more gradual, as we will see in Chap. 5.

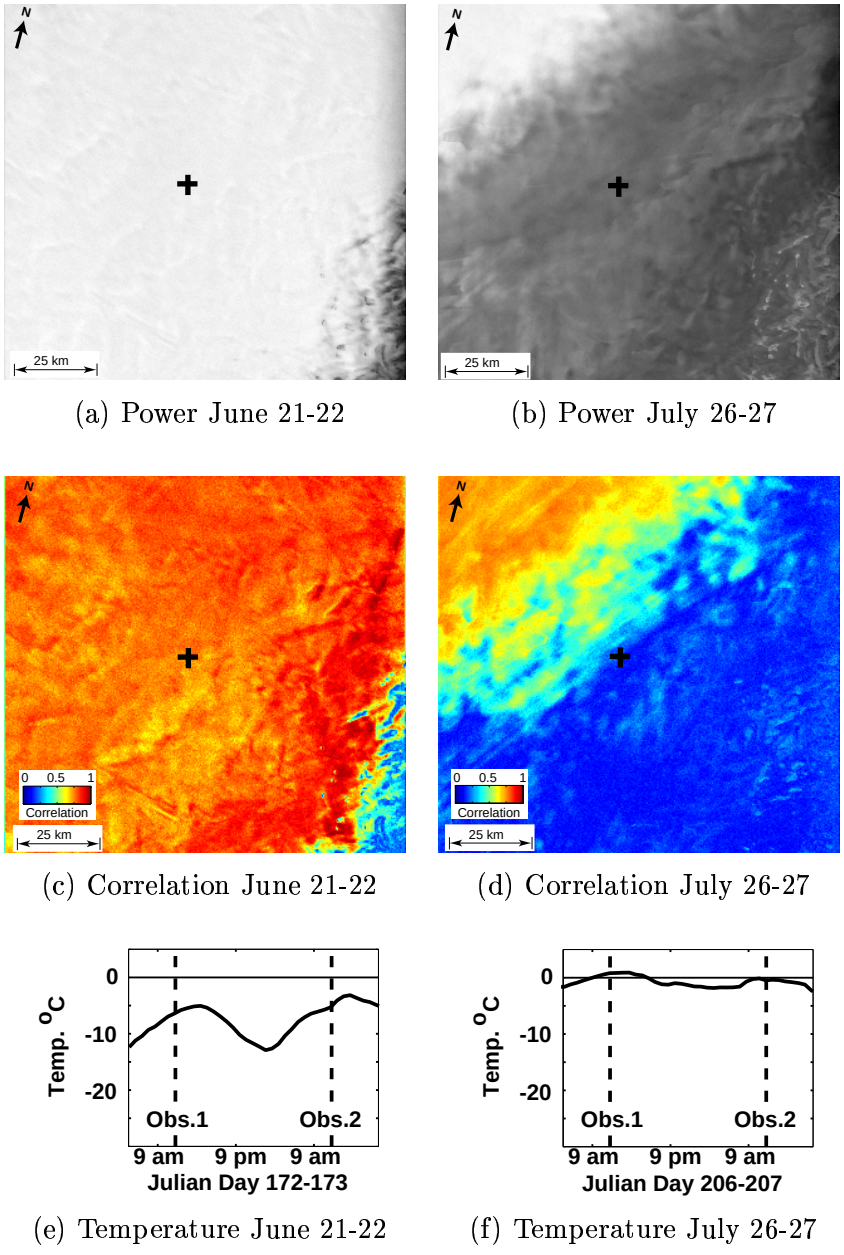

(a) Power June 21-22 (b) Power July 26-27

(c) Correlation June 21-22 (d) Correlation July 26-27

(e) Temperature June 21-22 (f) Temperature July 26-27

Figure 4.15: ERS power ((a) and (b)) and correlation images ((c) and (d)) over Crawford point, with temperature data from the Crawford Point weather station (denoted by the black cross) around the time of observation ((e) and (f)), for June 21-22 and July 26-27 1995, respectively. By comparing the data sets (a), (c) and (e) with (b), (d) and (f) we can see the dramatic effect melting has on the power and correlation images.

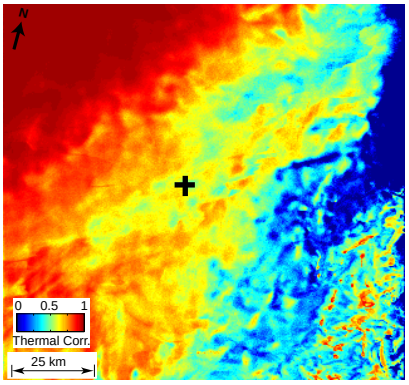

Thermal Decorrelation

Figure 4.16: Expected thermal correlation of Crawford Point. The image was created using Eqn. 4.41 and the average power image in Fig. 4.15. Some, but not all, of the decorrelation can be explained by thermal decorrelation, the rest being a result of temporal effects.

4.4.4 Doppler Centroid Differences

Another component to the spatial decorrelation factor, but which usually has a negligible effect, is the decorrelation due to different squint angles (see Fig. 3.4.) This is due to the same phenomenon described above for surface decorrelation; the azimuthal, or Doppler, spectra for the two SARs will be shifted from one another, and thus the two observations will not be completely correlated [Joughin, 1995]. Therefore another coefficient of spatial decorrelation will be $\rho_{doppler}$, and if similar windowing filters are used for both azimuth and range, it will be identical in form to $\rho_{surface}$.

In Fig. 4.17 we plot $\rho_{doppler}$ as a function of the difference in Doppler centroid, for the ERS system. The PRF of 1100 Hz is the extent of the azimuth bandwidth. For typical ERS viewing geometries the difference in Doppler centroid is small, leading to only a very slight decorrelation. However, $\rho_{doppler}$ would have a detrimental effect if the interferogram were comprised of both ascending and descending orbits, which have Doppler centroids that are different by many times the PRF.

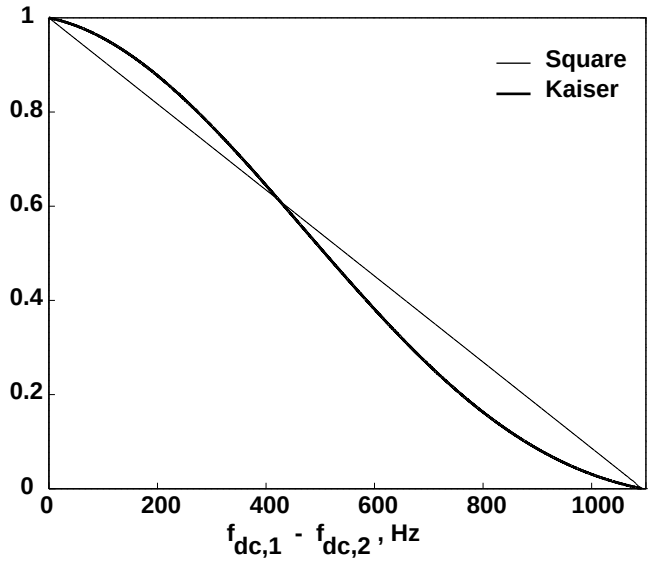

Figure 4.17: Correlation vs. difference in Doppler centroid, in Hertz, assuming ERS parameters. The difference in squint angle leads to spatial decorrelation, as a difference in incidence angle also can cause spatial decorrelation, as shown in Fig. 4.6.

4.5 Conclusion

In this chapter we have examined both the measurement and the theory aspects of the interferometric correlation. In terms of the measurement, the inherent bias in the calculation can lead to difficulties in interpretating correlation data. Fortunately, as we have shown, the bias can be estimated, and in the case of 80-look ERS images, is negligible. On the theoretical side, we have shown that the spatial correlation can be used to derive penetration depths of the terrain, which is a novel approach to studying the polar regions. While we have listed other sources of decorrelation, for most circumstances encountered on the Greenland ice sheet these non-spatial sources can be assumed to not be significant, with the exception of temporal decorrelation. Therefore the two sources of decorrelation that play important roles in determining ρ for the Greenland ice sheets are the spatial and the temporal factors. Thus

$$\rho \approx \rho_{spatial} \cdot \rho_{temporal} \quad . \tag{4.42}$$

In the next chapter we will use ERS Greenland ice sheet data to solve for both $\rho_{spatial}$ and $\rho_{temporal}$, thereby allowing us to determine penetration depths.

Chapter 5

Penetration Depths of the Greenland Ice Sheet

5.1 Introduction

In this chapter we describe the use of ERS correlation data for measuring penetration depths at various locations of the Greenland ice sheet. In particular, we solve for the one-way penetration depth, d, into an (assumed) lossy, isotropic half-space, from the spatial correlation coefficient, $\rho_{spatial}$. As stated previously, this is a novel technique for studying the scattering properties of the Greenland firn. Whereas most Greenland radar studies have concentrated on the amplitude of the radar echoes or the or the interferometric phase, we use the "noise" caused by the spatial separation of the two interferometric antennas as our signal.

There are a few practical issues to contend with before making the measurement. First, the Greenland firn has an increasing density profile, signifying that the medium is not isotropic, as was assumed in the derivation of the spatial correlation model (Sec. 4.3.) In Sec. 5.2 we show that the results of Sec. 4.3 remain valid for a medium with an increasing density profile such as the Greenland ice sheet.

Second, as was explained in Chap. 4, the other important decorrelating factor besides $\rho_{spatial}$ is $\rho_{temporal}$, which includes random changes in the scattering medium over time. In Sec. 5.3 we formulate a least-squares technique to quantify $\rho_{temporal}$, thus allowing us to solve for $\rho_{spatial}$ and the penetration depth.

In Sec. 5.4 we review other measurements of C-band penetration depth in the polar firn. These studies use various techniques of measuring penetration depth, and include

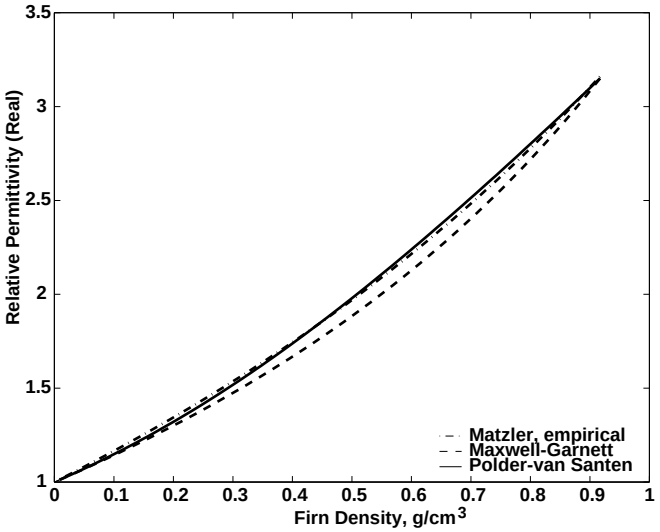

Figure 5.1: Relative permittivity of dry snow as a function of density, for three different mixing models: an empirical model [Matzler, 1987], the Maxwell-Garnett model, and the Polder-van Santen model [Sihvola and Kong, 1988]. Only a slight, and for our purposes, negligible, difference is seen between the models.

both *in situ* and remote-sensing methods. These published results indicate that the C-band penetration depth in Greenland firn is on the order of 10-30 meters.

A brief description of the ERS correlation data from Northern Greenland used in this chapter is given in Sec. 5.5.

In Sec. 5.6, the main part of this chapter, we present penetration depths at four different sites on the Greenland ice sheet, in which we make use of the technique described in Sec. 5.3. We find penetration depths that are consistent with the results in the literature. The conclusion is presented in Sec. 5.7.

5.2 Densification

In Chap. 4 we derived a spatial correlation model in which we assumed an isotropic half-space as the scattering medium. A more realistic model for the scattering volume would, of course, not be isotropic. Density increases with depth, as shown in Fig. 2.4, and causes the permittivity to increase as well. The effective permittivity at a particular depth can

be found by way of mixing formulas [Tiuri et al., 1984; Matzler, 1987; Sihvola and Kong, 1988; Matzler, 1996], which take the local density and the permittivities of the constituents, ice and air, as input. Examples of mixing are plotted in Fig. 5.1. The differences between the curves in Fig. 5.1 can be considered negligible for our purposes. Because of its success in matching microwave data and the ease to which it can be implemented, we chose the empirical model developed for dry snow by Matzler [1987]:

$$\epsilon = 1 + \frac{1.60\rho_f}{1 - 0.35\rho_f}, \tag{5.1}$$

where ρ_f is the local density of the firn as discussed in Chap. 2. At zero density the effective dielectric constant is that of the background air, and when the density is that of pure ice (0.917) then the effective dielectric constant is 3.15.

What consequence does the increase in permittivity with depth have on the volume decorrelation? The signal will now include effects of travel though a medium with a varying permittivity. In this case, the sub-resolution propagation term D_r is

$$D_{r1} = y \sin\theta_1 + \int_z^0 \left[\sqrt{\epsilon(z'')}\,\cos\theta_{r1}(z'')\right] dz''. \tag{5.2}$$

The notation for the y variable remains unchanged, and therefore the densification does not affect $\rho_{surface}$. The volume coefficient ρ_{volume} is affected, however, leading to

$$\rho_{volume} = \left| \frac{\int \sigma_v(z) e^{j\frac{4\pi}{\lambda}\int_z^0 \left[\frac{\sqrt{\epsilon(z'')}\,\delta\theta_r(z'')}{\sin\theta_r(z'')}\right] dz''} dz}{\int \sigma_v(z) dz} \right| \tag{5.3}$$

The power loss as a function of depth in the medium will also be altered, due to the change in the refracted angle:

$$\sigma_v(z) = \sigma_v^0\, e^{2\kappa_e \int_z^0 \left[\frac{1}{\cos\theta_r(z'')}\right] dz''}. \tag{5.4}$$

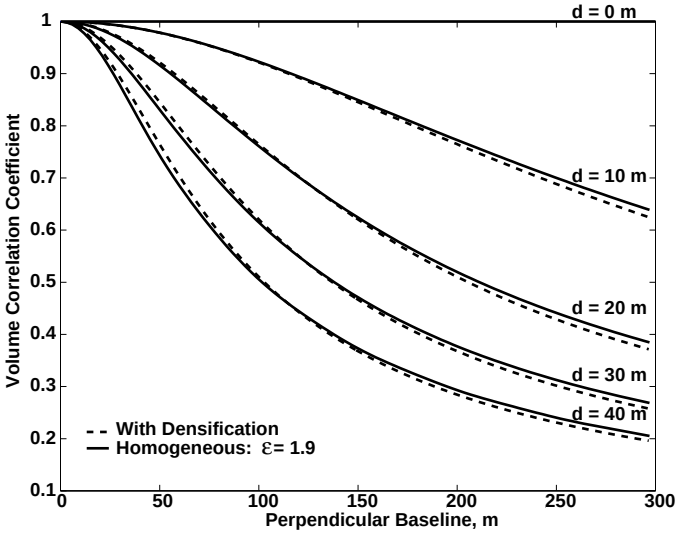

Figure 5.2: Numerical modeling results for volume decorrelation, with densification (dashed lines), and with the isotropic half-space model developed in Chap. 4 (solid lines).

The integral in Eqn. 5.3 cannot be solved analytically for realistic density profiles. Instead, we calculate ρ_{volume} numerically by (1) assuming a standard density profile as given by the two fits to the data in Fig. 2.4, (2) using this profile to calculate the permittivity profile by Eqn. 5.1, (3) calculating the depth-dependent refracted angle by Snell's Law, and (4) substituting $\epsilon(z'')$ and $\theta_r(z'')$ into the above equations. The surface value of ϵ is approximately 1.6 [West, 1994; Forster, 1999], but increases to 3.2 by 100 meters depth. Likewise the angle the radiowave makes with the vertical is 18.0° just below the surface and 12.6° at 100 meters.

A family of curves for different d was generated from Eqn. 5.3 and is plotted in Fig. 5.2, along with the results from the isotropic medium solution using a constant permittivity of $\epsilon = 1.9$. This value of ϵ was chosen to provide a reasonable fit with the depth-dependent permittivity results. We see that, while the isotropic solution underestimates the correlation for small baselines and overestimates the correlation for larger baselines, the difference between the depth-dependent permittivity and the constant permittivity is very small. Thus we can apply Eqn. 4.37 to our ice sheet data to determine penetration depths, even though the density of the firn increases with depth.

5.3 Temporal Decorrelation

Solution for penetration depth from ERS InSAR images, requires us to divide the observed correlation by $\rho_{temporal}$, in order to determine $\rho_{spatial}$. Temporal correlation can be highly variable, both spatially in a given interferogram, and with time from one interferogram to the next.

One approach to quantifying temporal decorrelation is to assume that it is negligible, that is $\rho_{temporal} = 1$. In cases where the two images are acquired simultaneously, as with airborne interferometers, by definition temporal decorrelation is non-existent. Even for repeat-pass interferometry there are dry, vegetation-free terrains for which the temporal decorrelation is negligible over long periods of time. An example is deserts, for which high correlations have been maintained over many years [Amelung et al., 2000]. However, this assumption is normally a poor one for repeat-pass interferograms of glaciers and ice sheets, which may decorrelate completely over a few days [Goldstein et al., 1993].

Another approach is to assume that interferograms with the same inter-observational times exhibit the same temporal decorrelation, or equivalently, that $\rho_{temporal}$ is a function of the temporal baseline T only. All 1-day interferograms would then have $\rho_{temporal} = \rho_{T=1}$, all 3-day interferograms $\rho_{temporal} = \rho_{T=3}$, etc. Thus if we have a 1-day interferogram with a baseline near 0 m, we can interpret the observed decorrelation as purely temporal, and use this value of $\rho_{temporal}$ to determine the $\rho_{spatial}$ of any other 1-day interferograms for the same scene. This approach is valid if the decorrelating process is constant, such as with compaction of the firn, but will not necessarily hold if the process changes daily, for example, as a result of meteorological conditions. In one study by Rott and Siegel [1996], there were instances where two interferograms of the same location in the Antarctic firn, each having the same temporal and spatial baselines, yielded correlations differing by almost 0.2. They concluded that wind was the driving mechanism behind the temporal decorrelation of cold polar firn. We do not attempt to model this random component to $\rho_{temporal}(T)$, but rather the general trend, and therefore any unmodeled decorrelation will be evidenced by the quality of the fit. If the fit residuals are small, we are justified in this simplification.

Our approach here is to model temporal decorrelation as a linear function of time. Such behavior was noted experimentally for Seasat interferograms at L-band in Zebker and

Villasenor [1992]. We have also tested exponential and Gaussian forms for $\rho_{temporal}(T)$, and while all three forms resulted the same penetration depth for each site to within $\pm$ 1 m, the linear form provided a better fit to the data in each case. Thus

$$\rho_{temporal}(T) = a_t + s_t \cdot T, \tag{5.5}$$

where we will allow a_t to vary from unity in order to account for any non-temporal, non-spatial effects such as thermal decorrelation or systematic processing errors, and where s_t is expected to be negative.

We use the linear model of temporal decorrelation above and the results from our spatial decorrelation model to solve for both the penetration depth d and the temporal decorrelation parameters by way of a least-squares algorithm. In other words, we substitute Eqn. 4.29 and Eqn. 5.5 into the equation below

$$\rho_{fit} = \rho_{spatial}(B_\perp, d) \cdot \rho_{temporal}(T, a_t, s_t) \tag{5.6}$$

and calculate a least-squares fit to the observed $\langle\rho\rangle$ to find the optimal d, a_t and s_t. $B_\perp$ and T for each correlation image are known *a priori*. The residual correlation, i.e. the error in the least-squares fit, can be considered either unmodeled spatial decorrelation and/or temporal decorrelation.

Implicit in Eqn. 5.6 are two assumptions. First, the temporal decorrelation is a function of the temporal baseline T only, as discussed above, and second, the penetration depth at each site is a constant for all observations. While the presence of liquid water could alter the measured penetration depth, in the areas where possible melting could occur, all of the observations occurred in winter/early spring months, where above freezing temperatures are highly unlikely, neither was there evidence of liquid water on the surface of the ice sheet in the brightness images.

5.4 Other C-Band Penetration Measurements in Polar Firn

What kind of C-band penetration depth would we expect to see in polar firn? At longer wavelengths (2 m), airborne radar systems are capable of sounding the bedrock topography of the Greenland ice sheet [Gogineni et al., 1998; Moussessian et al., 2000], a round-trip distance of 4-6 km. Even at short microwave wavelengths (2.2 cm) and with the nadir-looking geometry of radar altimeters, there is evidence of 2-10 meter penetration [Davis and Zwally, 1993; Legresy and Remy, 1998] in polar firn. At C-band, Matzler [1987] measured an extinction coefficient of 0.02 m^{-1} for a 29 mm slab of pure ice at $-20°$ C, corresponding to a penetration depth of 50 meters. In terms of absorption losses only, that is, those due to electrical heating of the medium, dry snow would have even greater penetration depths, due to the smaller volume fraction of ice, such that a penetration depth of 125 meters in dry snow is theoretically possible [Matzler, 1987]. As noted in Sec. 3.2.5, however, the penetration depth is dependent on scattering losses as well as absorption. Scattering losses occur when part of the wavefront is scattered by inhomogeneities in the medium and does not contribute to the return echo. Inhomogeneities in the firn could be as small as the individual grains or as large as meter-sized ice pipes. For radiation with off-normal incidence angles, specular reflections from the surface or from buried layers will also result in a part of the total energy being scattered away.

Due to scattering losses, then, we would expect the penetration depth to be less than 125 meters. There have been a few *in situ* results to confirm this. Rott et al. [1993] found a C-band penetration depth of 22 meters in Antarctic firn. Likewise Matzler [1987] found a penetration depth of 25 meters in alpine dry snow. Both of these results were derived from radiometric measurements, in which the transmittance of a successively smaller block of firn was recorded in one case [Rott et al., 1993], or the reflectance of a metal plate was recorded at successively greater depths in the other [Matzler, 1987]. The width of the slab used in both of the experiments was less than 2 m. In contrast to these measurements is the 1-2 m penetration depth found by Jezek et al. [1994]. In this study, a sled equipped with a ground-penetrating C-band radar was employed to detect the sub-surface of the ice sheet. They found that the strength of the echoes dropped off significantly after the first few meters, and measured a penetration depth of 2 m. The experiment took place in the

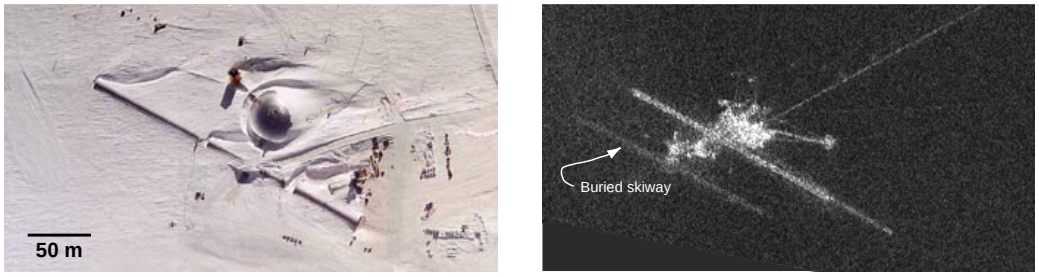

(a) (b)

Figure 5.3: South Pole penetration

percolation zone near Crawford Point during summer 1992. The temperature stayed below freezing and no meltwater was detected at the time of the experiment [Gogineni, 1999].

The result of Jezek et al. [1994] aside, there is further evidence, provided by satellite-borne SARs, that the C-band radiowave is penetrating many meters into the firn. In Fig. 5.3 we present two views of the South Pole station. Shown in (a) is a USGS aerial photograph, in (b), a RADARSAT image. RADARSAT is a C-band SAR satellite, similar to ERS, which was operated in a southward-looking mode for four weeks in Autumn 1997, in order to make a detailed and comprehensive map of Antarctica [Jezek et al., 1998]. In the radar image, coarser resolving capabilities makes it more difficult to identify features. Nonetheless, one feature that is possible to identify is the ~300 meter-long skiway, which is the line running from the upper left to the lower right in both images. In the radar image we can also see a second, fainter line to the left of the bright skiway. This is most probably the old skiway, which is buried under ~10 m of firn. Both images were obtained from the Canadian Space Agency website (www.space.gc.ca), and the radiometric difference between the surface skiway and the buried skiway are unknown. It is clear, however, that the satellite-borne C-band radar penetrates tens of meters into the firn. Several of the other features visible in the radar image also correspond to buried structures.

Another satellite-borne experiment that tests the depth of C-band penetration in polar firn is described by Dall et al. [2001]. In this study a comparison was made between adjacent pixels in topographic images of the Geikie ice cap in Eastern Greenland. The topography maps were derived from an airborne interferometric radar system, EMISAR, operating at

C-band [Madsen et al., 1996]. Because of the relatively abrupt rise to the ice cap, the images include the ice, wet snow, and percolation zones. Corner reflectors on the surface were used to locate the true surface in the interferometric data, and this height was compared to the heights of the surrounding pixels. The pixels containing the corner reflectors appeared to be "floating" off the surface by 6-13 m! This result implies that the "surface" measured for the ice volume was 6-13 m below that of the true surface, because of volume scatter.

To what penetration depth does the 6-13 m difference correspond? In Sec. 4.3.4 the additional phase due to volume scatter was derived:

$$\phi_z = \tan^{-1}\left[-\frac{2\pi\sqrt{\epsilon}\,d\,B_\perp}{R_0\,\lambda\,\tan\theta}\right]. \tag{5.7}$$

This phase arises because the phase center of the resolution element no longer rests at the origin in Fig. 4.5, as it would for surface scatter, but instead lies within the medium, along the line parallel to the wavefront that passes through the origin. Thus the topographic "surface" as measured by the radar interferometer will now be below the true surface, as depicted in Fig. 5.4. The offset between the two can be found by equating ϕ_z with ϕ_{topo} in Eqn. 3.43:

$$z_{offset} = \frac{\lambda R_0 \sin\theta}{4\pi B_\perp}\tan^{-1}\left[-\frac{2\pi\sqrt{\epsilon}\,d\,B_\perp}{R_0\,\lambda\,\tan\theta}\right]. \tag{5.8}$$

We note that this depth is not the depth of the phase center, since ϕ_{topo} does not assume a refractive medium, nor is it the "center of mass" of incoherent scattering given by $\frac{d}{2\cos\theta_r}$. Rather, it corresponds to simply the vertical difference between the true surface and that found by interferometry, assuming an isotropic half-space with loss denoted by the penetration depth, d. In Fig. 5.5 we plot z_{offset} as a function of d for EMISAR parameters. An increasing baseline, as well as a decreasing d, decreases z_{offset}.

From Fig. 5.5, a z_{offset} of 6-13 m corresponds to C-band penetration depths of 14-30 m. Larger penetration was seen at higher elevations, in the percolation zone. Even though these data are from an area less than 50 km from the coast, in a region with a degree of

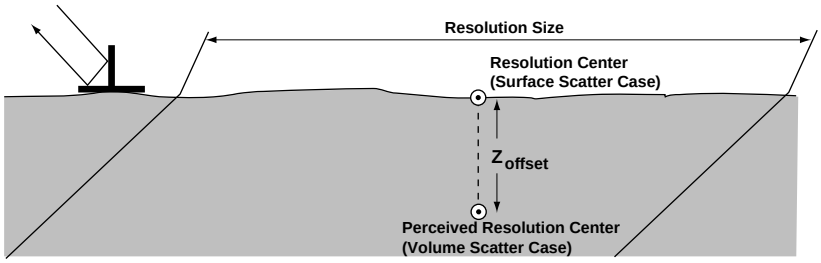

Figure 5.4: The experiment at the Geikie ice cap, as described by Dall et al. [2001]. Corner reflectors were used to compare the height of the true surface with that of the surrounding pixels. Differences of up to 13 meters were found.

geographic complexity which is not representative of the interior of the ice sheet, they do suggest that the radiation from satellite-borne SARs will penetrate a few tens of meters into the Greenland ice sheet. Unfortunately, for the Greenland ERS data analyzed in this thesis, there is no means by which z_{offset} can be found directly, since no "true" surface control was in place at the time of observation.

Based on the published *in situ* and remotely-sensed radar experiments then, we would expect penetration depths on the order of one to three decameters. In the case of the result found by Jezek et al. [1994], it is possible that that the Crawford point radar returns were dominated by a recent dramatic melt event that perhaps does not indicate the structure for other percolation zone areas, such as the Geikie ice cap, or that the radar returns were misinterpreted.

5.5 Data

In the processing of the ERS data presented in this chapter, each ~100 x 100 km ERS scene was multi-looked 20 times in azimuth and 4 times in range, resulting in square pixels ~80 m on a side, as discussed in Sec. 3.2.4. Furthermore, as discussed in Sec. 3.2.3, a Kaiser spectral window was used in both range and azimuth processing for sidelobe reduction. Power, phase (interferogram), and correlation images were produced for each scene. All of the above processing steps occurred at JPL, and copies of the resulting images were donated to us for our study.

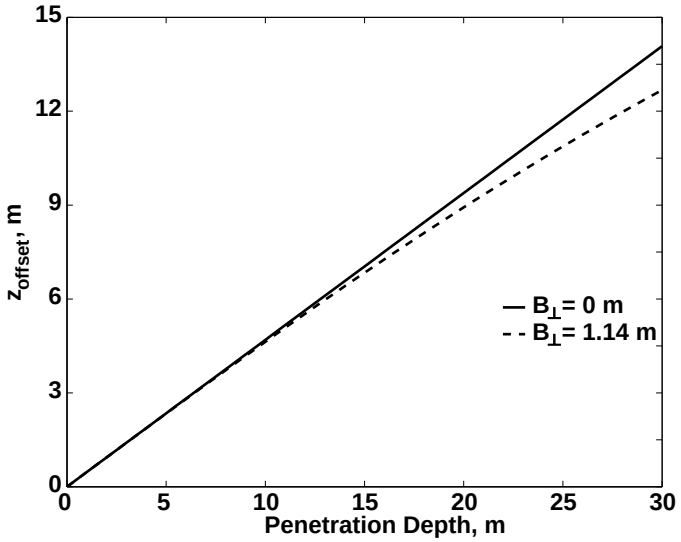

Figure 5.5: The offset between the true surface and the interferometrically-derived surface as a function of penetration depth, assuming the parameters of the EMISAR airborne system [Madsen et al., 1996; Dall et al., 2001].

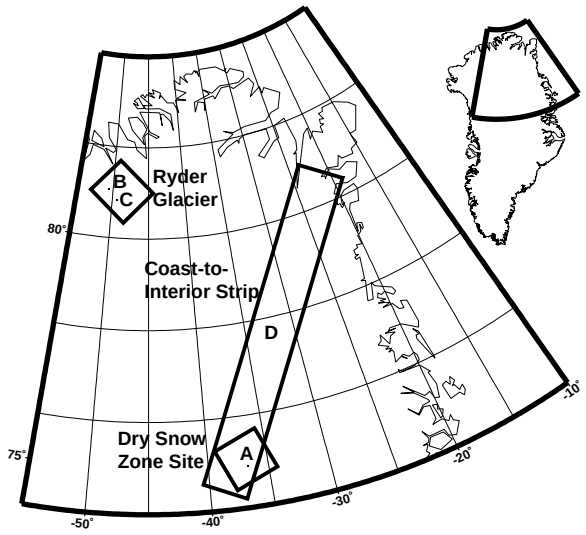

Figure 5.6: Sites A, B, C and strip D on the North-Eastern quadrant of the Greenland Ice Sheet. The small boxes denote one ERS scene (approximately 100 x 100 km); the rectangle denotes 8 concatenated scenes.

Table 5.1: Greenland Site Location and Correlation Image Quantity

Area	**Location** lat./lon., deg.	**# correlation images**
A	74.98/-36.63	10
B	81.17/-51.75	7
C	80.78/-49.05	7
D	80.99/-23.54 - 74.23/-37.13	2

Our study areas are noted in Fig. 5.6, where we consider site A in the dry snow zone of Greenland, two sites B and C around the outlet for the Ryder glacier, and a ~800 km long strip D that extends from the coast into the interior. Table 5.1 lists the approximate location followed by the number of correlation images analyzed for each site.

For sites A, B, and C, a 2.4 x 2.4 km square, corresponding to 900 pixels, was extracted from each of the correlation images that overlapped the location, as described in Sec. 4.2. Care was taken to choose uniform sites in which the correlation statistics did not vary spatially.

The standard deviation of the correlation was also computed. The correlation and standard deviation data for site A were presented in Fig. 4.2 in the discussion of the calculation of the effective number of looks.

Each of the sites A, B, and C, has 7-10 overlapping correlation images with different associated spatial and temporal baselines, which we analyzed using the least-squares algorithm described above. In order to study regional variations in penetration depth, we also examined the two correlation images denoted by strip D. Each of these images represents 8 concatenated ERS scenes. Since there are only two sets of correlation data for site D, then a least-squares approach would not be reasonable. However, one of the datasets has a small $B_\perp$ associated with it, and this dataset is used as the $\rho_{temporal}$ to infer the $\rho_{spatial}$ of the other.

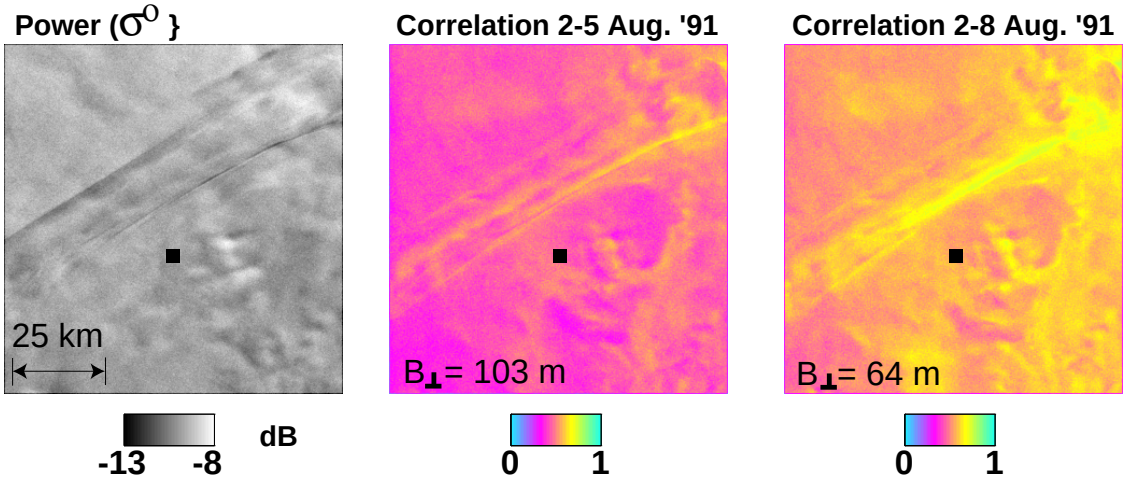

Figure 5.7: A brightness image and two correlation images covering site A (denoted by the black square) in the dry snow zone. The scene corresponds to the square box covering site A in Fig. 5.6. Radar illumination is from the left. The structure running diagonally across the power image is an ice stream that flows to the NE coast. The temporal baseline for the correlation image on the left was 3 days, on the right, 6 days. The first observation in each image was the same. Comparison of the two correlation images shows the dramatic effect of baseline in this area.

5.6 Greenland Ice Sheet Examples

5.6.1 Site A: Dry Snow Zone

Site A, inland and at high elevation, is within the dry snow zone region. Fig. 5.7 shows a power image and two of the ten ERS correlation images that cover site A. The temporal baseline for the correlation image on the left was 3 days; on the right, 6 days. The structure that runs diagonally to the top right in each of the images is an ice stream that flows to NE coast of Greenland [Fahnestock et al., 1993; Joughin et al., 1997].

The 6 day correlation image has a higher correlation than the 3 day image. This confirms that baseline effects, including volume scatter, dominate over temporal effects. Site A corresponds to the black square in each of the images in Fig. 5.7. In Fig. 5.8 (a) the mean correlations, $\langle\rho\rangle$, for ten correlation images covering site A are plotted vs. $B_\perp$, with the number beside each data point denoting the temporal baseline T, in days. Also plotted in (a) are the theoretical curves from our spatial correlation model (Eqn. 4.37) for different

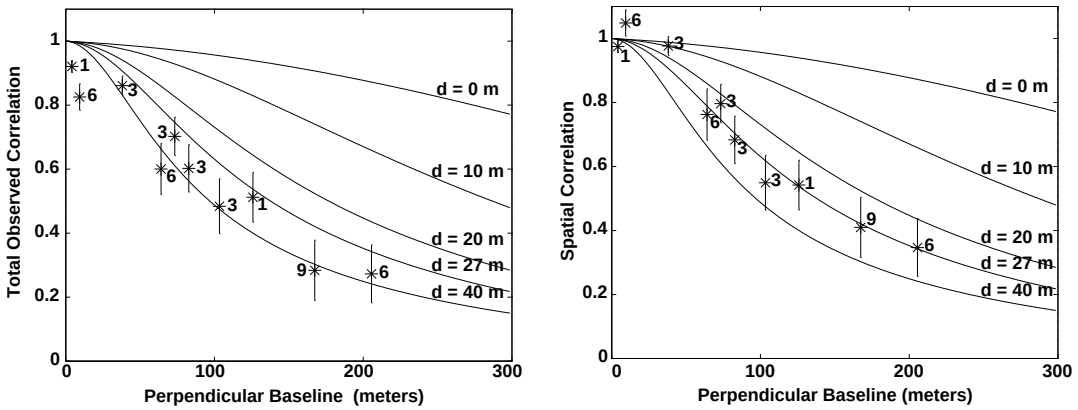

(a) (b)

Figure 5.8: In (a) we plot the measured correlation of site A vs. baseline, where we have also plotted the curves from our spatial correlation model. The error bars indicate the standard deviation of the correlation. Volume effects are evident in the sharp drop-off of correlation with baseline, leading to a critical baseline that is roughly a fourth of the nominal ERS critical baseline. The number beside each data circle denotes temporal baseline (T), in days. Longer temporal baselines show a slight drop in correlation. By estimating and removing the temporal decorrelation in (a) we calculate the residual spatial correlation, shown in (b).

wave penetration depths.

What is remarkable is that for a dataset comprising many different observations over several years (1991-96), including different look directions (the 1-day data were made from ascending passes, all others from descending passes), the data from this site roughly match the shape of a single theoretical curve. This suggests that the decorrelating mechanisms of the terrain do not change much with time or with viewing direction. Because of the large amount of volume scatter a perpendicular baseline over 300 m will result in a correlation under 0.2. Thus care must be taken to choose orbit pairs with small baselines for this region of the world, in order to insure adequate correlation.

Since the temporal baseline for each correlation measurement was non-zero, we would expect some temporal decorrelation. By inspection of the Fig. 5.8 (a) we can clearly see temporal effects. These effects, though, can be seen as modulation on the global trend of fall-off in correlation with baseline, due to volume scattering.

We solve for $\rho_{temporal}(T)$ and d by the least-square method discussed in Sec. 5.3, where

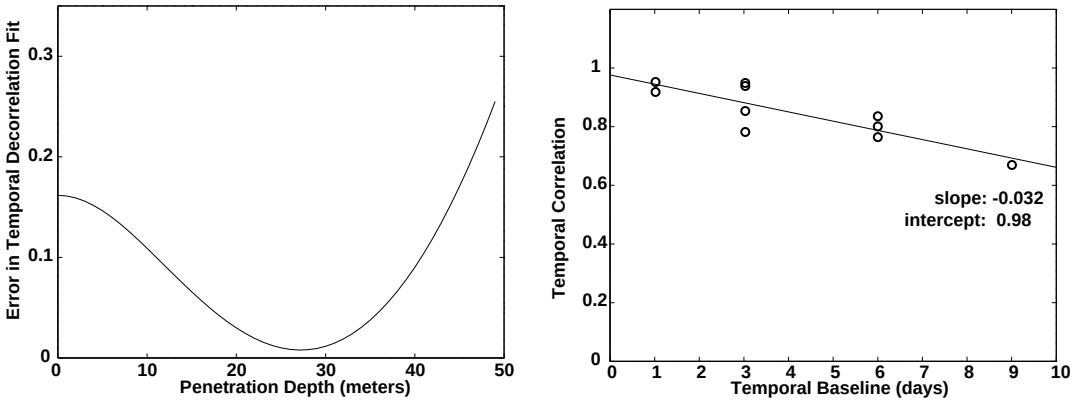

Figure 5.9: Site A optimization results. In (a) we vary d and plot the error in the linear temporal decorrelation fit (Eqn. 5.5.) For the minimum $d = 27$ m found in (a) we plot in (b) the residual temporal decorrelation vs. days between observations. In (b), some points are overlaid: 2 points at T=1, 4 at T=3, 3 at T=6, and 1 at T=9. The linear fit yields a slope of -0.032 $days^{-1}$ and intercept of 0.98.

we fit Eqn. 5.6 to the data $\langle\rho\rangle$. The left side of Fig. 5.9 shows a slice of this minimization. Here we vary over d and plot the error from the best fit of Eqn. 5.5. We find $d = 27$ m. For this value of d the residual temporal correlation along with the best fit line are shown on the right. The slope and intercept of this line are -0.032 day^{-1} and 0.98, respectively.

The decrease of $\rho_{temporal}$ over time indicates that the scattering medium is relatively stable, with a loss of about 0.3 in correlation from 0 to 9 days. 35-day interferograms with significant correlation are not unheard of in this region [Rignot, 1999]. This could be a by-product of the amount of volume scatter (i.e. the scatterers are not as affected by wind), or of the low temperatures and reduced shearing motion of the ice flow in this region.

On the right of Fig. 5.8 we plot the residual spatial correlation, where we have removed $\rho_{temporal}(T)$ as given by the slope and intercept found above. As can be seen by the error in plot (b) of Figs. 5.8 and 5.9 there are spatial and/or temporal effects for which our modeling does not account.

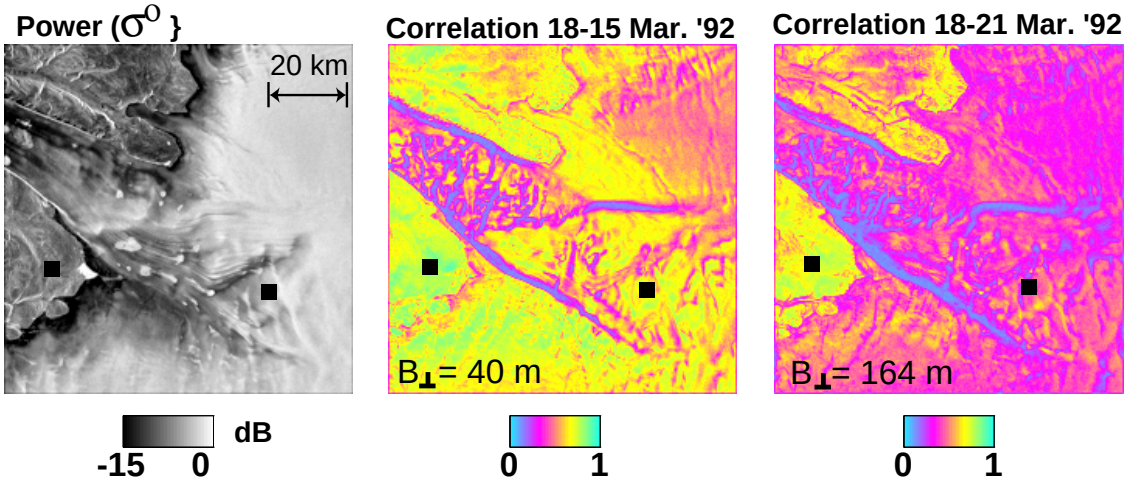

Figure 5.10: A power and two correlation images from the outlet of the Ryder Glacier. This scene corresponds to the box covering sites B and C in Fig. 5.6. Site B is denoted by the square to the lower left of the images; site C the lower right. Radar illumination is from the right. The temporal baseline for each correlation image was three days. The rocky region is in the left of each image. The regions with the greatest decrease with baseline are probably regions with the largest amount of volume scatter, and hence deeper penetration by the incident wave.

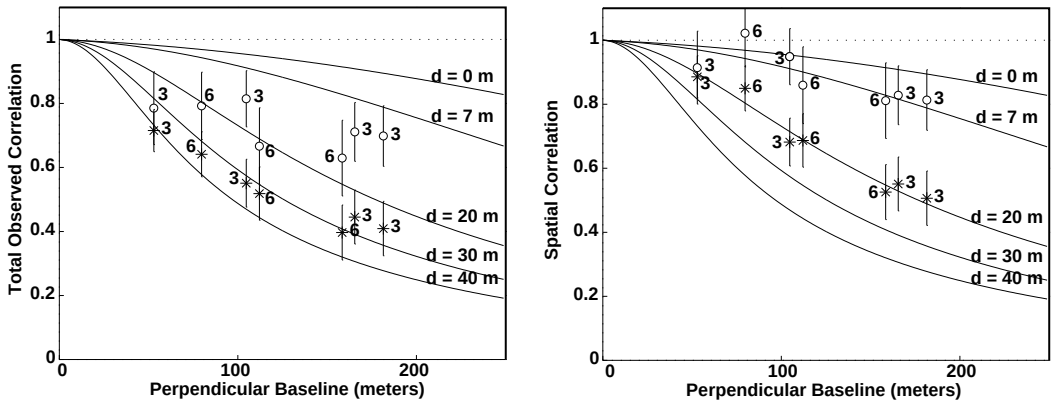

Figure 5.11: Ryder Glacier measured correlation (a) and residual spatial correlation (b), for sites B (circles) and C (stars). The error bars denote the standard deviation of correlation. While both sites suffer from some unaccounted decorrelation, it is apparent from our modeling that the ice stream data (C) experiences a greater wave penetration than the rocky terrain data (B).

5.6.2 Sites B and C: Ryder Glacier

The Ryder Glacier is an outlet glacier on the northern coast of Greenland (map shown in Fig. 5.6). In the scene we analyze here both the glacier and the rocky outcrops of the coast are visible. In Fig. 5.10 a power image and two correlation images are shown. The rocky terrain is the highly correlated region in the upper left of the image. The glacier flow between the rocks on the left side of the images is of lower correlation due to the shearing motion of the flow and other temporal effects.

We would expect the incident wave to not penetrate the rocky surface, while for the glacier we would expect some degree of wave penetration. This is consistent with the correlation images in Fig. 5.10, where the icy terrain suffers enhanced volume decorrelation with increasing baseline as compared to the rocky surface.

Seven correlation images were produced for this scene. The results are shown in Fig. 5.11, where in (a) we plot the mean correlation values, $\langle\rho\rangle$. Site B within the rocky terrain has consistently higher correlation values than the glacier site C. Using the least-squares technique described in Sec. 5.3 we solved for the penetration depths and temporal decorrelation in each area. On the right of Fig. 5.11 are the residual spatial correlation values, similar

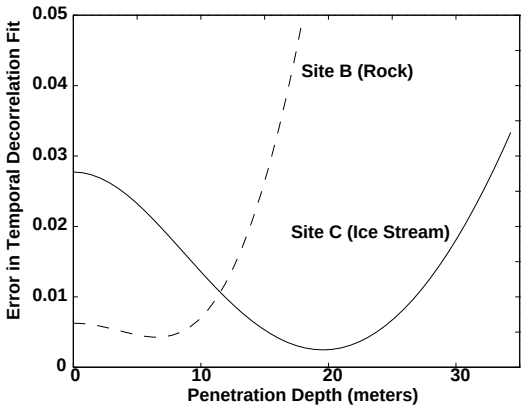

Figure 5.12: Ryder Glacier optimization results for the rocky coast site B and ice stream site C. We find minima at d = 7 and 20 m, respectively, though inspection of the site B result shows that the minimum is less well-determined than the site C depth, and could be less than 7 m.

to Fig. 5.8 for the dry snow zone. The results for sites A, B, and C are summarized in Table 5.2, where we have included a 68% confidence interval associated with our penetration depth measurement. This interval was calculated from a Monte Carlo error analysis, where each value of $\langle\rho\rangle$ was varied according to its standard deviation, and a distribution of penetration depths was produced for each site.

As shown in Fig. 5.12, we calculate through least-squares methods a "penetration" depth of 7 m for the rocky terrain. While it would make sense that a very rough surface could be considered a volume of scatterers, we realize that applying our embedded scatterer model to rough terrain where the radiowave does not penetrate the surface is not appropriate for quantitative analysis. Therefore we do not intend the one-way penetration depth of 7 m or even the two-way penetration depth of half this value to indicate the height dispersion of the surface for a given pixel, since the depth determination was made using a model based on embedded scatterers in a lossy ice medium, not a rough air-rock interface. In fact the depth determination is poorly bound on the lower end, as can be seen in Fig. 5.12 and correspondingly in the confidence interval for site B listed in Table 5.2. Thus we would conclude that d <8 m for this site. More surface scatter-only data are needed before assessing the accuracy of our surface scatter decorrelation model, though Zebker and Villasenor [1992] observed more surface decorrelation than expected for InSAR images of

Table 5.2: Dry Snow Zone and Ryder Glacier Results

Location	d, m	68% Conf., m	a_t	s_t, $days^{-1}$
Site A	27	23-31	0.98	-0.032
Site B	7	1-8	0.94	-0.028
Site C	20	16-24	0.86	-0.018

the Death Valley.

On the other hand, the optimization of site C shown in Fig. 5.12 yielded a distinct minimum around $d = 20$ m. Even with the error associated with site B it is apparent in Fig. 5.11 (a) and (b) that the icy terrain of site C experiences an enhanced decorrelation as a function of baseline, and thus, by our modeling, it experiences greater wave penetration. The observed penetration depth for sire C is less than that found for site A in the dry snow zone. This may be because the ice layer near the coast is broken up by the ice motion or has structures within the medium from melting/freezing, and thus presents more shallow facets to scatter the incident wave.

From Table 5.2 we see that the measured fall-off in temporal decorrelation as denoted by s_t for site C was significantly less than that of site A and B, which is surprising, given the comparative mobility of the icy flow compared to the interior site and to the rocky terrain.

5.6.3 Strip D: Coast to Interior

Two ERS 1/2 tandem pairs were acquired over the strip D (as shown in Fig. 5.6), the first on 11-12 January 1996 and the second 15-16 February that same year. Fig. 5.13 includes four different representations of this 8 scene-long strip. On the far left is a power image, where we can clearly see three different zones: the coastal region, the bright percolation zone, and the darker dry snow zone in the interior. Also apparent in the lower half of the image is the ice stream that flows to the NE of Greenland. The next figure is a correlation image from the 11-12 January tandem pair, where the baseline is small (24 m at the coast down to 1 m in the interior.) As we can see the entire strip is highly correlated, except for small patches in the rocky terrain. In stark contrast to this is the second correlation image, which has a much larger baseline (134 m at coast to 124 m in the interior), and which has a lower overall correlation as well as a higher degree of variation.

Why is there a large difference between the two correlation images? Based on the results presented in Secs. 5.6.1 and 5.6.2, we argue that the dissimilarities are due to spatial decorrelation. On the other hand, if the reason were temporal, and there were a mechanism in place (other than melting) that could dramatically alter the ice sheet correlation from day to day, then we would expect that the differences would manifest in the local weather data. Unfortunately, the closest weather stations on the ice sheet in service at the time the ERS data were acquired were the NASA-U and Humboldt weather stations, whose locations are shown in Fig. 5.14. While there are several hundred miles between the stations and Strip D, any weather patterns that could cause an 800 km-long variation in correlation would likely be apparent in the data at these two stations.

In Fig. 5.15 and Fig. 5.16 we plot the weather data from NASA-U and Humboldt stations, respectively, around the time of observations. The Humboldt temperature data for much of February 15-16 1996 is missing. Accumulation data, which is not shown, showed no signs of precipitation at either station. The temperature and wind speed data indicate that conditions were not dramatically different during January 10-11 as compared to February 15-16. Thus the most likely explanation for the difference between the two correlation images of Fig. 5.13 is that spatial correlation, due to the differences in baseline, is the cause.

From a comparison of the rocky terrain we conclude that this spatial decorrelation cannot be due to surface scatter alone. In the second correlation image we also can see the separation of the lower correlated percolation zone in the interior with the higher correlated bare ice zone that abuts the coast [Fahnestock et al., 1993], which is difficult to discern in either of the first two images on the left.

The fourth image is a map of penetration depths inferred from the correlation images, where we have corrected for temporal decorrelation by assuming the first correlation image represents the temporal decorrelation only. This approach is reasonable considering its small baseline. Notice in this case that the coast is found to have zero penetration. Values for d over the ice sheet range from 10 m in the bare ice zone, 15-35 m in the percolation zone, and 15-38 m in the dry snow zone.

Apparent in the second correlation image are small-scale (< 10 km) variations in correlation that match the power image. They are particularly apparent in the ice stream

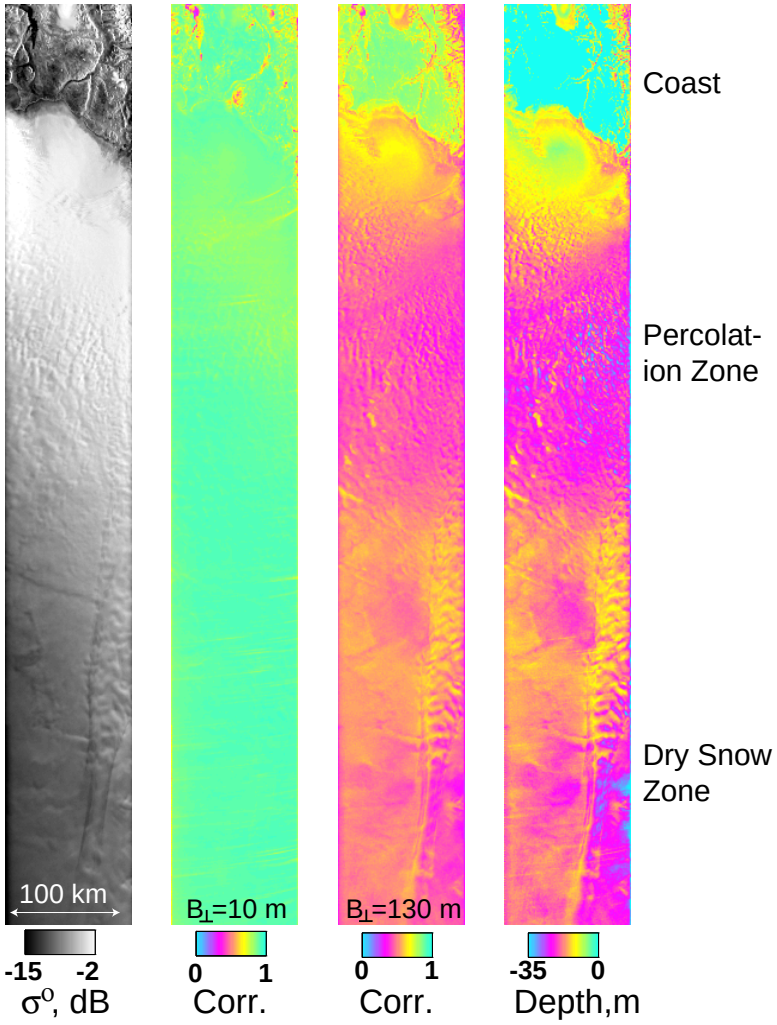

Figure 5.13: Coast-to-the-Interior. As shown in Fig. 5.6, this 800 kilometer-long strip D, including 8 ERS scenes, extends from the rocky coastal area through the percolation zone into the dry snow zone. From left to right we show a brightness image, correlation image ($B_\perp$ = 24-1 m, top-to-bottom), a second correlation image ($B_\perp$ = 136-124 m), and a penetration map made from the second correlation image, respectively. The first correlation image, due to its small baseline, is highly correlated and little detail is apparent. A greater contrast is seen in the icy regions in the second correlation image because of the increased baseline and significant wave penetration. The coastal area, due to the minimal volume scattering, remains highly correlated. In the fourth image we have used our model to invert the second correlation image into penetration depth. The percolation zone is shown to have equal or greater penetration than the dry snow zone.

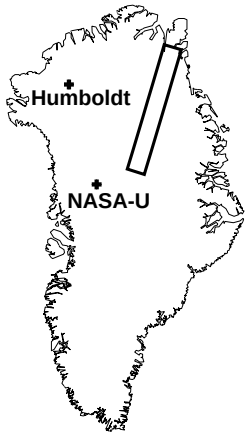

Figure 5.14: Location of the NASA-U and Humboldt weather stations.

undulations in the lower half of the strip. This connection between brightness and interferometric correlation might suggest that thermal effects, due to changes in SNR, are dominant. But as stated earlier the SNR over the icy terrain was above the threshold where this would be apparent. As evidence the small baseline correlation strip yielded a high, uniform correlation, which would not be the case if thermal decorrelation dominated. Analyses of these small-scale variations in power and correlation and their relation to topography will discussed in Chap. 6.

5.6.4 Penetration Depth Discrepancy

Interestingly, the percolation zone, while much brighter, shows approximately the same penetration depths as the dry snow zone. Rignot [1995] developed a scattering model that had some success in explaining the airborne polarimetric radar observations of the percolation zone. In this model, buried ice pipes in the first few meters were the dominant scattering mechanism. The assumption of the depth of scattering was based on the *in situ* radar experiments at Crawford Point by Jezek et al. [1994] that were discussed in Sec. 5.4. If this is true we would not expect significant volume decorrelation in this region, which is contrary to our map of penetration depths.

Why is there a discrepancy between the *in situ* result of Jezek et al. [1994] and our

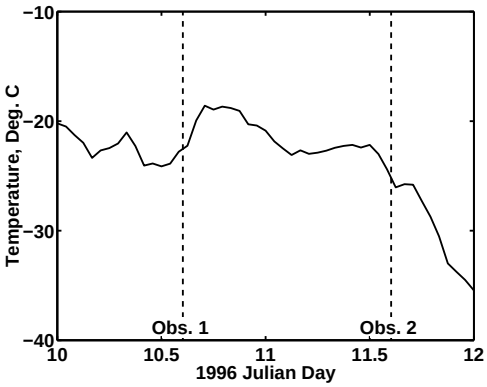

(a) NASA-U Temp. Jan. 10-11 1996

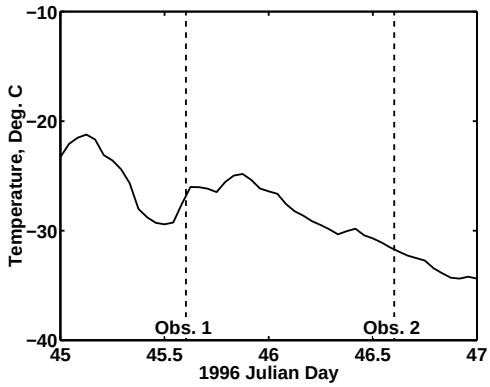

(b) NASA-U Temp. Feb. 15-16 1996

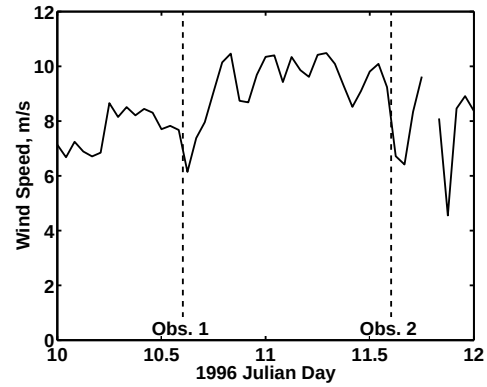

(c) NASA-U Wind Spd. Jan. 10-11 1996

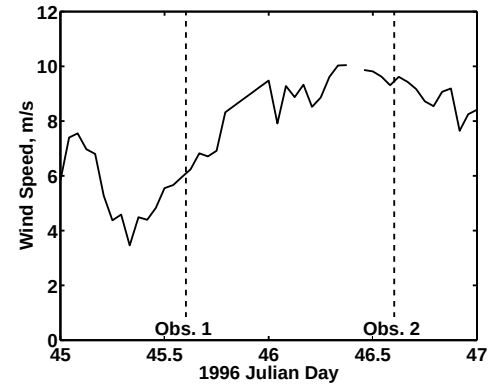

(d) NASA-U Wind Spd. Feb. 15-16 1996

Figure 5.15: Temperature and wind speed data from NASA-U weather station around the time of observation for the two correlations images shown in Fig. 5.13.

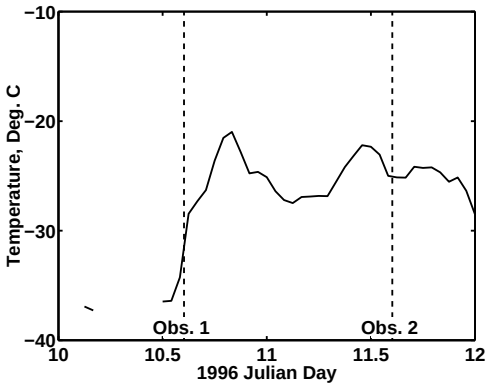

(a) Humb. Temp. Jan. 10-11 1996

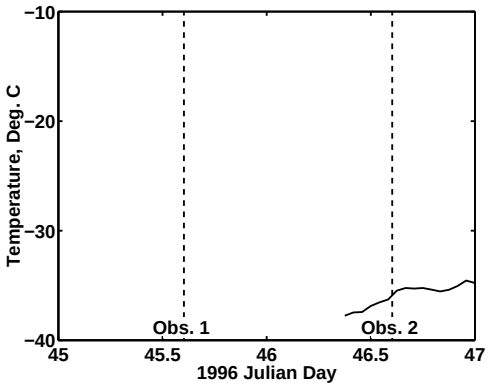

(b) Humb. Temp. Feb. 15-16 1996

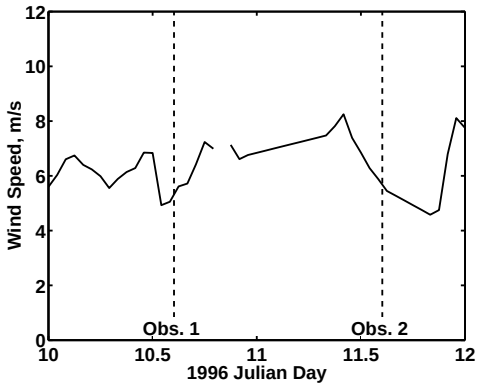

(c) Humb. Wind Spd. Jan. 10-11 1996

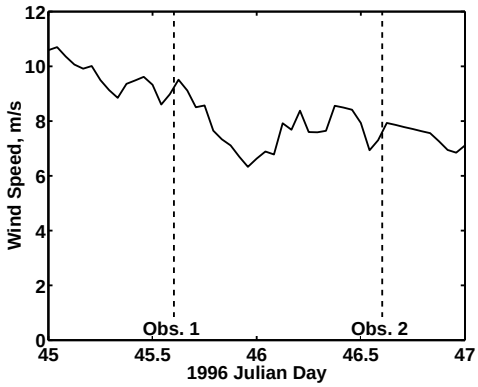

(d) Humb. Wind Spd. Feb. 15-16 1996

Figure 5.16: Temperature and wind speed data from Humboldt weather station around the time of observation for the two correlations images shown in Fig. 5.13.

findings for d in the percolation zone? As explained in Sec. 5.4 there is evidence from the percolation zone of the Geikie ice cap that penetration depths of over 20 m are possible [Dall et al., 2001], and thus it is possible that the GPR results of [Jezek et al., 1994] are either in error or not indicative of the rest of the ice sheet. Furthermore, the percolation zone does not seem to be lacking in scatterers at depth, as Benson [1962] found evidence of "pronounced melt structures" at depths greater than 50 meters in the percolation zone of North-Western Greenland.

If our findings are in error, then perhaps there are processes leading to spatial decorrelation in this region for which our model does not account. Rignot [1995] modeled the ice pipes as cylinders that were situated at least several wavelengths apart, such that they were considered uncorrelated with each other. Therefore his model does not include "multi-bounce" mechanisms, only the complete electromagnetic solution for scattering from a single cylinder, as derived by Bohren and Huffman [1983], with many realizations over length, tilt angle, and so forth. The reason for the large degree of backscatter in this region was explained by the "glory" effect caused by the rounded cylindrical form of the ice pipes [Rignot, 1995].

If the scattering is uncorrelated from scatterer to scatterer, then the only spatial decorrelation not found in our volume scatter model would be the effect of the change in incidence angle on each individual scatterer. That is,

$$\rho_{scatterer} = \frac{< f(\theta_1) f^*(\theta_1 + \delta\theta) >}{< f(\theta_1) f^*(\theta_1) >}, \tag{5.9}$$

where we have assumed that the scatterers are identical, with uniform distribution, and have complex reflectivity f. Now

$$\rho_{spatial} = \rho_{surface} \cdot \rho_{volume} \cdot \rho_{scatterer} \quad . \tag{5.10}$$

The amount that a scatterer decorrelates due to changes in incidence angle is directly

related to its size, as it can be considered a coherent aperture with a beam pattern determined by its length and its orientation. Decorrelation results when the first and second SAR observations are in and out of the beam pattern, respectively, or vice-versa. How long an aperture on the ground is needed to produce decorrelation in two observations that are 830 km away, and which are separated by ~300 m? If we consider the antenna beam patterns of the ice pipes to be *sinc*-functions in form (defined in Eqn. 3.8), and the ice pipes that dominate the return to be oriented parallel to the wavefront, then the length of the ice pipe would have to be

$$\ell_{pipe} = \frac{\lambda R_0 \cos\theta_r}{2\sqrt{\epsilon}\cos\theta B_\perp} = 60\,m, \tag{5.11}$$

where we have taken into account the refractive medium. Obviously this is not realistic! Therefore, we find no other decorrelating source that could account for the measured spatial decorrelation *other* than scatterers at depths much greater than a few meters contributing to the return echo.

5.7 Conclusion

Our results indicate that the penetration depth of the Greenland ice sheet ranges from about 10-30 m, consistent with other published data. Past ERS SAR studies of Greenland have used either the amplitude of the return or interferometric phase for analyzing the upper firn. Our approach, which gives insight into the vertical extent of the scattering medium, is to use the second-order information in the amplitude and phase by calculating the correlation. From correlation images presented in this chapter we conclude that the standard model for surface scatter alone can not explain the extent of the decorrelation in interferometric images of the Greenland Ice Sheet, confirming the existence of a significant amount of volume scatter. Using the volume decorrelation model developed in Chap. 4, we invert the measured correlation to obtain penetration depths. We measure C-band penetration depths averaging 27 m in the dry snow zone, 20 m near the outlet of the Ryder glacier, and produce a map from the coast to the interior with penetration depths of 12-35 m for the

icy terrain. These results are consistent with both *in situ* and remotely-sensed studies done in similar terrain in polar firn. While there is significant uncertainty associated with this technique (see Table 5.2), correlation-based measurement does allow us to make estimates of the penetration depth, not just for one location, but for the wide coverage afforded by satellite-borne radars.

Our results also indicate that the effective critical baseline, the value of $B_\perp$ at which the correlation is so poor as to make the interferometric phase unusable, is greatly reduced over the Greenland Ice Sheet due to volume scatter. For interferometric images over terrain with surface-scatter only, the ERS effective critical baseline is greater than 1 km, whereas over the Greenland Ice Sheet, judging from the results of sites A and C, it is 250-300 m.

In measuring penetration depth values we also determined the amount of temporal decorrelation in the correlation image. We found unexpectedly that the interior site A suffers more from temporal effects than does the the coastal site C. Interferograms with longer temporal baselines are desired to determine the form of $\rho_{temporal}(t)$ more accurately.

Analysis of the variations in spatial correlation and the return power, as seen in Fig. 5.13, will be the subject of Chap. 6.

Chapter 6

Variations in Dry Snow Zone Structure

6.1 Introduction

In the previous chapter we showed how radiowave penetration depths in polar firn can be measured via the interferometric correlation. While penetration depth values are useful for characterizing regions of greater or lesser volume scatter, to this point our measurements have not aided in the estimation of more important scientific variables, such as mass balance terms. As noted in Chap. 2, the large uncertainty associated with the mass balance measurement is the spatial sparseness of accumulation data. Thus accumulation rates derived from a remote sensing dataset, especially having the coverage and resolution of space-borne SARs, would be extremely useful.

In this chapter we analyze two radar scattering models used for deriving accumulation rates. At present we only test the feasibility of these models, and reserve detailed examination of this problem for the future. By comparing the results of the models to both ERS power and correlation data, we find the first scattering model, which is based on the assumption that scattering is dominated by the individual snow grains, does not provide an accurate match to the data and also can not explain other ancillary data. The second model, based on a scattering from buried interfaces, appears to explain the radar data more accurately. We use the second model to produce a map of variations in accumulation rate over a small region in the dry snow zone.

Why should radar observations yield constraints on accumulation rate? The connection is illustrated below, where by "$\rightarrow$" we mean "influences" :
Since, as we have found, the two-way C-band radiowave signal penetrates 10 or more meters into the upper firn, the return echo carries signatures of the sub-surface structure. These

signatures are present in the depth of penetration and also the total amount of energy backscattered to the radar. In the dry snow zone, where melting does not occur, accumulation rates play a prominent role in determining radar backscatter signatures, as grain sizes and the thickness of the annual layers are directly dependent on accumulation [Zwally, 1977; Long and Drinkwater, 1994; West, 1994; Forster, 1999]. Here we investigate the effects snow grain size (Sec. 6.4) and annual layer thickness (Sec. 6.6) have on InSAR data. In particular, we focus on small-scale (< 20 km) horizontal variations in the Greenland ice sheet radar data.

Scatterometry, radiometry, and optical satellite imagery studies comprise a more comprehensive viewpoint of the entire ice sheet, but due to their coarser resolving capabilities they are not sensitive to these local variations. In zones other than the dry snow zone the radar return is dominated by melt effects [Fahnestock et al., 1993]. In these regions it is unknown what effect accumulation rate has on the radar data, though possible links have been investigated by Long and Drinkwater [1994]. Because it presents a slightly more tractable problem, in this chapter we will restrict ourselves to dry snow zone data.

Exact modeling of the InSAR return, even for the dry snow zone, is difficult, due to the large number of unknowns. In terms of measurable quantities ERS SAR data suffers in particular because it has only one polarization state (VV), a small range of incidence angles ($19.5°$-$26.0°$) compared to scatterometry or airborne SARs, and a resolution that, although only a few tens of meters, is still too large to be able to image individual snow layers, such as is possible using ground-based ground-penetrating radars. However, with the inclusion of correlation data with power data we double the usable dataset, so that, for each pixel in the image, we have not only the strength of the return echo but also a measure of the vertical dispersion of scatterers, which is a novel approach to analyzing InSAR data. The phase of a pixel, other than through a possible measurement of z_{offset} (Sec. 5.4), gives no

direct indication of the structure of the firn, since it is relative.

6.2 Power and Correlation in the Dry Snow Zone

Comparing the power image and the long baseline correlation image in Fig. 5.13, we note that in the dry snow zone there appears to be patterns common to both images. These variations, as we shall see, are caused by topographic undulations. The undulations themselves are believed to be caused by the flow of the North-East ice stream over obstructions in the underlying bedrock [Ekholm et al., 1998].

Fig. 6.1 we show (a) a shaded relief map of a DEM (courtesy of Ian Joughin, JPL), (b) the corresponding power image of this region, and (c) the 127 m baseline correlation image, each in grayscale. The geocoded scene shown in these images is the same as the region in the lower part of Fig. 5.13. The black line in the images denotes a transect whose 1-D profile we will discuss below.

It is clear from Fig. 6.1 that corresponding variations are seen in topography, power, and correlation. Within the ice stream, whose shear borders are marked by the dark gray lines in the power image, there are more topographic undulations than outside the ice stream, and we see an increase in power and correlation variation. Outside of the ice stream, where the ice sheet is relatively flat, we see little spatial variation in the scene reflectivity or the correlation.

The ice stream profile is shown in Fig. 6.2, where increasing distance corresponds to displacement from the bottom to top of the black line in Fig. 6.1. The topographic undulations are very gentle compared to common terrestrial terrain, with amplitudes of only about 40 m over wavelengths of 10-20 km. To scientists making field measurements it is difficult to determine on which side of these "hills" they are situated [Bindschadler, 1998a]. On the other hand, the power and correlation data show dramatic contrasts, with factors of two apparent in Fig. 6.2. Interestingly, the power and correlation cycle in phase, but are approximately 90° out of phase with the topography, that is, the power and correlation are maximum on one side of the topographic undulations, and minimum on the other. In terms of power, this phenomenon has also been observed in Radarsat images of Antarctica [Sohn et al., 1999; Fahnestock et al., 2000].

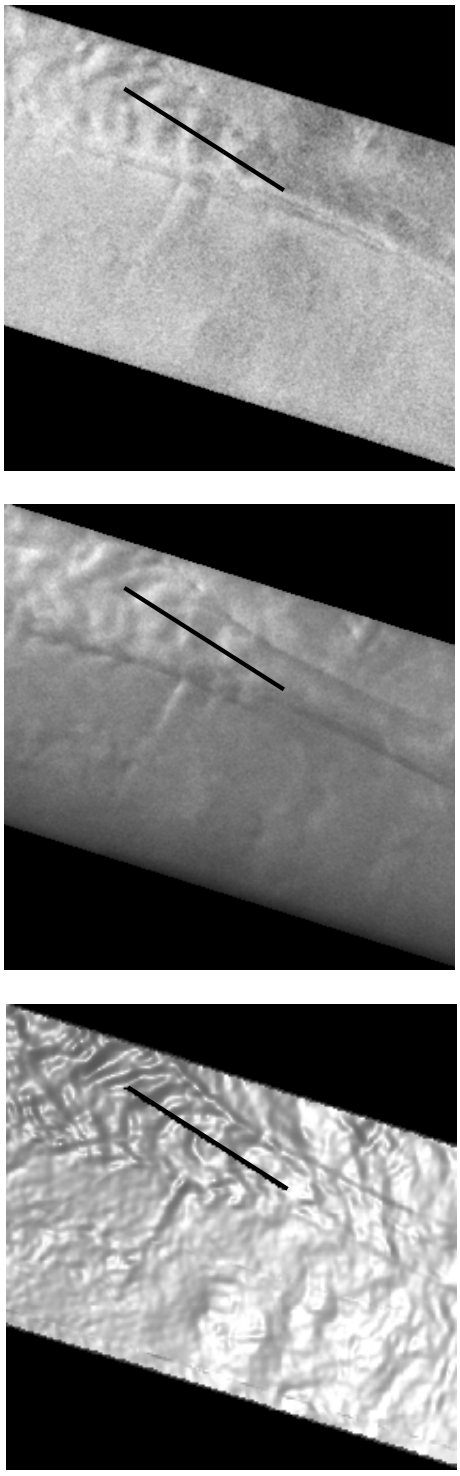

Figure 6.1: A shaded relief map (a) of an area within the dry snow zone of the Greenland ice sheet, with (b) power and (c) correlation images of the same scene. The correlation has an associated perpendicular baseline of 127 m.

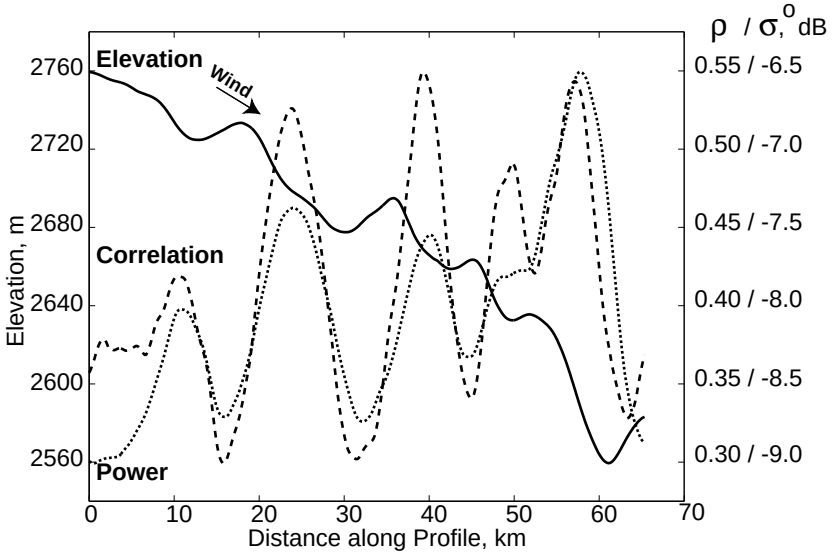

Figure 6.2: A profile of the dry-snow zone images shown in Fig. 6.2. The direction of the profile is from the lower to upper part of Fig. 6.2. Power and correlation is found to have maxima on the downslope sides of the topographic undulations.

Observations of other terrain do not necessarily show the same behavior as seen Fig. 6.2. For example, in InSAR observations of rocky terrain both the backscattered power and correlation are largely determined by the surface slope. By examining Eqn. 3.24 for power and Eqn. 4.27 for correlation, we see that as the incidence angle θ decreases, the return power increases and the correlation decreases. Both of these effects are due to the increase in the size of the resolution cell (Eqn. 3.27), since a larger resolution element will increase the number of scatterers adding to the return echo, but will decrease the correlation because the "ground aperture", as discussed in Sec. 4.3.4, will be larger. We witness this effect for InSAR images of the rocky coast of Greenland, shown in Fig. 6.3, where the radar look direction is from the right. The imaged scene has a sharp depression that runs vertically through the image. As we can see the power and correlation images are inverted copies of one another, as the bright lines of foreshortening/overlay exhibit low InSAR correlation.

Since the slopes encountered on the Greenland ice sheet are less that 1°, then any tilt effects, such as those affecting the rocky coast images, are negligible. There then two main questions regarding the power and correlation observation of the dry snow zone: (1) Why

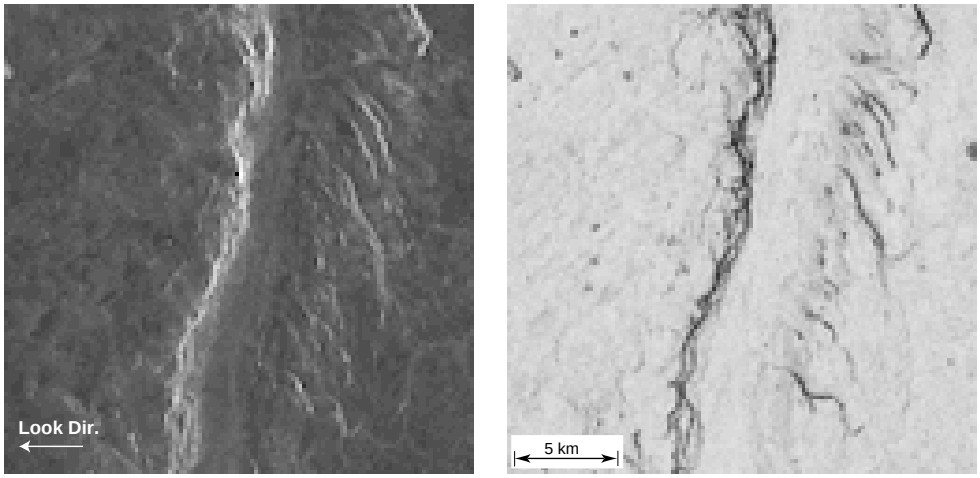

(a) Power (b) Correlation

Figure 6.3: Power (a) and correlation (b) over rocky terrain. Notice that power and correlation are inversely-related, due to the sloping of the terrain towards the radar. In areas where the slope is facing the radar, the return power increases, while the spatial correlation coefficient decreases.

do power and correlation observations of the ice sheet vary together? and (2) what is the cause of power and correlation variations? The first question we attempt to answer below, the second is the basis for our modeling investigations in Sec. 6.4 and Sec. 6.6.

6.3 Reasoning for Similarities in Power and Correlation

It is not surprising that InSAR power and correlation observations of the dry snow zone vary together when we consider volume scatter. From Eqn. 3.32,

$$\sigma^0 = \frac{\sigma_v^0 \cos\theta_r}{2(\kappa_s + \kappa_a)}, \tag{6.1}$$

where we have substituted the sum of the scattering and absorption coefficients for the extinction coefficient (Eqn. 3.28.) The volumetric backscatter coefficient σ_v^0 and the scattering coefficient κ_s are somewhat analogous in nature; the former indicates how well the average point in the volume scatterers energy back to the radar, the latter how well a point in the

volume scatterers energy over all angles [Ishimaru, 1978]. For scatterers small compared to the size of a wavelength, there is a proportional relationship between σ_v^0 and κ_s. For spheres [Ishimaru, 1978],

$$\sigma_v^0 = \frac{3\,\kappa_s}{2}. \tag{6.2}$$

Substituting Eqn. 6.2 into Eqn. 6.1, we find

$$\sigma^0 = \frac{3\,\kappa_s\,\cos\theta_r}{2\,(\kappa_s + \kappa_a)}. \tag{6.3}$$

For correlation, assuming that all the spatial variation seen is from changes in volume correlation (Eqn. 4.37), we have:

$$\rho_{volume} = \frac{1}{\sqrt{1 + \alpha\,(\kappa_s + \kappa_a)^{-2}}}, \tag{6.4}$$

where α is a constant for a given interferometric viewing geometry. The functions expressed in Eqns. 6.3 and 6.4 are plotted in Fig. 6.4 for an increasing κ_s, where we neglect the effect of thermal noise on the received signals. As shown, σ^0 and ρ_{volume} have similar behavior as a function of κ_s, and thus it is to be expected that, in the radar images, power and correlation vary together.

We interpret Fig. 6.4 as follows: at low values of the scattering coefficient, little energy is scattered back to the radar and there is only a slight amount of received power. The correlation is low because the depth of penetration is at its greatest value, though some of the signal is absorbed due to the non-zero value of κ_a. As κ_s increases, more energy is scattered back to the radar, increasing σ^0, but more energy is also scattered in other directions, and thus the penetration depth decreases, increasing ρ_{volume}. For the simple scatterers assumed here, a limit is approached in both backscattered power and correlation as the scattering coefficient increases, since all the energy is scattered from near-surface interactions. This does not imply that terrain exhibiting surface scatter has only one possible

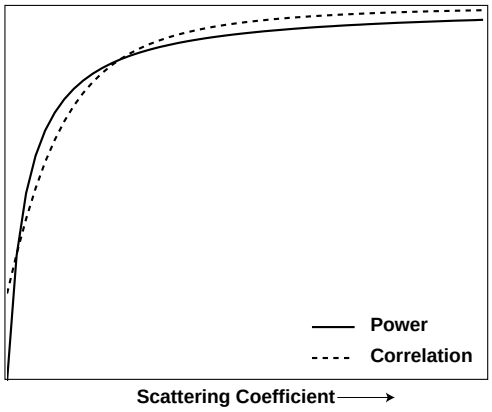

Figure 6.4: The effect of increasing scattering coefficient on return power and volume correlation.

value of σ^0, rather, that for a volume of diffuse scatterers a maximum return power and depth of penetration is approached as the scattering efficiency of the scatterers increases.

A simple explanation for the variations seen in the profile of Fig. 6.2 is variations in the scattering coefficient. Thus κ_s increases on one side of the undulation and decreases on the other. What mechanism could produce this difference in scattering characteristics between the two sides? The driving force behind this difference is believed to be the prevailing winds [Sohn et al., 1999; Fahnestock et al., 2000]. The winds in this region are largely due to katabatic processes, that is, downslope winds that result from the cooling effect of the ice sheet [Benson, 1962]. Zonal circulation patterns play a lesser role [Box, 1999]. The direction of the average prevailing winds for the three closest weather stations to our area of study are shown in Fig. 6.5. The direction of the prevailing winds is essentially along the profile, as noted in Fig. 6.2. Thus we measure more backscatter on the lee side of the hill, and less on the windward side, consistent with other satellite radar measurements [Sohn et al., 1999; Fahnestock et al., 2000]. These variations in power are matched by the variations in correlation, which we interpret as changes in the depth of penetration, shown in Fig. 6.6, where we have calculated the penetration depth from a profile of the penetration map in Fig. 5.13. The scenario that we suggest of the wind, topography, and radar signal is depicted in Fig. 6.7.

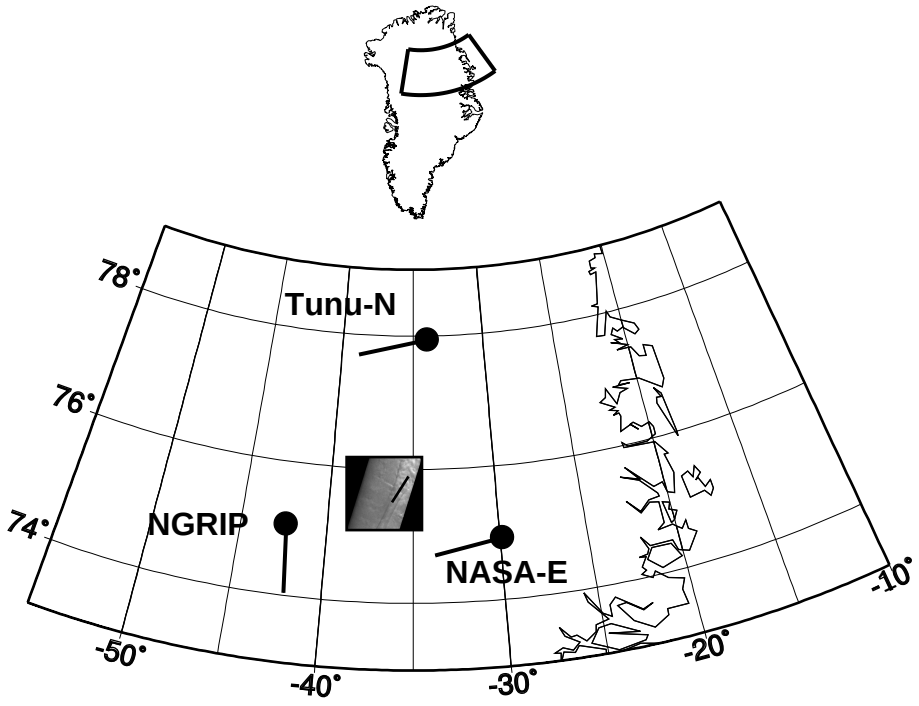

Figure 6.5: The direction of the average prevailing winds in proximity to the imaged scene in Fig. **??**, as measured by the Greenland Climate Network [Box, 1999]. The wind barbs direction of wind flow is from the tip to the base.

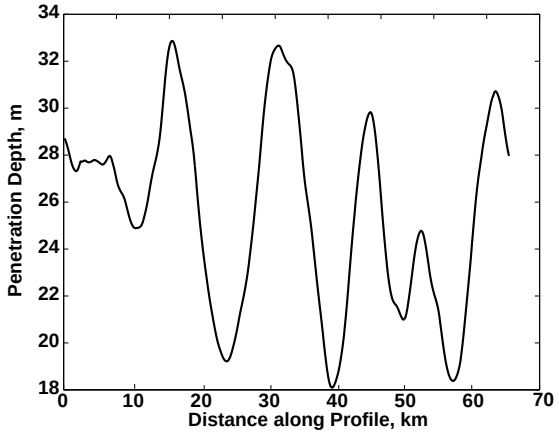

Figure 6.6: Penetration depth along the profile of Fig. 6.2, as calculated from the correlation.

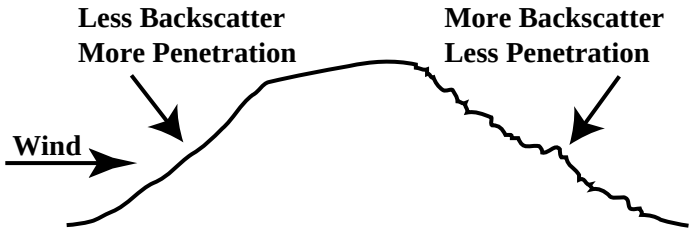

Figure 6.7: Topographic undulations and the radar signal

The interaction between the winds and these slight topographic undulations can produce large (40%-60%) variations in the accumulation rate [Sohn et al., 1999; van der Veen et al., 1999; Steffen et al., 1999; Munk et al., 2001]. Accumulation differences can alter the structure in several ways; we examine two cases in Secs. 6.4 and 6.6.

6.4 Snow-grain scattering

As explained in Chap. 2, snow-grain scattering has been proposed by others as the dominant scattering mechanism for C-band SAR observations of the dry snow zone, and variations in mean grain size as the cause of spatial backscatter fluctuations [Jezek, 1993; Partington, 1989; Forster, 1999; Munk et al., 2001]. As detailed in Chap. 2, the mean grain size can be translated into accumulation rates. Because snow grains are small compared to the wavelength, the scattering from the grains will follow a Rayleigh relationship. For simplicity, snow scattering models usually include the assumption that each snow grain is a sphere. For a volume of uniform spheres, each having (real) relative permittivity ϵ_i and radius r_g, embedded in a background of air, the classical expression for the scattering coefficient is [Matzler, 1998]:

$$\kappa_s = 2\, v_f\, k_0^4\, r_g^3 \left(\frac{\epsilon_i - 1}{\epsilon_i + 2}\right)^2, \tag{6.5}$$

where $k_0 = \frac{2\pi}{\lambda_0}$ is the free-space wavenumber and v_f is the *volume fraction* of the firn, that is,

$$v_f = \frac{\rho_f}{\rho_i}. \tag{6.6}$$

Here ρ_f is the density of the firn and ρ_i is the density of ice ($0.917\ g\,cm^{-3}$). Due the r_g^3 dependence in Eqn. 6.5, the scattering coefficient is very sensitive to changes in grain size. Thus factors of two in the return power could be achieved with variations in grain size of about 25%, although, as we can see by the curve in Fig. 6.4, this sensitivity diminishes as the grain size increases.

As we can see by the volume fraction dependence in Eqn. 6.5, the scattering coefficient increases with increasing density. If we consider the snow grains as a "cloud" of non-interacting spheres, then the increase in κ_s with number density makes sense. However, as the densities approach that of pure ice, we would expect that the scattering would die off, since the medium becomes more homogeneous. For an idealized solid block of ice there should be zero return echo from the volume. Thus the classical model fails to predict κ_s as $v_f \rightarrow 1$.

In fact, even at common firn densities, the snow grains are close enough together that the classical model is not realistic [Tsang et al., 1985]. The classical model has been improved upon by more rigorous dense medium radiative transfer (DMRT) models, including a solution for a homogeneous medium of spheres [Tsang et al., 1985], for spheres having a distribution of permittivities and sizes [Ding and Tsang, 1989] and for "sticky" spheres [Shih et al., 1997].

These models account for the interaction of the scattered fields $\vec{E_s}$ from neighboring grains, i.e., the scatterers can no longer be considered independent:

$$\langle \vec{E_{s,i}} \vec{E^*_{s,j}} \rangle_{i \neq j} \neq 0, \tag{6.7}$$

resulting in an added factor in the expression for the scattering coefficient. In the case of model developed by Tsang et al. [1985] for scattering from a dense medium of same-size and same-permittivity spheres, the new κ_s in the low-frequency (Rayleigh) limit is

$$\kappa_{s,Tsang} = \kappa_{s,Classical} \frac{(1-v_f)^4(\epsilon_i+2)^2}{9\,(1+2\,v_f)^2\,\left[1+\frac{(1-v_f)\,(\epsilon_i-1)}{3\,\epsilon}\right]^2}. \tag{6.8}$$

where ϵ is the effective permittivity of the firn, as discussed in Chap. 5.

On account of the $1-v_f$ factor in Eqn. 6.8, the scattering coefficient dies out as v_f goes to 1. Also, as v_f approaches zero, $\epsilon \rightarrow 1$ and $\kappa_{s,Tsang}$ is reduced to $\kappa_{s,Classical}$, as we would expect.

The introduction of a distribution of sphere sizes about a mean size into the DMRT model tends to increase the theoretical backscatter coefficient, since Rayleigh scattering will disproportionately favor larger grain sizes [Ding and Tsang, 1989; Shi et al., 1993]. Thus the *effective* grain size, that is, the grain size as measured by radar, will be larger than the mean grain size. Moreover, more complicated models involving "sticky" spheres tend to increase the effective or radar-measured grain size as clumps of spheres will act as one larger sphere [Shih et al., 1997]. These additions to the DMRT model, however, do not decrease the dependence of κ_s on density.

Because of the mathematical complexity of the DMRT models and the lack of success in matching DMRT theoretical results with real-world backscatter data [West et al., 1993; Kendra et al., 1998], several authors have proposed modified classical models that include dense-medium aspects [Matzler, 1998; Kendra et al., 1999; Forster, 1999]. For instance, Matzler [1998] derived a scattering coefficient for volume scatter from sphere-shaped snow grains using a modified Born approximation:

$$\kappa_{s,Matzler} = \kappa_{s_{Classical}}(1-v_f)\left[\frac{2\,\epsilon+1)\,(\epsilon_i+2)}{3\,(2\,\epsilon+\epsilon_i)}\right]^2. \tag{6.9}$$

As was the case with $\kappa_{s,Tsang}$, $\kappa_{s,Matzler}$ falls to zero as v_f approaches 1, and conversely as $v_f \rightarrow 0$ the scattering coefficient in Eqn. 6.9 approaches the classical result.

In Fig. 6.8(a) we plot the expected normalized radar cross section as a function of grain size, for the three models above. In calculating the curves in Fig. 6.8 (a) we assumed an isotropic half-space with single size and same permittivity spheres. The volume fraction was

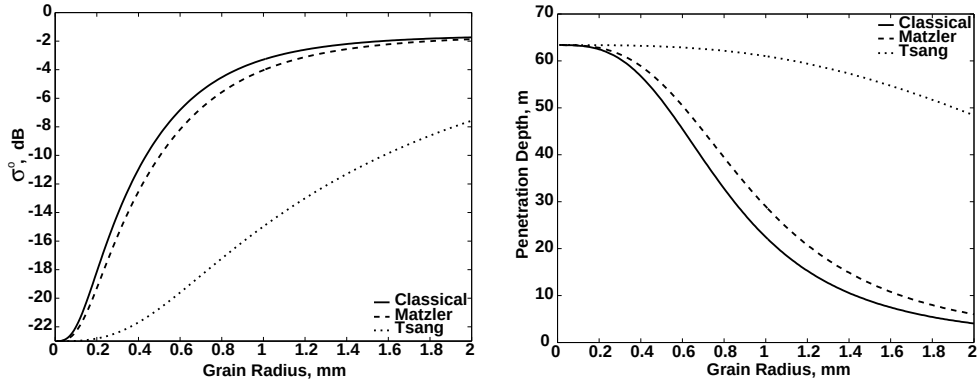

(a) (b)

Figure 6.8: Power (a) and penetration depth (b) as a function of grain size for three different scattering models, as discussed in the text. The classical model gives the highest return power but is physically implausible, the model by [Matzler, 1998] shows slightly less return, while the model by Tsang et al. [1985] has dramatically less backscattered power. The reason for these differences is due to the dependence on firn density.

assumed to be 0.5. We used ERS nominal wavelength (5.67 cm), incidence angle (23°), and included the nominal noise equivalent, σ^0_{noise}, of the ERS system (-23 dB) in our calculation. The absorption coefficient, κ_a, was calculated as [Rott et al., 1993]:

$$\kappa_a = \frac{k\,\epsilon''}{\sqrt{\epsilon}}, \tag{6.10}$$

where ϵ'' is the imaginary term of the firn permittivity, which, at C-band, is given by the empirical mixing formula developed by Matzler [1987]:

$$\epsilon'' = \epsilon''_i\,(0.52\,\rho_{firn} + 0.62\,\rho^2_{firn}). \tag{6.11}$$

Here ρ_{firn} is the firn density and $\epsilon''_i = 0.00033$ is the imaginary part of the dielectric constant of pure ice at C-band and a typical firn temperature of $-15°$ C [Matzler, 1987]. For a volume fraction of 0.5, ϵ'' is approximately 1.0×10^{-4}.

It is apparent in Fig. 6.8(a) that the model by [Tsang et al., 1985] underestimates the

return power we find in our ERS data (Fig. 6.2) for typical grain sizes, as grain radii of even 2 mm would be considered extremely large [Benson, 1962]. Both West et al. [1993] and Kendra et al. [1998] found a similar underestimation of the DMRT model for radar data from snow. On the other hand, the classical model and the modified Born model of Matzler [1998] show a range of return powers consistent with Fig. 6.2 for reasonable grain sizes.

In (b) of Fig. 6.8 we plot the penetration depth as calculated by $d = \kappa_e^{-1}$. We see that the classical and the modified Born model give a range of penetration depths that is consistent with the penetration depth profile shown in Fig. 6.6, whereas the DMRT model, because of the density factor in $\kappa_{s,Tsang}$, fails to accurately predict the penetration of the radar signal for typical grain sizes. The reason why there is a finite penetration depth at zero grain radius is due to absorption.

As was discussed in Chap. 2, a medium with constant density and permittivity is not realistic for the Greenland firn, as the density and permittivity increase with depth. Therefore we extend our model to include this aspect, where we consider the firn to be a layered medium, in which each layer of spheres has a constant density. The signals from the layers are added incoherently [Ulaby et al., 1981]:

$$\sigma^0 = \sum_{n=1}^{\infty} \frac{3\,\kappa_s(n)\,h}{2} \exp\left(-2\,h \sum_{m=1}^{n} \frac{\kappa_e(m)}{\cos\theta_r(m)}\right) \tag{6.12}$$

where h is the layer thickness, assumed constant. Below the layer size where sampling issues affect the result, the choice of h makes little different to the overall result. Also, for the time being, we neglect any backscatter from the layer interfaces. The density is assumed to follow the profile parameterized in Fig. 2.4, such that κ_s, κ_a, and θ_r are all functions of the layer indices n and m.

Since almost all of the parameters in Eqn. 6.12 are functions of depth, derivation of penetration depths is more complicated than simply calculating $1/\kappa_e$. This leads to an important point: even though the extinction coefficient κ_e may decrease as a function of depth, thus leading to greater transparency of the medium at depth to the radiowave, the backscattering coefficient σ_v also decreases, leading to a diminished signal at greater depths. In general, in interpreting radar data without any *a priori* information, we have

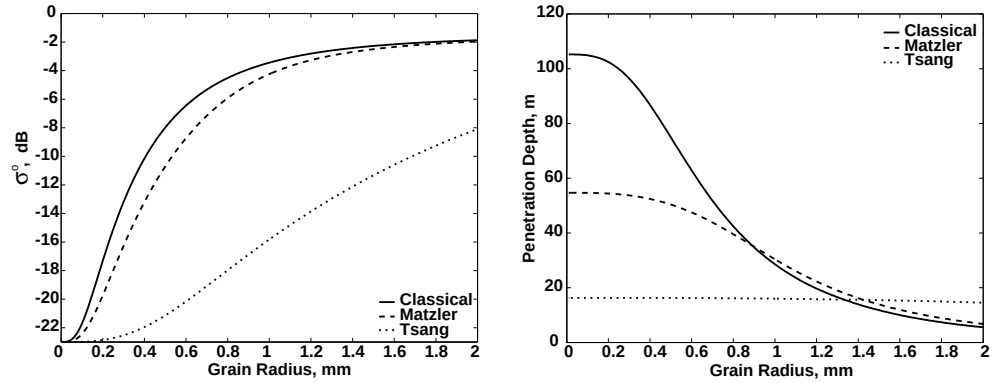

(a) (b)

Figure 6.9: Power (a) and penetration depth (b) as a function of grain size for three different scattering models, where we have included the increase of density with depth. There are only slight differences between the (a) and constant-density result in Fig. 6.8(a). The penetration depth curves in (b) are remarkably different than those in Fig. 6.8(b), due to the dependence of κ_s on density.

no means to determine if the echoes are diminishing due to losses in the medium or due to a reduction of the backscattering efficiencies of the scatterers. Since the penetration depth d that we measure by the correlation is derived from radar signals, as opposed to one-way transmission, we calculate the penetration depth by finding the depth at which the return echo is e^{-2} down from the echo of the topmost layer.

In Fig. 6.9(a) and (b) we plot σ^0 and penetration depth values, respectively, for an increasing-density firn, as a function of grain size. There are only slight differences between the backscatter power (a) and the constant-density result in Fig. 6.8 (a). The penetration depth curves, however, are remarkably different. The differences can be explained by the κ_s of each respective model dependence on firn density. At small grain sizes the scattering coefficient is small, and the κ_e is dominated by the absorption coefficient. However, the backscatter efficiency is now a function of depth, so that the perceived penetration depth, as compared to the penetration in the constant density case of Fig. 6.8(b), increases for the classical model (since $\kappa_{s,Classical}$ increases as a function of depth), decreases slightly for the modified Born model of Matzler [1998] (due to the $(1 - v_f)$ dependence in $\kappa_{s,Matzler}$), and decreases strongly for the DMRT model of Tsang et al. [1985] (due to the $(1 - v_f)^4$ dependence in $\kappa_{s,Tsang}$.) In fact, the penetration depth as predicted by the DMRT model

is completely determined by the decrease in backscatter as a function of depth, so the penetration depth shows only a slight decrease as the grain size increases.

The backscatter coefficient as a function of depth can be translated directly into volume correlation by a discretized version of Eqn. 5.3:

$$\rho_{volume} = \left| \frac{\sum_{n=1}^{\infty} \sigma_v(n) h \exp\left(j \frac{4\pi}{\lambda} h \sum_{m=1}^{n} \frac{\sqrt{\epsilon(m)}\, \delta\theta_r(m)}{\sin\theta_r(m)} \right)}{\sum_{n=1}^{\infty} \sigma_v(n) h} \right| \tag{6.13}$$

where

$$\sigma_v(n) = \frac{3\,\kappa_s(n)\,h}{2} \exp\left(-2\,h \sum_{m=1}^{n} \frac{\kappa_e(m)}{\cos\theta_r(m)} \right) \tag{6.14}$$

We plot in Fig. 6.10 the theoretical volume correlation as a function of grain size, for the increasing-density medium described above. The correlation predicted in the Tsang et al. [1985] model is high (> 0.7) and shows little variation (± 0.03) over grain size variations since, in the model, the radar signal is constrained near the surface. On the other hand, the other two models show a much greater degree of variation of correlation, consistent with the InSAR coreelation data.

The DMRT model predicts less backscatter *and* volume decorrelation than we see in the radar data, and poorly explains the observed power and correlation fluctuations. The classical model is limited in that it has no allowances for a medium that approaches ice. The model by Matzler [1998] predicts backscattered power that ranges from the ERS noise floor to -4 dB, and correlation variation from 0.3 to 0.9, all within a plausible grain size range. However, when we combine the power and correlation data in Fig. 6.11, we see that the model of Matzler [1998] fails to explain the *combined* ERS power and correlation data. The only way for the model curve in Fig. 6.11 to match the data is to adjust ϵ'' term for each point, which, raises or lowers the "leveling off" point in Fig. 6.11. Such an variation in the imaginary permittivity would imply factors of two fluctuations or more over a few kilometers, which is unlikely.

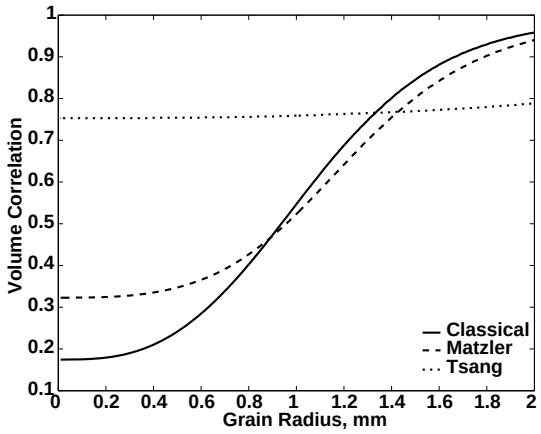

Figure 6.10: Volume correlation as a function of grain size for three different snow grain scattering models. The DMRT model [Tsang et al., 1985] predicts scattering constrained near the surface, and thus there is little variation in volume correlation. The classical model and the modified Born model show a large degree of correlation variation, consistent with the InSAR data.

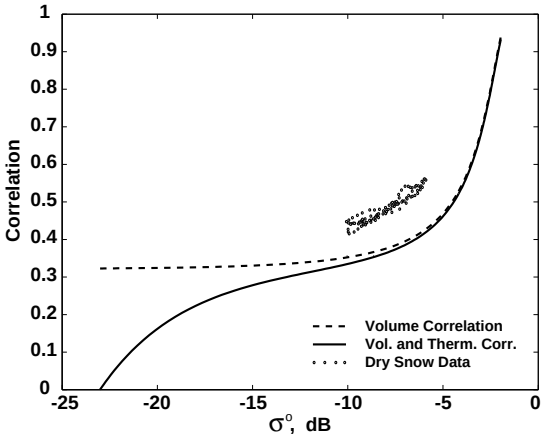

Figure 6.11: Volume correlation vs. power, as predicted by Matzler [1998], plotted with ERS data from the dry snow zone. We see that, while the *range* of power and correlation variations can be explained by the snow-grain model, the model is not able to simultaneously explain the power and correlation data.

Thus it appears, based on our combined modeling of the return power and volume correlation, that models including grain-scattering effects alone fail to predict the behavior observed in ERS InSAR data from the interior of Greenland. This has important implications, since there has been at least one study [Forster, 1999], in which a C-band snow grain scattering model was invoked to estimate accumulation rates from ERS power data. If our reasoning is correct, then application of a snow-grain model to explain C-band dry snow zone data is in error. There is further evidence to corroborate our finding as detailed in Sec. 6.5.

6.5 Evidence C-band Scattering from Buried Layers

There are several additional lines of reasoning that suggest that grains are not the dominant scatterers in the dry snow zone at C-band. The first follows from laser altimetry data, courtesy of W. Krabill at GSFC-NASA. Numerous tracks flown over the Greenland ice sheet in the summers of 1994 and 1995 by the Airborne Topographic Mapper (ATM) yield surface height data using an on-board laser altimeter. A single height datum is determined by scanning the laser over an approximately 20 x 20 m area on the ground, where approximately 1000 pixels are averaged to find a mean height value, which, depending on the terrain, has an absolute accuracy of a few centimeters. As the aircraft moves along, a height profile is thus recorded. Also recorded is an RMS height profile, based on the abovementioned averaging over individual scan planes. The RMS height value is indicative of the surface roughness, as terrain with a greater dispersion of heights over the 20 meter-square window will have a larger RMS height value. The ATM RMS height is measured in centimeters, and thus small-scale effects such as changing grain sizes will not be evidenced in the data. Furthermore, the laser does not interact with the sub-surface, so that grain growth is not a factor in interpreting the ATM data.

In Fig. 6.12 we plot both RMS height variation and elevation as a function of distance along a profile, where the profile flight track is the same as for the profile shown in Fig. 6.2. Just as the power and correlation were maximum on the lee side of the hill, the roughness shown in Fig. 6.12 likewise increases on the lee side of the hill. While it is difficult to extract exact roughness parameters from the laser RMS height value, this plot does indicate that

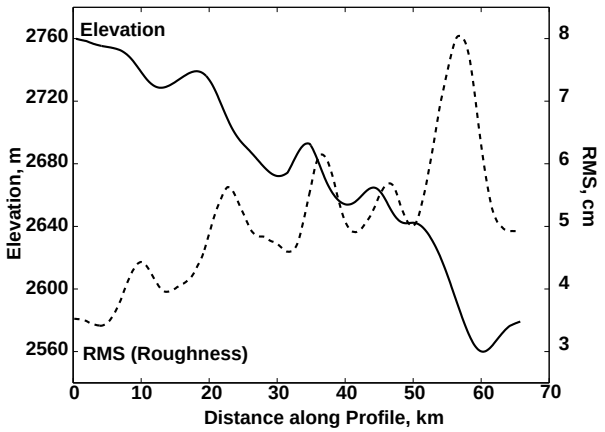

Figure 6.12: ATM laser altimeter RMS variations plotted with surface elevation for the same flight track in Fig. 6.2. The RMS height value is a measure of the roughness of the terrain.

structures larger than snow grains affect the backscatter over these topographic undulations.

Even in areas devoid of topographic variation, there is reason to suspect that grains are not the dominant scatterers. For diffuse volume scatter where σ_v is not a function of incidence angle, the fall-off of σ^0 with incidence angle is as $\cos\theta_r$, as found in the derivation of Eqn. 6.3 for snow grain scatter. Satellite scatterometry data over the dry snow zones of the polar ice sheets, however, show a comparatively rapid fall-off of σ^0 with increasing θ; for example, Rott et al. [1993] and Rott and Rack [1995] found that over the incidence angles $\theta = 20^\circ - 60^\circ$ σ^0 decreased by 10 dB or more. Diffuse volume scatter, on the other hand, would decrease by less than 3 dB over the same angles. Even over the the ERS swath width a sharper drop-off is found than would be expected from diffuse volume scatter, as shown in Fig. 6.13. Here we plot the calibrated ERS dry snow zone σ^0 data from near range to far range, ERS scatterometry data over similar terrain in Antarctica [Rott et al., 1993], and results from two different scattering model: diffuse volume scatter, discussed above, and rough surfaces, which we calculate using the small perturbation method (SPM) for single-scattering from a slightly rough surface [Ulaby et al., 1981]. We will discuss our modeling of rough surface scattering in Sec. 6.6.

Clearly the dry-snow firn does not scatter solely like a diffuse volume. Our ERS SAR results are similar in form to ERS scatterometry, both of which are better represented by

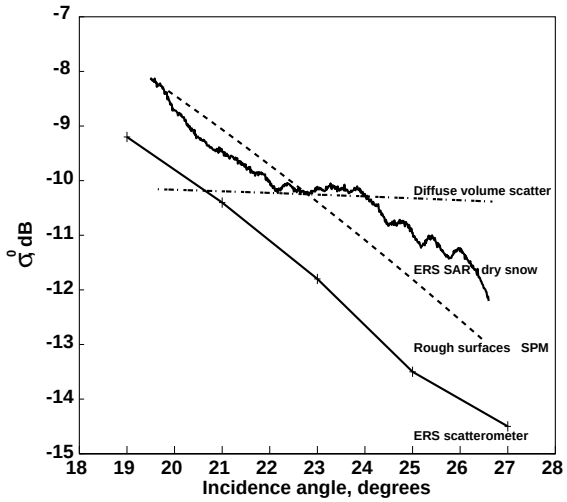

Figure 6.13: σ^0 vs. incidence angle over the ERS swath. Also plotted are ERS scatterometry data from Antarctica [Rott et al., 1993], and two models: diffuse volume scatter and rough surfaces scatter.

a rough surface scattering model. We note that even though the firn does not scatter like a diffuse volume, this does not imply that all the return echo results from scatter from the air-ice interface. On the contrary, we have shown in Chap. 5 that there are scatterers at depth contributing to the return echo. What Fig. 6.12 and Fig. 6.13 do imply, however, is that interfaces, including both surface and buried, are the most dominant form of C-band scatterer in the dry snow zone, rather than the grains. These results are corroborated by DMRT modeling of Antarctic microwave emission data by West et al. [1994], who concluded that at 37 GHz (0.8 cm) microwave emission of polar firn is dominated by snow grain scattering, while at 6.6 GHz (4.5 cm), i.e., C-band, it is dominated by layered scattering.

6.6 Layering

For demonstrative purposes we model the scattering from an infinite series of rough interfaces in the Greenland firn, as depicted in Fig. 6.14. For simplicity, we restrict our model to the single-scattering case, thus neglecting any multiple scattering or coherent effects such as "resonances" between layers, since the separation between interfaces is assumed to be

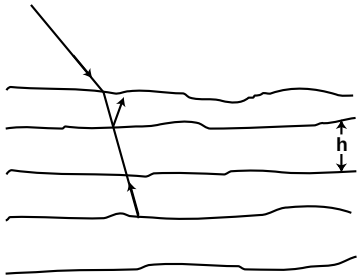

Figure 6.14: Layered scattering.

several wavelengths in width. Also, we assume that the layers are planar with mm-scale roughness characteristics. Of course more rigorous models do exist; see Zuniga et al. [1979]; Tsang et al. [1985]; Karam and Fung [1986]; Shih et al. [1997]; Fung [1994]. We understand that the simplifications in our modeling may omit important scattering aspects, however, our goal is to show that power and correlation may be used to determine mean annual snow layer widths.

We consider first a single slightly rough interface between two different dielectric mediums. Here we make use of the first-order SPM result from Ulaby et al. [1981] for VV polarization scattering from a rough surface:

$$\sigma^0_{layer} = 8\, k_i\, \sigma_l^2\, \cos^4\theta\, |\alpha_{vv}|^2\, W(2\, k\, \sin\theta), \tag{6.15}$$

where k_i is the wavenumber in the incident medium, σ_l^2 is variance of the surface (assuming a Gaussian height distribution), θ is the incidence angle, α_{vv} is the VV *polarization amplitude*:

$$\alpha_{vv} = (\epsilon_r\ - 1)\, \frac{\sin^2\theta\ - \epsilon_r\ \left(1\ +\ \sin^2\theta\right)}{\left[\epsilon_r\, \cos\theta\ +\ \sqrt{\epsilon_r\ -\ \sin^2\theta}\right]^2}, \tag{6.16}$$

Here ϵ_r is the ratio of permittivities between the mediums at the interface forming the rough surface, with $\epsilon_r\ =\ \epsilon(below)/\epsilon(above)$. Continuing with Eqn. 6.15, W is the Fourier transform of the interface autocorrelation function, which we assume to be Gaussian:

$$W(2\,k\,\sin\theta) = \frac{1}{2}\,l^2 \exp\left[-(k\,l\,\sin\theta)^2\right], \tag{6.17}$$

and l is the horizontal correlation length of the surface.

In adopting a rough-layer model, even the simple one here, we now have several more free parameters than in the snow-grain scattering case. Namely, the roughness σ_l^2, the correlation length l, and the density contrast between layers ϵ_r, are all terrain-dependent parameters that affect $\sigma^0_{vv,layer}$.

Considering the air-ice interface for the moment, we use ERS parameters and the *in situ* findings of Long and Drinkwater [1994] (σ_l of 5 mm, l of 5 cm, and ϵ_r of 1.6), which are typical for the dry snow zone [Forster, 1999], to calculate a $\sigma^0_{vv,layer}$ of -30 dB. In the dry snow zone, typical values of σ^0 range from about -4 to -15 dB. Obviously, the InSAR power images can not be explained by the surface scatter-only case.

Instead of just the top layer, suppose that the radiowave interacts with a series of rough interfaces, each contributing to the return echo. As can be seen in Fig. 2.6, the summer hoar layers not only indicate the annual accumulation but also provide a high degree of dielectric contrast from the surrounding medium. Thus we characterize the firn as a series of evenly-spaced rough hoar layers, with spacing h, having thicknesses t_l, dielectric contrast ϵ_r from the surrounding medium, RMS roughness σ_l, and horizontal correlation length l.

There will be losses associated with propagation in the medium, which we separate into two different factors: absorption losses and losses from non-backscattered reflections from the interfaces. The absorption losses are quantified by an exponential loss coefficient as discussed in previous chapters, with the extinction coefficient determined by absorption losses only: $\kappa_e = \kappa_a$. The absorption coefficient is calculated from ϵ'' in Eqn. 6.10. The reflection losses are quantified by the transmission coefficient for a rough interface [Ulaby et al., 1981]:

$$\gamma = \gamma_{Fresnel} \cdot \exp(-\bar{q}_z\,\sigma_l^2/2) \tag{6.18}$$

where $\gamma_{Fresnel}$ is the oblique Fresnel power transmission coefficient for parallel polarization incident on a plane boundary of a slab of thickness t_l, and $\bar{q}_z = k_1 \cos\theta_1 - k_2 \cos\theta_2$, with the indices 1 and 2 referring to the incident and transmitted mediums, respectively.

We calculate the theoretical σ^0 of the firn by incoherently adding the returns from individual rough interfaces:

$$\sigma^0 = \sum_{n=1}^{\infty} \sigma^0_{vv,layer} \exp\left(-2\,n\,h\,\frac{\kappa_a}{\cos\theta_r}\right) \prod_1^n \gamma_n^2(\theta_r). \tag{6.19}$$

From Eqn. 5.3, the volume correlation is

$$\rho_{volume} = \left| \frac{\sum_{n=1}^{\infty} \sigma^0_{layer} \exp\left(-2\,n\,h\,\frac{\kappa_a}{\cos\theta_r}\right) \prod_1^n \gamma_n^2(\theta_r) \exp\left(j\frac{4\pi n h\sqrt{\epsilon}\,\delta\theta_r}{\lambda \sin\theta_r}\right)}{\sigma^0} \right|. \tag{6.20}$$

Layered scattering acts similarly to grain scattering, in that brighter returns correspond to shallower penetration depths. Layers that are rougher, closer together, or that have a larger dielectric contrast from one another will result in stronger return echoes but with less wave penetration. Conversely, when the layers are smoother, or spaced farther apart, or do not have much dielectric contrast, then there will be little scattering to impede the propagation of the wavefront, resulting in decreased return echo power and larger penetration depths.

There are a number of unknowns in this model. In an effort to reduce the number of possible variables we assume that both the correlation length l and thickness t_l are constant, with values of 5 cm [Long and Drinkwater, 1994] and 2 cm (the resolution of the profile shown in Fig. 2.6), respectively. Furthermore, Rott et al. [1993] found that in regions of lower accumulation the dielectric contrast of the interfaces was greater, compared to areas of higher accumulation. Also, in low accumulation areas each layer is exposed for a longer period of time before being buried, therefore climate-induced roughness mechanisms have a longer time in which to act. Of course, layer spacings are smaller in low accumulation areas. Therefore it is reasonable to suspect that accumulation rates, in the form of layer spacings, are inversely related to both the roughness of the interfaces and the dielectric

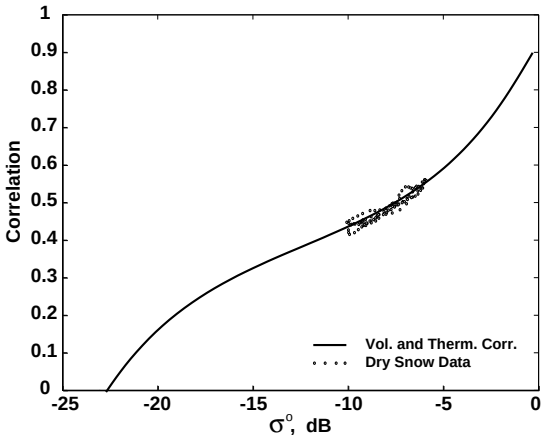

Figure 6.15: Modeled correlation (volume × thermal) vs. power for a layered medium (black line), with ERS InSAR data (small circles.)

contrast between layers. We parameterize the dependence of σ_l and ϵ_r on h as linear:

$$\sigma_l = -h\,\alpha_l + \beta_l, \tag{6.21}$$

and

$$\epsilon_r = h\,\alpha_r + \beta_r, \tag{6.22}$$

where α_l, β_l, α_r, β_r are constants, and ϵ_r is less than one, as the hoar layers are less dense than the surrounding firn.

In Fig. 6.15 we plot correlation vs. power (σ^0) for our rough layers model, with ERS InSAR data. We have adjusted the parameters α_l, β_l, α_r, β_r to fit the data using least-squares methods. Over the range of the ERS data shown in Fig. 6.15, h varies from 12 to 17 cm, σ_l from 3.5 to 2.0 mm, and ϵ_r from 0.88 to 0.91, all of which are physically plausible.

The plots of power and volume correlation as a function of layer width for the fitted constants are found in Fig. 6.16(a) and (b), respectively. As the spacing width increases

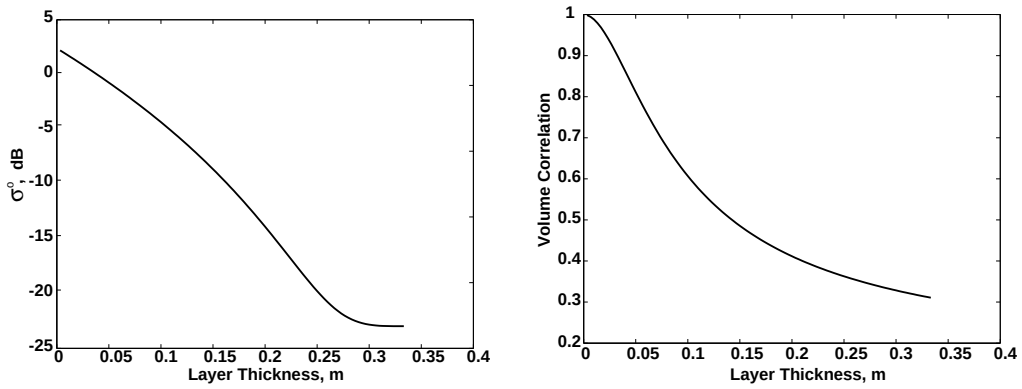

(a) (b)

Figure 6.16: Power (a) and volume correlation (b) for a layered medium with increasing layer widths. As expected, power and correlation fall off as layer width increases.

the return power falls off, since the radar signal is forced to travel longer distances before encountering a scatterer, while at the same time the correlation drops, since scatterers are spread more in the vertical direction.

We use the curve in Fig. 6.15(a) to interpolate layer spacing values from the power image in Fig. 6.2(b). The layer spacing map is shown in Fig. 6.17. Considering a direct proportionality between hoar layer spacing and accumulation rate, we see up to a 40% variation along the ice stream undulations, consistent with similar topography-dependent accumulation rate variations in found by *in situ* methods [Sohn et al., 1999; van der Veen et al., 1999; Steffen et al., 1999; Munk et al., 2001].

6.7 Conclusion

In Chap. 3 we use a simple volume scattering model to describe the return power, quantified by σ^0, in terms of the properties of the terrain. In Chap. 4, we applied this simple volume scatter model to derive an expression for spatial decorrelation that includes volume scatter. Other than a few terrain-dependent assumptions, such as many scatterers within each resolution element, correlation lengths between scatterers small compared to the size of the resolution element, and an exponential fall-off due to propagation in the medium, we have

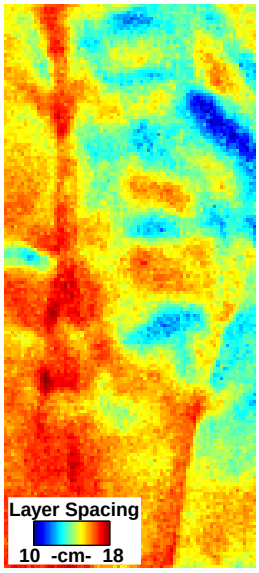

Figure 6.17: A map of annual hoar layer spacing, derived from rough interface modeling and the power image in Fig. 6.2(b).

not introduced into the model the particulars of C-band scattering from dry polar firn. To rectify this, in this chapter we examined two cases: Rayleigh scattering from snow grains, and rough surface scattering from buried interfaces. The motivation for adding realistic scattering situations into the model is to derive accumulation rates, since the structure of the firn will be determined by the local climate conditions. Both of the structural cases analyzed here, snow grains and layers, are sensitive to the amount of snow that is deposited each year.

We find that none of grain-scattering models we analyze can explain the ERS power and correlation data. Moreover, there is ancillary radar and laser altimetry data to support this finding. The simple layered model that we introduce here, however, is able to match both the power and correlation data, and seems to give a plausible explanation to the ancillary data.

One of the omissions of the layered model are structures that are correlated on a scale greater than a wavelength. The laser data shown in Fig. 6.12 indicates that such large-scale surface structures are present, which could also explain the increase in backscatter on the

lee sides of hills. Furthermore, radiometer, scatterometer, and SAR data taken at different azimuth angles, that is, the pointing angle of the antenna relative to north, indicates that there is a preferred azimuth orientation to passive/active radar measurements of polar firn [Rott et al., 1993; Sohn et al., 1999; Long and Drinkwater, 2000], which is also indicative of "corrugations". Rott et al. [1993] suggested that buried *sastrugi* (meter-scale surface undulations) are the cause of the azimuthal variations. A more complete layered scattering model should include these structural aspects.

Chapter 7

Conclusion

The icy polar regions, which play an important role in the global climate, can be analyzed from afar on a continental scale and with regularity using radar remote sensing. In this dissertation, we introduce a new technique in analyzing interferometric radar remote sensing data of polar firn, namely, the measurement of spatial decorrelation due to volume scatter.

7.1 Contributions

These data yield information about the depth of penetration of C-band radar signals into the polar firn, as well as the suitability of various scattering models that relate the radar echoes to accumulation rates. Our specific contributions are:

1. An extended surface correlation model including dielectric volume scattering. The model assumes very little about the scattering medium and thus is applicable to a wide range of volume scattering regimes. In a special case, we apply the model to a lossy medium, in order to compute penetration depths.

2. Penetration depth maps of Greenland firn using decorrelation model. Due to the wide coverage and fine resolution afforded by the ERS satellites we are able to create high resolution penetration maps that include all of the different facies of the ice sheet. As expected, we find minimal penetration depths on the rocky coast, but around 20-30 m in the icy interior.

3. Observations and models of the leeward/windward side differences in backscatter and correlation in the dry snow zone. We found that the lee side of topographic undulations show brighter returns and less depth of penetration, indicative of a decrease in snow accumulation on the lee side.

4. Correlation and power analyses constraining models to estimate accumulation rates. Using both correlation and power data we find that grain-scattering models fail to explain the InSAR data, while a layered scattering model provides a better match. Using a layered scattering model we estimate an approximate 40% variation in snow accumulation along Greenland ice sheet topographic undulations.

7.2 Future Work

As with any body of scientific work, the research included in this dissertation is not complete. Future InSAR spatial correlation research of the ice sheets would best concentrate on three main areas:

1. Refinement of temporal correlation determination. While we determine $\rho_{temporal}$ here, our temporal baselines are limited to less than 10 days. Interferograms depicting the polar ice caps have been produced with several months to a year temporal separation between observations. Obviously, with a greater range of T, we can more accurately determine the temporal component of the decorrelation.

Furthermore, there are various airborne and spaceborne sensors, such as TOPSAR or SRTM, which acquire InSAR data simultaneously, allowing a more direct measurement of $\rho_{spatial}$. Typically single-pass interferometers have a baseline that, due to mechanical constraints, is only a small fraction of the critical baseline, implying that only a slight amount of spatial decorrelation would be seen in the data. However, since $\rho_{temporal}$ is unity for these measurements, then determining the spatial decorrelation, however small it may be, becomes much easier. Neither SRTM or TOPSAR have observed the ice sheets, though there are certainly temperate glaciers data that are included in their dataset. While determining accumulation rates would be very difficult for the complex scattering medium presented by temperate glaciers, penetration depth information could be determined, which would aid in the refinement of the technique.

2. Improvement of scattering models. As we show, the radiowave scattering medium comprised by the polar firn is complex. Our modeling approaches have used various simplifying assumptions to make the problem tractable. More rigorous solutions, such as DMRT methods for a hybrid layer/grain scattering, would require fewer assumptions. Furthermore,

one aspect that we have not included in our modeling is coherent additions of echoes from periodicities in the firn structure. As discussed in Chap. 6, such a model would help account for the azimuthal anisotropy seen in various radiowave data from polar firn. None of the simple models we use in this dissertation can account for azimuthal variations.

3. Inclusion of other remote-sensing data. In Chap. 6 we presented laser altimetry data acquired over the same terrain as the InSAR data. A more complete description of the polar firn could be attained by including co-registered scatterometry, radiometry, and additional optical data. While sensors different than the SAR platform on-board the ERS satellite will be sensitive to other aspects of the firn, based on frequency, polarization, and incidence angle, a more comprehensive model would be able to explain all forms of data. More comprehensive and wavelength diverse input data at hand should lead to a more accurate determination of accumulation rates, or other important mass balance variables.

Appendix A

Correlation Lengths

We can derive the relationship expressed in Eqn. 3.20 more formally by considering that f represents a random process that is indexed by the position (x, y, z). Then [Leon-Garcia, 1994]

$$\langle f(x,y,z) f^*(x',' y', z') \rangle = \iint f f'^* p_{f,f'}(f,f') df\, df', \tag{A.1}$$

where $p_{f,f'}$ is the joint pdf of $f(x,y,z)$ and $f(x',y',z')$, and the integrals are over possible realizations. A white reflectivity function implies that from scatterer to scatterer the phase of f is random and uniformly distributed from 0 to 2π. This also implies that the pdfs of neighboring scatterers are uncorrelated. Thus when $(x,y,z) \neq (x',y',z')$,

$$p_{f,f'^*}(f,f'^*) = p_f(f) p_{f'^*}(f'^*), \tag{A.2}$$

and

$$\langle f(x,y,z) f^*(x',' y', z') \rangle = \int f p_f(f) df \int f'^* p_{f'}(f') df', \tag{A.3}$$

which is simply $\langle f(x,y,z) \rangle \cdot \langle f^*(x',' y', z') \rangle$. Since the phase is uniformly distributed, f is a zero-mean process. Then

$$\langle f(x,y,z)f^*(x','y',z')\rangle = 0. \tag{A.4}$$

When $(x,y,z) = (x',y',z')$, then

$$p_{f,f'^*}(f,f'^*) = p_f(f), \tag{A.5}$$

and

$$\langle f(x,y,z)f^*(x','y',z')\rangle = \int |f|^2 p_f(f)df. \tag{A.6}$$

Eqn. A.6 is the variance of the reflectivity function, which is equal to the mean backscatter coefficient per unit volume [Curlander and McDonough, 1991]. The 'mean' in this case is over possible realizations, not space, and is in fact still a function of (x,y,z). Therefore

$$\langle f(x,y,z)f^*(x,'y',z')\rangle = \sigma_v(x,y,z)\delta(x-x',y-y',z-z'), \tag{A.7}$$

as in Eqn. 3.20.

Bibliography

Abdalati, W. and Steffen, K. (1998). Accumulation and hoar effects on microwave emission in the greenland ice-sheet dry-snow zones. *Journal of Glaciology*, 44(148):523–531.

Abramowitz, M. and Stegun, I. (1972). *Handbook of Mathematical Functions*. Dover, New York.

Alley, R. B. (1990). Summertime formation of depth hoar in central greenland. *Geophysical Research Letters*, 17(13):2393–2396.

Amelung, F., Oppenheimer, C., Segall, P., and Zebker, H. (2000). Ground deformation near Gade 'Ale Vocano, Afar, observed by radar interferometry. *Geophysical Research Letters*, 27(19):3093–7.

Arthern, R. and Winebrenner, D. (1998). Satellite observations of ice sheet accumulation rate. *IEEE Proceedings of IGARSS*, 4:2249–2251.

Askne, J. I. H., Dammert, P. B. G., Ulander, L. M. H., and Smith, G. (1997). C-band repeat-pass interferometric sar observations of the forest. *IEEE Transactions on Geoscience and Remote Sensing*, 35:25–35.

Bamler, J. (1994). A digital elevation model of the antarctic ice sheet derived from ers-1 altimter data and comparison with terrestrial measurements. *Annals of Glaciology*, 20:48–54.

Bamler, R. and Hartl, P. (1998). Synthetic aperture radar interferometry. *Inverse Problems*, 14:R1–54.

Benson, C. S. (1962). Research report 70: Stratigraphic studies in the snow and firn of the greenland ice sheet. Technical report, SIPRE, U.S. Army Corps of Engineers.

Bindschadler, R. (1998a). Goddard Space Flight Center, private communication.

Bindschadler, R. (1998b). Monitoring ice sheet behavior from space. *Reviews of Geophysics*, 36(1).

Bohren, C. and Huffman, D. (1983). *Absorption and Scattering of Light by Small Particles*. Wiley, New York.

Born, M. and Wolf, E. (1985). *Principles of Optics:Electromagnetic Theory of Propagation,Interference and Diffraction of Light*. Elmsford, New York.

Box, J. (1999). University of Colorado, private communication.

Bracewell, R. N. (1986). *The Fourier Transform and Its Applications*. McGraw-Hill, New York.

Chen, C. W. and Zebker, H. A. (2000). Network approaches to two-dimensional phase unwrapping: intractability and two new algorithms. *Journal of the Optical Society of America A*, 17:401–414.

Curlander, J. C. and McDonough, R. N. (1991). *Synthetic Aperture Radar Systems and Signal Processing*. Wiley, New York.

Dainty, J. C. (1975). *Laser speckle and related phenomena*. Springer-Verlag, Berlin.

Dall, J., Madsen, S., Keller, K., and Forsberg, R. (2001). Topography and penetration of the greenland ice sheet measured with airborne sar interferometry. *Geophysical Research Letters*, 28(9):1703–1706.

Davis, C. and Zwally, J. (1993). Geographic and seasonal variations in the surface properties of the ice sheets by satellite-radar altimetry. *Journal of Glaciology*, 39(133):687–697.

Ding, K. and Tsang, L. (1989). Effective propagations constants in media with densely distributed dielectric particles of multiple sizes and permittivities. *PIER*, 1:241–95.

Ekholm, S. (1996). A full coverage, high-resolution, topographic model of greenland computed from a variety of digital elevation data. *Journal of Geophysical Research*, 101(B10):21961–72.

Ekholm, S., Keller, K., Bamber, J., and Gogineni, S. (1998). Unusual surface morphology from digital elevation models of the greenland ice sheet. *Geophysical Research Letters*, 25(19):3623–26.

Fahnestock, M., Bindschadler, R., Kwok, R., and Jezek, K. (3 December 1993). Greenland Ice Sheet surface properties and ice dynamics from ERS-1 SAR imagery. *Science*, 262.

Fahnestock, M., Scambos, T., Schuman, C., Arthern, R., Winebrenner, D., and Kwok, R. (2000). Snow megadune fields on the east antarctic plateau: extreme atmosphere-ice interaction. *Geophysical Research Letters*, 27(22):3719–22.

Ferretti, A., Ferrucci, F., Prati, C., and Rocca, F. (2000). Sar analysis of building collapse by means of the permanent scatterers technique. *Proceedings of IGARSS 2000*, 7:3219–21.

Forster, R. (1999). Relationships between radar backscatter and accumulation rates on the greenland ice sheet. *International Journal of Remote Sensing*, 20(15):3131–3147.

Fung, A. (1994). *Microwave scattering and emission models and their applications*. Artech House, Boston, MA.

Gabriel, A. K. and Goldstein, R. M. (1988). Crossed orbit interferometry: theory and experimental results from sir-b. *International Journal of Remote Sensing*, 9:857–872.

Gabriel, A. K., Goldstein, R. M., and Zebker, H. A. (1989). Mapping small elevation changes over large areas: differential radar interferometry. *Journal of Geophysical Research*, 94:9183–9191.

Gatelli, F., Guarnieri, A. M., Parizzi, F., Pasquali, P., Prati, C., and Rocca, F. (1994). The wavenumber shift in SAR interferometry. *IEEE Transactions on Geoscience and Remote Sensing*, 32(4):855–864.

Gogineni, P. (1999). U. Kansas, private communication.

Gogineni, P., Legarsky, J., and Thomas, R. (1998). Coherent radar depth sounder measurements over the greenland ice sheet. *IEEE Proceedings of IGARSS*, 4:2258–60.

Goldstein, R. M. (1995). Atmospheric limitations to repeat-track radar interferometry. *Journal of Geophysical Research*, 22:2517–2520.

Goldstein, R. M., Barnett, T. P., and Zebker, H. A. (1989). Remote sensing of ocean current. *Science*, 246:1282–1285.

Goldstein, R. M., Engelhardt, H., Kamb, B., and Frolich, R. M. (1993). Satellite radar interferometry for monitoring ice sheet motion: Application to an Arctic ice stream. *Science*, 262:1525–1530.

Goldstein, R. M. and Zebker, H. A. (1987). Interferometric radar measurement of ocean surface current. *Nature*, 32:707–709.

Goldstein, R. M., Zebker, H. A., and Werner, C. L. (1988). Satellite radar interferometry: two-dimensional phase unwrapping. *Radioscience*, 23:713–720.

Goodman, J. (1999). Stanford University, private communication.

Goodman, J. W. (1985). *Statistical Optics*. Wiley, New York.

Graham, L. C. (1974). Synthetic interferometer radar for topographic mapping. *Proceedings of IEEE*, 62:763–768.

Guarnieri, A. M. and Prati, C. (1997). SAR interferometry: A "quick and dirty" coherence estimator for data browsing. *IEEE Transactions on Geoscience and Remote Sensing*, 35(3):660–669.

Hagberg, J. O. (1994). *Repeat-Pass Satellite SAR Interferometry*. PhD thesis, Chalmers University of Technology.

Hanssen, R. F. (2000). *Radar interferometry: data interpretation and error analysis*. PhD thesis, Delft University of Technology.

Hanssen, R. F., Weckwerth, T. M., Zebker, H. A., and Klees, R. (1999). High-resolution water vapor mapping from interferometric radar measurements. *Science*, 283(5406):1297–9.

Herron, M. and Langway, C. (1980). Firn densification: An empirical model. *Journal of Glaciology*, 25(93):373–385.

Hoen, E. and Zebker, H. (2000). Penetration depths inferred from interferometric volume decorrelation observed over the greenland ice sheet. *IEEE Transactions on Geoscience and Remote Sensing*, 38(6):2571–2583.

Hoen, E. and Zebker, H. (2001). Penetration depths inferred from interferometric volume decorrelation observed over the greenland ice sheet. *IEEE Transactions on Geoscience and Remote Sensing*, 39(1):Erratum.

Ishimaru, A. (1978). *Wave propagation and scattering in random media.* Academic Press, New York.

Jezek, K. (1993). Spatial patterns in backscatter strength across the greenland ice sheet. *Proceedings of the First ERS-1 Symposium, ESA SP-359*, pages 269–272.

Jezek, K., Drinkwater, M., Crawford, J., Bindschadler, R., and Kwok, R. (1993). Analysis of synthetic aperture radar data collected over the southwestern greenland ice sheet. *Journal of Glaciology*, 39(131):119–132.

Jezek, K., Gogineni, P., and Shanableh, M. (1994). Radar measurements of melt zones on the Greenland Ice Sheet. *Geophysical Research Letters*, 21(1):33–36.

Jezek, K., Sohn, H., and Noltimier, N. (1998). The radarsat antarctic mapping project. *IEEE Proceedings of IGARSS*, 5:2462–4.

Joughin, I. (1994). Jet Propulsion Laboratory, Pasadena CA. JPL Meeting: Glaciological Applications of Satellite Radar Interferometry.

Joughin, I. (1995). *Estimation of Ice-Sheet Topography and Motion Using Interferometric Synthetic Aperture Radar.* PhD thesis, University of Washington.

Joughin, I., Gray, L., Bindschadler, R., Price, S., Morse, D., Hulbe, C., Mattar, K., and Werner, C. (1999). Tributaries of west antarctic ice streams revealed by radasat interferometry. *Science*, 286(5438):283–6.

Joughin, I., Kwok, R., and Fahnestock, M. (1996a). Measurement of ice-sheet motion using satellite radar interferometry: method and error analysis with application to humboldt glacier, greenland. *Journal of Glaciology*, 42(142):564–75.

Joughin, I., Kwok, R., and Fahnestock, M. (1998). Interferometric estimation of three-dimensional ice-flow using ascending and descending passes. *IEEE Transactions on Geoscience and Remote Sensing*, 36(1):25–37.

Joughin, I., Winebrenner, D., and Fahnestock, M. (1995). Observations of ice-sheet motion using satellite radar interferometry. *Geophysical Research Letters*, 22(5):571–574.

Joughin, I., Winebrenner, D., Fahnestock, M., Kwok, R., and Krabill, W. (1996b). Measurement of ice-sheet topography using satellite-radar interferometry. *Journal of Glaciology*, 42(140):10–22.

Joughin, I. R. (2000). JPL, private communication.

Joughin, I. R., Fahnestock, M., Ekholm, S., and Kwok, R. (1997). Balance velocities of the Greenland ice sheet. *Geophysical Research Letters*, 24(23):3045–3048.

Joughin, I. R. and Winebrenner, D. P. (1994). Effective number of looks for a multilook interferometric phase distribution. *Proceedings of IGARSS '94*, 4:2276–8.

Karam, M. and Fung, A. (1986). Radiative transfer in multilayered random medium with laminar structure: Green's function approach. *Journal of Applied Physics*, 59(11):3650–3661.

Kendra, J., Sarabandi, K., and Ulaby, F. (1998). Radar measurements of snow: Experiment and analysis. *IEEE Transactions on Geoscience and Remote Sensing*, 36(3):864–79.

Kendra, J., Sarabandi, K., and Ulaby, F. (1999). A hybrid experimental/theoretical scattering model for rense random media. *IEEE Transactions on Geoscience and Remote Sensing*, 37(1):21–35.

Krabill, W., Abdalati, W., Frederick, E., Manizade, S., Martin, C., Sonntag, J., Swift, R., Thomas, R., Wright, W., and Yungel, J. (2000). Greenland ice sheet: High-elevation balance and peripheral thinning. *Science*, 289:428–430.

Kwok, R. and Fahnestock, M. A. (1996). Ice sheet motion and topography from radar interferometry. *IEEE Transactions on Geoscience and Remote Sensing*, 34(1):189–200.

Legresy, B. and Remy, F. (1998). Using the temporal variability of satellite radar altimetric observations to map surface properties of the antarctic ice sheet. *Journal of Glaciology*, 44(147):197–206.

Leon-Garcia, A. (1994). *Probability and Random Processes for Electrical Engineering.* Addison-Wesley, Reading, MA.

Levanon, N. (1988). *Radar Principles.* Wiley, New York.

Long, D. and Drinkwater, M. (2000). Azimuth variation in microwave scatterometer and radiometer data over antarctica. *IEEE Transactions on Geoscience and Remote Sensing*, 38(4):1857–69.

Long, D. G. and Drinkwater, M. (1994). Greenland ice sheet surface properties observed by the the seasat-a scatteromoeter at enhanced resolution. *Journal of Glaciology*, 40(1):213–230.

Lytle, V. and Jezek, K. (1994). Dielectric permittivity and scattering measurements of Greenland firn at 26.5-40 GHz. *IEEE Transactions on Geoscience and Remote Sensing*, 32(2):290–295.

Madsen, S. (1986). *Speckle theory: Modelling, analysis and applications related to synthetic aperture radar.* PhD thesis, Technical University of Denmark.

Madsen, S., Skou, N., Woelders, K., and Granholm, J. (1996). Emisar single pass topographic sar interferometer modes. *IEEE Proceedings of IGARSS*, 1:674–6.

Massonet, D. and Feigl, K. (1998). Radar interferometry and its application to changes in the Earth's surface. *Reviews of Geophysics*, 36(4).

Massonet, D., Rossi, M., Carmona, C., Adragna, F., Peltzer, G., and Feigl, K. (1993). The displacement field of the landers earthquake mapped by radar interferometry. *Nature*, 364:138–142.

Matzler, C. (1987). Applications of the interaction of microwaves with the natural snow cover. *Remote Sensing Reviews*, 2:259–387.

Matzler, C. (1996). Microwave permittivity of dry snow. *IEEE Transactions on Geoscience and Remote Sensing*, 34(2):573–581.

Matzler, C. (1998). Improved born approximation for scattering of radiation in a granular medium. *Journal of Applied Physics*, 83(11):6111–6117.

McDonald, R. (1995). Corona- success ofr space reconaissance, a look into the cold war, and a revolution for intelligence. *Photogramm. Eng. Remote Sens.*, 61:689–720.

Moussessian, A., Jordan, R., Rodriguez, E., Safaeinili, A., Akins, T., Edelstein, W., Kim, Y., and Gogineni, P. (2000). A new coherent radar for ice sounding in greenland. *Proceedings of IGARSS '00*, 2:484–6.

Munk, J., Jezek, K., Forster, R., and Gogineni, S. (2001). An accumulation map for the greenland dry-snow zone derived from spaceborne radar. *Journal of Geophysical Research.* submitted.

Ohmura, A. and Reeh, N. (1991). New precipitation and accumulation maps for greenland. *jglac*, 37:140–148.

Oppenheim, A. and Schafer, R. (1989). *Discete-Time Signal Processing.* Prentice Hall, New Jersey.

Partington, K. (1989). Discrimination of glacier facies using multi-temporal sar data. *Journal of Glaciology*, 44(146):42–53.

Paterson, W. (1994). *The Physics of Glaciers.* Elsevier, New York.

Prati, C., Rocca, F., and Guanieri, A. (1989). Effects of speckle and additive noise on the altimetric resolution of interferometric sar (isar) surveys. *IEEE Proceedings of IGARSS*, pages 2469–2472.

Rignot, E. (1995). Backscatter model for the unusual radar properties of the Greenland Ice Sheet. *Journal of Geophysical Research*, 100(E5):9389–9400.

Rignot, E. (1999). JPL, private communication.

Rignot, E., Gogineni, S., Krabill, W., and Ekholm, S. (1997). North and northeast greenland ice discharge from satellite radar interferomtry. *Science*, 276:934–7.

Rignot, E., Jezek, K., and Sohn, H. (1995). Ice flow dynamics of the greenland ice sheet from sar interferomtry. *Geophysical Research Letters*, 22(5):575–8.

Rott, H. and Rack, W. (1995). Characterization of antarctic firn by means of ers-1 scatterometer measurements. *IEEE Proceedings of IGARSS*, 3:2041–3.

Rott, H. and Siegel, A. (1996). Glaciological studies in the Alps and in Antarctica using ERS interferometric SAR. *Proceedings of Fringe*, 2:145–159.

Rott, H., Sturm, K., and Miller, H. (1993). Active and passive microwave signatures of Antarctic firn by means of field measurements and satellite data. *Annals of Glaciology*, 17.

Scambos, T., Kvaran, G., and Fahnestock, M. (1999). Improving avhrr resolution through data cumulation for mapping polar ice sheets. *Remote Sensing of Environment*, 69(1):56–66.

Shi, J., Davis, R., and Dozier, J. (1993). Stereological determination of dry-snow parameters for discrete-scatterer microwave modeling. *Annals of Glaciology*, 17:295–9.

Shih, S., Ding, K., Kong, J., and Yang, Y. (1997). Modeling of millimeter wave backscatter of time-varying snowcover. *PIER*, 16:305–30.

Shuman, C. (1995). Comparison of high-resolution isotope profiles and satellite passive microwave brightness temperature trends. *Journal of Geophysical Research*, 100:9165–77.

Sihvola, A. and Kong, J. (1988). Effective permittivity of dielectric mixtures. *IEEE Transactions on Geoscience and Remote Sensing*, 26(4):420–429.

Sohn, H.-G., Jezek, K., Baumgartner, F., Forster, R., and Mosley-Thompson, E. (1999). Radar backscatter measurements from radasat sar imagery of south pole stattion, antarctica. *IEEE Proceedings of IGARSS*, 4:2360–2.

Steffen, K., Box, J., and Abdalati, W. (1999). Accumulation variability derived with ground penetration radar along a transect of western greenland. In *EOS transactions*. AGU.

Thomas, R., Akins, T., Csatho, B., Fahnestock, M., Gogineni, P., Kim, C., and Sonntag, J. (2000). Mass balance of the greenland ice sheet at high elevations. *Science*, 289:426–428.

Tiuri, M., Sihvola, A., Nyfors, E., and Hallikaiken, M. (1984). The complex dielectric constant of snow at microwave frequencies. *IEEE Journal of Oceanic Engineering*, 9(5):377–381.

Touzi, R., Lopes, A., and Bruniquel, J. (1996). Statistics of the stokes parameters and of the complex coherence parameters in one-look and multilook speckle fields. *IEEE Transactions on Geoscience and Remote Sensing*, 34(2):519–531.

Touzi, R., Lopes, A., Bruniquel, J., and Vachon, P. (1999). Coherence estimation for SAR imagery. *IEEE Transactions on Geoscience and Remote Sensing*, 37:135–149.

Tsang, L., Kong, J., and Shin, R. (1985). *Theory of Microwave Remote Sensing*. Wiley, New York.

Ulaby, F., Moore, R., and Fung, A. (1981). *Microwave Remote Sensing, Active and Passive*. Addison-Wesley, London.

van der Veen, C., Mosley-Thompson, E., Gow, A., and Mark, B. (1999). Accumulation at the south pole: Comparison of two 900-year records. *Journal of Geophysical Research*, 104(D24):31067–76.

Weidick, A. (1984). Studies of glacier behaviour and glacier mass balance in greenland; a review. *Geografiska Annaler A*, 66:183–195.

Weidick, A. (1995). *Satellite Image Atlas of Glaciers of the World*, chapter Greenland. U.S. Geol. Surv. Prof. Pap., 1386.

Werner, C. (1999). GAMMA Remote Sensing, private communication.

West, R. (1994). *Microwave emission from polar firn*. PhD thesis, University of Washington.

West, R., Tsang, L., and Winebrenner, D. (1993). Dense medium radiative transfer theory for two scattering layers with arayleigh distribution of particle sizes. *IEEE Transactions on Geoscience and Remote Sensing*, 31(2):426–437.

West, R., Winebrenner, D., and Tsang, L. (1994). The influence of layering and grain size on microwave emission from polar firn. *IEEE Proceedings of IGARSS*, 3:1297–9.

Wismann, V., Winebrenenr, D., Boehnke, K., and Arthern, R. (1997). Snow accumulation on greenland estimated from ERS scatterometer data. *Proceedings of IGARSS '97*, 4:1823–1825.

Woods, G. A. (1994). Grain growth behavior of the gisp2 ice core from central greenland. Technical report, Earth Systems Science Center, Penn State University, USA.

Zebker, H. A., Farr, T. G., Salazar, R. P., and Dixon, T. H. (1994a). Mapping the world's topography using radar interferometry: The TOPSAT mission. *Proceeding of the IEEE*, 82(12).

Zebker, H. A. and Goldstein, R. M. (1986). Topographic mapping from interferometric SAR observations. *Journal of Geophysical Research*, 91(B5):4993–4999.

Zebker, H. A. and Lu, Y. (1998). Phase unwrapping algorithms for radar interferometry: residue-cut, least-squares, and synthesis algorithms. *josaa*, 15:586–598.

Zebker, H. A., Rosen, P. A., and Hensley, S. (1997). Atmospheric effects in interferometric synthetic aperture radar surface deformation and topography maps. *jgr*, 102:7547–7563.

Zebker, H. A. and Villasenor, J. (1992). Decorrelation in interferometric radar echoes. *IEEE Transactions on Geoscience and Remote Sensing*, 30(5):950–959.

Zebker, H. A., Werner, C. L., Rosen, P. A., and Hensley, S. (1994b). Accuracy of topographic maps derived from ERS-1 interferometric radar. *IEEE Transactions on Geoscience and Remote Sensing*, 32(4):823–836.

Zuniga, M., Habashy, T., and Kong, J. (1979). Active remote sensing of layered random media. *IEEE Transactions on Geoscience and Remote Sensing*, 17(4):74–79.

Zwally, H. (1977). Microwave emissivity and accumulation rate of polar firn. *Journal of Glaciology*, 18:195–215.

Zwally, H. and Giovinetto, M. (1995). Accumulation in antarctica and greenland derived from passive-microwave data: A comparison with contoured complications. *Annals of Glaciology*, 21:123–30.